DISSERTATION

BANDWIDTH ENHANCEMENT IN MULTIMODE FIBER OPTIC COMMUNICATION SYSTEMS CONSIDERING SOURCE NON-IDEALITIES

Submitted by

Sulaiman Saleh Al-Sowayan

Department of Electrical and Computer Engineering

In partial fulfillment of the requirements

for the Degree of Doctor of Philosophy

Colorado State University

Fort Collins, Colorado

Summer 2005

COLORADO STATE UNIVERSITY

April 20th, 2005

WE HEREBY RECOMMEND THAT THE DISSERTATION PREPARED UNDER OUR SUPERVISION BY SULAIMAN SALEH AL-SOWAYAN ENTITLED BANDWIDTH ENHANCEMENT IN MULTIMODE FIBER OPTIC COMMUNICATION SYSTEMS CONSIDERING SOURCE NON-IDEALITIES BE ACCEPTED AS FULFILLING IN PART REQUIREMENTS FOR THE DEGREE OF DOCTOR OF PHILOSOPHY.

Committee on Graduate Work

Adviser

Department Head

ABSTRACT OF DISSERTATION

BANDWIDTH ENHANCEMENT IN MULTIMODE FIBER OPTIC COMMUNICATION SYSTEMS CONSIDERING SOURCE NON-IDEALITIES

The research described in this dissertation investigated the impact of source behavior on the bandwidth of multimode fiber (MMF) optic communication links. Physical as well as signal processing modifications were considered that enhanced the performance of a dispersion limited, 1 km long link. Experiments demonstrated that a single mode optical source reduced the MMF fiber bandwidth by 30 % relative to a multimode vertical cavity surface emitting laser (VCSEL) source. The single mode optical source was created by coupling the same multimode VCSEL into a single mode fiber(SMF) or by directly using a single mode VCSEL. However, a simple operation of separating the single mode source from the MMF fiber to an optimum distance would regain the multimode bandwidth without losing more than 10% of the total power. This scheme is considered to be simpler to implement than the standard offset launch method. Further, experimental measurements have shown that the beam divergence distributions of commercial, multimode VCSELs are data pattern dependent even with data patterns that maintain the same thermal conditions. The impact of this nonlinear source behavior on optical link performance has been evaluated by characterizing the angle and offset dependent differential mode delay of a multimode fiber using multiple experimental approaches as well as computer modeling. An algorithm has been implemented for equalizing

the combined link by taking into account the nonlinear data pattern dependent beam divergence distribution of the source coupled with the angle dependent behavior of the MMF. The nonlinear algorithm results in a 2 dB improvement in the receiver sensitivity at a 10^{-9} bit error rate.

Sulaiman Saleh Al-Sowayan
Department of Electrical and Computer Engineering
Colorado State University
Fort Collins, Colorado 80523
Summer 2005

TABLE OF CONTENTS

1 Introduction 1

1.1 Definition of The Problem 1

1.2 Research Objective and Outline 3

2 Equalization 5

2.1 Background 5

2.2 Introduction 6

2.3 Linear Equalization 10

2.3.1 Feedforward Filter 10

2.3.2 Feedback Filter 13

2.4 Non-linear Equalization 16

2.5 Performance Evaluation and Research Results 17

2.5.1 Performance Evaluation 17

2.5.2 Performance Evaluation Verification 20

2.5.3 MMF As a Linear System 21

3 Fiber Impulse Response 26

3.1 Introduction 26

3.2 Launch Condition and Fiber Impulse Response 26

3.2.1 Optical Source Effects 26

3.2.2 Launch Condition and Bandwidth 28

3.3 Parametrization of Graded Index Multimode Fiber Modes 30

3.3.1 Parametrization of Meridional Modes 30
3.3.2 Parametrization of Meridional and Helical Modes 31
3.3.3 Modeling of GIMMF Modes 33

4 Fiber Bandwidth Enhancement 35

4.1 Introduction 35
4.2 Simple Launch Technique for Bandwidth Enhancement 36
4.2.1 Experiment 36
4.2.2 Measurement Results 38
4.2.3 Application and Discussion 42
4.2.4 Summary 44
4.3 Simple Launch Technique using Single Mode Laser 45
4.3.1 Experiment 45
4.3.2 Results 46
4.4 VCSEL Beam Divergence Dependence on Data Pattern 48
4.4.1 Experiment 50
4.4.2 Experiential Results 51
4.4.3 Discussion of Results 56
4.4.4 Summary 58
4.5 System Bandwidth Dependence on Data Pattern 59

5 Pattern Dependency Effects on Link and Nonlinear Equalization 63

5.1 Introduction 63
5.2 Angle/Offset Launch Experiments 64
5.2.1 Method 64
5.2.2 Angle Experiment 66
5.2.3 Offset Experiment 68
5.3 Pinhole Launch Experiment 71

5.4 Near Field Aperture Launch Experiment 74
5.5 Fiber Modes Model and Effective Impulse Response 77
5.6 Non-linear Equalization 86
5.6.1 Method 87
5.6.2 Algorithm and Results 88

6 Summary and Suggested Future Research **93**
6.1 Summary 93
6.1.1 Previous Work 93
6.1.2 Single Mode Source with MMF 93
6.1.3 Beam Divergence Dependence on Data Pattern and Its Impact on Link Performance 94
6.2 Suggested Future Research 95

LIST OF FIGURES

1.1 Material and wave-guide dispersion as a function of wavelength for fused-silica fiber reproduced after[2]. 2

2.1 Communication system. 5

2.2 Spatially resolved optical receiver. 8

2.3 Feedforward filter. 10

2.4 Feedforward equalization (a)Input data, (b)Fiber impulse response, (c)Data with no equalization, (d)Data after equalization. 13

2.5 Power penalty due to equalization vs. bit rate. 14

2.6 Feedback filter structure. 14

2.7 Feedback equalization (a)Input data, (b)Fiber impulse response, (c)Data with no equalization, (d)Data after equalization. 16

2.8 DFE equalizer structure. 17

2.9 Test of bit neighborhood. 18

2.10 Real measurment of noise which appear Gaussian. 19

2.11 Performance evaluation experimental setup. 19

2.12 Performance evaluation verification experimental setup. 20

2.13 Comparison between BER measured and estimated. 21

2.14 (a)The optical input pulse to the 1 km MMF, (b)The output of the fiber which represents its impulse response. 22

2.15 Linearity measure for 1km MMF fiber. 23

2.16 Equalization result: (a)The impulse response of the fiber, (b)The received data with no equalization, (c)Data after equalization 24
2.17 Experimental setup for producing the BER curves as a function of received power. 25
2.18 BER curves as a function of received power no equalization (solid), with linear equalization (dashed.) 25

3.1 LED used as source (upper) which produce OFL, and VCSEL (lower) which produce narrow beam. 27
3.2 Refractive index profile for GIMMF fibers with a central peak (inset), Bandwidth dependence on angle of launch and laser to fiber offset (reproduced after[24] for 850nm transmission. 28
3.3 parametrization of GIMMF meridional modes. 29
3.4 Contour plot showing GIMMF meridional mode numbers with respect to offset and angle of launch. 30
3.5 parametrization of GIMMF axial, meridional, and helical modes with three dimensions shown in inset. 32
3.6 parametrization of GIMMF modes by the travel time. 33

4.1 Experimental setup. 37
4.2 Total average power as a function of the separation distance d: from average power meter(dashed) , and integration under the curve from the temporal measurement (solid). 38
4.3 Total average power as a function of the separation distance d (solid), and Gaussian beam fitting (dashed). 39
4.4 Temporal response contour plot as a function of the separation distance d. 39

4.5 Average lower order mode power as a function of the separation distance d(solid), and Gaussian beam fitting(dashed). 40
4.6 SMF to MMF separation configuration. 41
4.7 Ratio of slow mode power to total power. 41
4.8 (a)Impulse response for $d = 0$ (solid), at optimum distance of $125\mu m$ (dotted), and the multimode impulse repose out of multimode VCSEL directly to the multimode fiber (dashed), (b)Frequency responses for $d = 0$ (solid), at optimum distance of $125\mu m$ (dotted), and multimode VCSEL directly to the multimode fiber (dashed.) . 45
4.9 Single mode laser to MMF temporal response contour plot as a function of the separation distance 46
4.10 3 dB bandwidth calculations as a function of the separation distance . . 47
4.11 Eye diagram at zero separation. 48
4.12 Eye diagram at 150 μm separation. 49
4.13 Experimental setup for measuring the BER. 49
4.14 BER for a data rate of 625 Mbps with zero separation (solid), and 150 μm separation (dashed) 50
4.15 Experimental setup for measuring VCSEL's beam divergence. 52
4.16 Beam divergence angle distribution for Part A: alternating ones and zeros pattern (solid), alternating sixteen ones and sixteen zeros (dashed), and gain switched pulse one followed by fifteen zeros (dotted). Dotted data is multiplied by 7 to ease comparison. 53
4.17 Beam divergence angle distribution for Part B: alternating ones and zeros pattern (solid), alternating sixteen ones and sixteen zeros (dashed). 54
4.18 Bit time pulses of Part A: (a) at 0 degrees, (b) at -3 degrees, and (c) at -6 degrees. 55

4.19 Bit time pulses of Part B: (a) at 0 degrees, (b) at -3 degrees, and (c) at -7.5 degrees. 56
4.20 Total integrated bit time pulses of: (a) Part A, and (b) Part B. 57
4.21 Bit time pulses of Part A: regular pulse (solid), and gain switched pulse (dotted): (a) At 0 degrees, and (b) At -6 degrees. 58
4.22 Bit time pulses of regular pulses (solid), and reduced drive current pulses (dotted). 59
4.23 Increased bias level bit time pulses of regular pulses (solid), and reduced drive current pulses (dotted). 60
4.24 Beam divergence angle distribution for Part A: alternating ones and zeros pattern (solid), alternating sixteen ones and sixteen zeros (dashed). 61
4.25 Bit time pulses of VCSEL at 0 degrees 61
4.26 Power distribution over Beam divergence. 62

5.1 Beam divergence distribution of alternating ones and zeros with weight coefficients displayed. 65
5.2 Collimated beam launch angle experimental setup. 66
5.3 Temporal response contour plot as a function of the launch angle. . . . 68
5.4 Temporal response at: zero degree (solid), and 13 degrees (dashed). . . 69
5.5 Offset launch experimental setup. 69
5.6 Temporal response contour plot as a function SMF launch radial position. 70
5.7 Spatial filtering idea using a pinhole. 71
5.8 Pinhole experimental setup. 72
5.9 Spatial beam shape as a contour plot as a function of distance from aperture. 75
5.10 Spatial beam shape plot for distance from aperture (a) $0.5\mu m$, (b) $20\mu m$, (c) $100\mu m$ 76

5.11 Spectrometer setup to measure separation between fiber and mask. . . . 76
5.12 Response of 16 μm circle (solid), 14 μm circle (dashed), 12 μm circle (dotted). 78
5.13 Mask set experiment configuration. 78
5.14 Cone responses of 15 μm offset (solid), 13 μm offset (dashed). 79
5.15 parametrization of GIMMF modes by the travel time. 80
5.16 Gain-switched VCSEL optical output pulse. 81
5.17 Beam divergence distribution of gain switched pulses with weight coefficients displayed. 82
5.18 Measured gain-switched VCSEL optical output from the MMF fiber. . 83
5.19 Model output. 84
5.20 Comparison between measured and model predicted beam mean delay time. 85
5.21 Model predicted impulse response for Part A: alternating ones and zeros pattern (solid), alternating sixteen ones and sixteen zeros (dashed). 86
5.22 Model predicted impulse response for Part B: alternating ones and zeros pattern (solid), alternating sixteen ones and sixteen zeros (dashed). 87
5.23 Measured far field scans for five different data patterns. 88
5.24 Algorithm flow chart. 91
5.25 BER curves for: no equalization (solid), linear equalization (dashed), the developed algorithm (dotted), and the no dispersion limit shown. 92

LIST OF TABLES

5.1 Comparison between measured and model predicted beam mean delay time 85

5.2 Impulse responses with corresponding consecutive ones 89

Chapter 1

INTRODUCTION

1.1 Definition of The Problem

Fiber optic channels with their high capacity have become a major information transmission system in both long haul and short communication systems such as local area networks (LAN). In general fiber optic channels are more immune to attenuation, interference, and bandwidth limitations than any other transmission channels. Fiber cables can be classified into two main categories based on the set of electromagnetic waves (modes) propagating through them: single mode fibers (SMF) and multimode fibers (MMF).

SMF fibers are used in long haul telecommunications due to their high bandwidth distance product compared to MMF fibers. MMF fibers are used in LANs, which do not require a large bandwidth-distance product since they span a few hundred meters distance[1]. Multimode fibers are also classified into two categories in terms of the refractive index profile of the core of the fiber: step index, and graded index. This work focus on graded index multimode (GIMMF) fibers, which are widely used in local area networks.

One of the main limitations of MMF based systems is dispersion which can be defined as the spread in time of the received pulse beyond the duration of the pulse at the transmitter. The causes of dispersion in fiber optic systems are either the channel itself (fiber) or the optical source used with the channel as the transmitter.

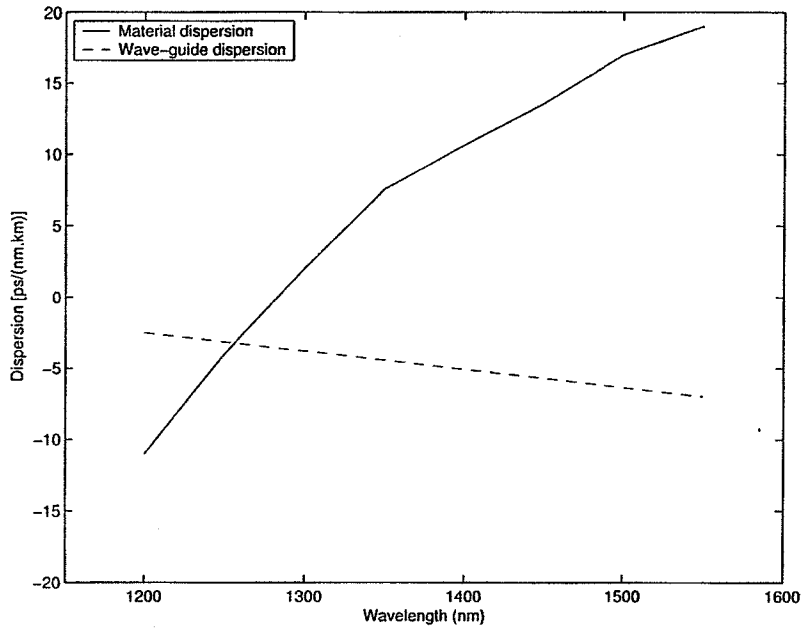

Figure 1.1: Material and wave-guide dispersion as a function of wavelength for fused-silica fiber reproduced after[2].

To be more specific, there are three types of dispersion: modal dispersion, wave-guide dispersion, and material dispersion. Modal dispersion is due to the fact that different modes in the fiber propagate in different paths, leading to different arrival times of the modes of one of the pulses that spreads the pulse. Wave-guide dispersion is a result of the fact that the modal propagation constant is a function of wavelength. Material dispersion is due to variation of the refractive index with wavelength. In MMF the dominant type of dispersion is modal dispersion, while in SMF there is no modal dispersion. Material and wave-guide dispersions can be expressed as a function of wavelength (see Figure 1.1). Modal dispersion is not shown here.

For high data rates depending on the bandwidth of the fiber, GIMMF used in LANs are generally dispersion-limited rather than loss-limited. Losses in such systems are typically 2.5 dB/km at wavelength of 850 nm.

As a result of the dispersion, the separation between adjacent pulses is reduced. Portions of the pulse may spread into the neighboring pulse's time slot,

producing what is known as intersymbol interference (ISI). ISI means that the responses of the transmitted pulses overlap each other in time. The resulting superposition of signals causes shifts in the location of the signal peak and variances in signal amplitude. When signal distortion is too great, errors can be made in the detection process at the output. Therefore, as the bit rate increases, the bit error rate (BER) simultaneously increases.

1.2 Research Objective and Outline

ISI is a limiting factor on the bit rate of dispersion-limited systems because if ISI is avoided, the time slot for each bit should not be affected by the dispersion outcome. As a consequence, practical MMF can have a relatively low bandwidth. However, if the effects of ISI can somehow be reduced, the achievable bit rate for a given error probability can likewise be increased. To compensate for this distortion and increase the bit rate, a process known as equalization is used. Equalization means any process used to compensate for ISI.

In this dissertation, a literature review of equalization in fiber optic communications systems has been presented with emphasis on gaps that have not been filled in the area of MMF. A study of the modes of GIMMF fibers is presented here with emphasis on their parameterization in terms of launching techniques. Methods are proposed for increasing the bandwidth of the graded index multimode fibers used in LANs utilizing vertical cavity surface emitting lasers (VCSEL) as the source of communications.

Chapter 2 discusses equalization efforts carried out in the area of fiber optic systems and related areas of study that have not yet been described in the technical literature, with some research results related to linear equalization. Chapter 3 presents the fiber channel impulse response with emphasis on the impact of the type of optical source used with optical fiber channels. This chapter also includes

a study with modeling and simulation of the modes of the GIMMF fibers and their relationship to the launch method employed. A new launch method that would increase the GIMMF fiber bandwidth is presented in Chapter 4, followed by presentation of the idea of VCSEL beam divergence dependence on data pattern, and effectively the GIMMF impulse response. In Chapter 5, various impulse responses for, different data patterns are given from both fiber model and experiment with proper non-linear equalization. Finally, a summary and ideas for future research are introduced in Chapter 6.

Chapter 2

EQUALIZATION

2.1 Background

ISI is produced when a transmitted signal $b(t)$ has a greater bandwidth than the channel carrying it. ISI causes the received signal $c(t)$ to contain errors, but the effect of ISI can be reduced by the use of an equalizer. The term equalization can be used to describe any signal processing operation to reduce ISI. The requirement on the equalizer is that the overall system impulse response, which is the convolution of the channel impulse response $f(t)$ and the equalizer impulse response $h(t)$, would produce a sufficient bandwidth for the transmitted signal $b(t)$. It is appropriate to point out that this research deals with discrete time models since it is convenient to work with such models when dealing with ISI. Discrete time pulses are produced by sampling the data pulses and channel impulse response at the same rate as the data rate. Generally there are different types of equalization: linear and non-linear, or static, and adaptive. These issues will be discussed in the following sections starting with the current status of fiber optic equalization in literature.

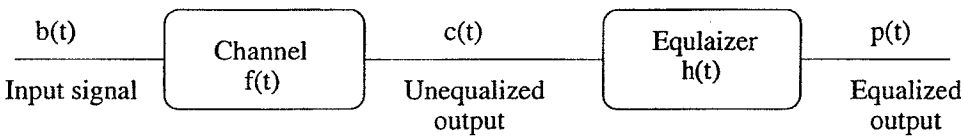

Figure 2.1: Communication system.

2.2 Introduction

Equalization processes are well-known in the area of copper-wire systems. Nearly every book in the field of communications deals with this subject. However, in the area of fiber optic systems, a moderate number of papers have been published related to equalization in SMF fibers.

One source of dispersion in SMF fibers is polarization mode dispersion (PMD). PMD in single mode fibers is far smaller than chromatic dispersion but PMD is not well compensated for by traditional techniques. Some of the work related to mitigation of PMD is carried in the electrical domain[3],[4] and some in the optical domain, such as [5]. In [3], the authors are optimistic that the electrical domain, or what is known as post-detection, holds great promise for distortion mitigation in single mode fibers such as PMD, having simulated a polarization diversity receiver structure using accurate models of the PMD distortion. The authors of [4] did both simulation and experimental adaptive equalization for PMD that sets its weights by the method of least mean square. The authors of [5] carried out PMD mitigation efforts in the optical domain using a simple polarization controller followed by a polarization maintainer fiber, whereby they effectively reduced the bit error rate from 10^{-6} to 10^{-9}.

The work in mitigation of the PMD in single mode fiber is immense and carried out in both the electrical and the optical domain, where our field of multimode fibers most of the equalization processes are done in the optical domain . Perhaps the first article dealing with equalization was by Kasper in 1982[6], reporting simulated linear feedforword and decision feedback filters by modeling the fiber channel as a Gaussian channel. He then carried out a performance evaluation by considering the increased supported bit rate to the resulting power penalty and then comparing it to various systems, such as four leveling.

Most of the work done afterwards was in the optical domain rather than the electrical domain. The authors of [7]-[9] reported that using a light-emitting diodes (LED) as a source with MMF will overfill the modes of the fiber, meaning that it will excite the modes of the fiber comparably, resulting in the so called overfilled launch OFL bandwidth, and when using a laser based transmitter the modes of the fiber will underfill, indicating excitation of a selection of low order modes in a small spot at the center of the fiber. Unfortunately, there is a common error in the manufacture of the graded index multimode fibers (GIMMF) of having a distinct peak or dip in the refractive index profile at the center of the fiber, which means that propagation constants will be differ widely for the propagating modes, thereby severely reducing the bandwidth to below the OFL bandwidth. These authors proposed a criterion of the restricted launch condition using the offset launch from source to fiber in order to avoid the defective area at the center of the fiber, thus eliminating the effect of the refractive index profile defect at the center of the fiber, which in turn enhances the stability of the fiber bandwidth. The authors of [10] introduced a simple device that blocks the center emission of the VCSEL so that it does not go into the center of the fiber, which would increase the bandwidth of the fiber. The authors of [11] proposed a device that consists of a 10 cm hollow fiber that would act as a mode converter that would convert the power coupled to the lower order mode to the higher order mode and then increase the effective bandwidth.

All of the above have carried out their work on the transmitter side, or what is known as pre-equalization. On the receiver side, the authors of [12],[13] have introduced a new method termed spatially resolved equalizer (SRE) that divides the optical receiver into two parts, inner and outer (see Figure 2.2); the pulses received by the two parts are then subtracted from each other to obtain a two-fold increase in bandwidth out of the fiber. In [14], the same authors also combined

this SRE with what is considered equalization in the electrical domain by the use of forward error correction (FEC) coding. It is noteworthy that they claim that equalization using FEC alone will not improve the bit rate as well as with processing in the optical domain. In [15], the same authors reported that they used the above method of SRE with the use of a decision feedback equalizer (DFE). The basic concept of the DFE is that once the value of the currently transmitted symbol is determined, the ISI contribution of that symbol can be precisely removed to future symbols; that is, it utilizes the previous bit decisions to cancel ISI. With the use of SRE Ralph and his group were able to reduce the complexity of the design of the DFE by a factor of 3.

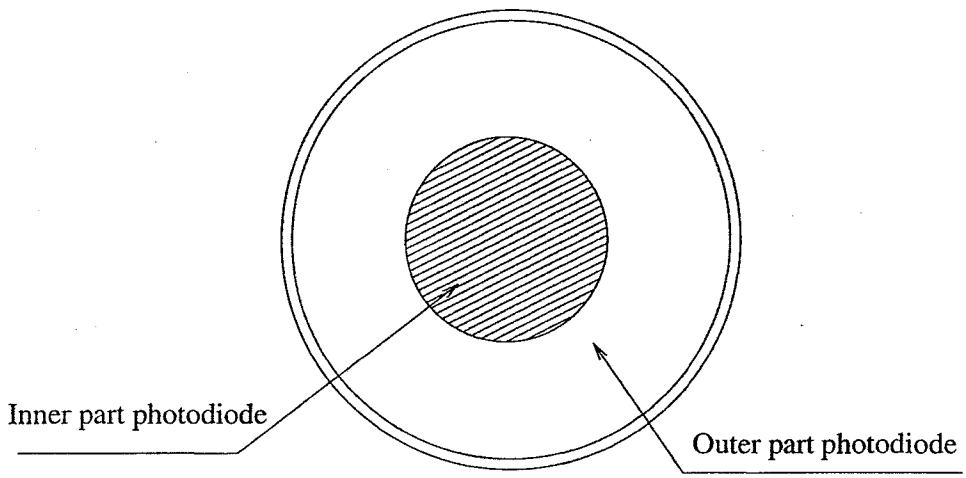

Figure 2.2: Spatially resolved optical receiver.

In [16], the authors proposed a digital pre-equalization for VCSELs by using a 3.3v CMOS circuit. Their idea was to operate the VCSEL at its threshold and increase the current for "1"s that are in the leading edge-that is, preceded by "0" by a certain amount, and reduce the "0"s current in the leading edge; i.e., preceded by "1" by the same amount. These authors carried out their performance evaluation by looking at the eye diagram and then improving the eye opening by 9.5% under no pre-equalization; they then carried out the same experiment with

pre-equalization to obtain a 25% improvement in the eye opening. They also modeled the fiber as Gaussian with various mode delays and widths to produce the measured eye diagrams; they then simulated the output of their pre-equalizer circuit to predict an increase in the eye opening of 3% for unconditioned launch and 10% for conditioned launch. The difference between the calculated values and measured values in the increase of the eye opening is the slow roll-off in the impulse response in the experimental results compared to the modeled. In [17], the authors carried out a 10 Gbps transmission over a 1.5km MMF by using a decision feedback equalizer (DFE) on the receiver side. They designed their tap weights using the least mean squares converging method, by which training pulse are sent, which repair the tap weights when they converge. These authors carried out their equalization experimentally analogly, and the taps where carried out by amplifiers and attenuators. It is noteworthy that in [17] authors reported that MMF has a stable modal behavior as long as launching conditions remain the same However, in our thesis as will be presented later the excitation of modes depends on the data pattern.

In [18], the authors designed an analog 7-tap differential feedforward equalizer. They used analog utilizing feedforward rather than digital because of the high speed at which the experiment was conducted. These authors improved the ISI penalty by 9 dB and also reduced the time jitter from 60 to 21 psec. The authors of [19] designed a feedforward equalizer that is operated at 5 Gsymbol/sec at multilevel sense by using a 2 μm GaAs HBT process. Their idea is to combine the multilevel pulse amplitude modulation PAM with the linear equalization, which improves the performance over the regular on-off keying (OOK). They did not report any numbers for the improvement but rather some eye diagram figures. In [20], the authors made some modeling and simulation comparisons between the feedforward equalizer and the decision feedback equalizer based on real measured three MMF

impulse responses and they produced the BER curves for each equalizer. For certain distances and the BER requirement, they found the optimum number of taps for each filter and the improvement that each one would yield. In the next sections a brief illustration of the types of equalization that have been mentioned in the above literature review is presented.

2.3 Linear Equalization

Linear equalization compensates for distortion due to ISI but also enhances the noise present[21]. Consequently it is linear in the sense that it deals with signal and noise equally. The two main types of linear equalizers are termed feedforward filter and feedback filter.

2.3.1 Feedforward Filter

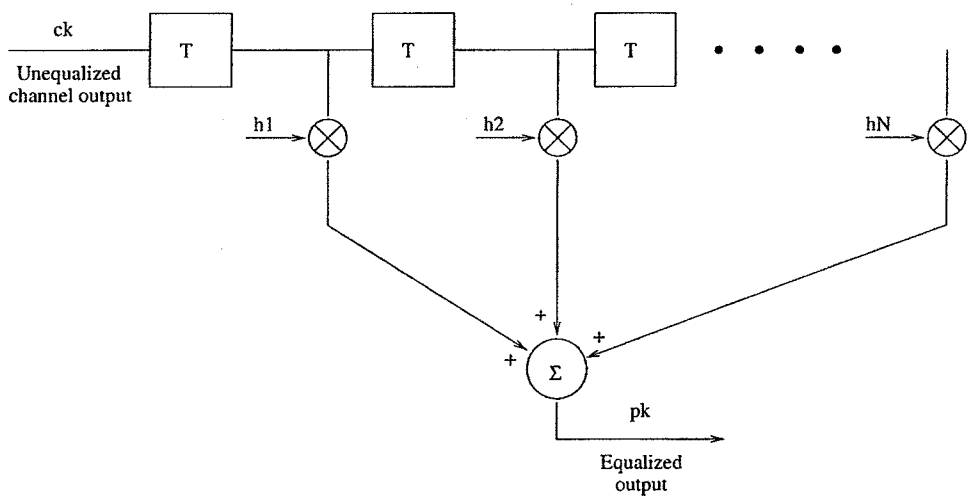

Figure 2.3: Feedforward filter.

A feedforward filter is a finite impulse response filter (FIR). It is made up of tapped delays with the tapping spaced a bit period T apart. In this filter both current and past data values are linearly weighted by tap weights h_1, h_2,.. and then summed up to produce the output. There are different methods of calculating

the tap weights three of which are presented in the next subsections followed by examples of these methods.

2.3.1.1 Zero Forcing Method

Let us assume that the information bit is b_k and the fiber impulse response is represented by f_k. Then the received signal c_k can be written as

$$c_k = b_k * f_k, \tag{2.3-1}$$

where * denotes convlution. The equalized output p_k can be written as

$$p_k = c_k * h_k, \tag{2.3-2}$$

where h_k is the impulse response of the equalizer

$$p_k = b_k * f_k * h_k \tag{2.3-3}$$

So to make $p_k = b_k$ requires

$$f_k * h_k = \delta_k \tag{2.3-4}$$

In a matrix form, for a finite number of taps we can write

$$\begin{pmatrix} f_0 & f_{+1} & \cdot & \cdot & f_{N-1} \\ f_{-1} & f_0 & \cdot & \cdot & \cdot \\ \cdot & \cdot & \cdot & \cdot & \cdot \\ \cdot & \cdot & \cdot & \cdot & \cdot \\ f_{-N+1} & \cdot & \cdot & \cdot & f_0 \end{pmatrix} \begin{pmatrix} h_1 \\ h_2 \\ \cdot \\ \cdot \\ h_N \end{pmatrix} = \begin{pmatrix} 0 \\ \cdot \\ 1 \\ \cdot \\ 0 \end{pmatrix} \tag{2.3-5}$$

It is now easy to calculate the vector h which represents the tap weights by multiplying the inverse of the f matrix with the delta vector. The name of this method came from forcing the contributions of the adjacent bits being to zero. The problem with this method is that it compensates for the channel distortion at the expense of enhancing the additive noise.

2.3.1.2 Minimum Square Error (MSE) Method

The MSE method is basically designed to minimize the error between the equalized output and the sent data. That is solving for minimum square error by defining this error as a function of the different elements of the system, including the tap weights vector, and then minimizing this error by equating to zero its derivative with respect to the tap weights vector, and solving for the tap weight vector. The error to be solved is

$$\varepsilon_n = E[(b_n - p_n)^2] \tag{2.3-6}$$

Where $p_k = \sum h_m c_{k-m}$. To minimize the error

$$\frac{\partial \varepsilon}{\partial h_k} = 0; \forall k \tag{2.3-7}$$

Then solve for h_k

2.3.1.3 Training Sequence

The training sequence method is carried out by sending a known training sequence and adjusting the tap weights until the equalized output is the same as the training sequence.

2.3.1.4 Example Data

Figure 2.4(a) shows some example data b_k that might be sent through a channel with a normalized Gaussian impulse response, f_k shown in Figure 2.4(b). The received signal c_k is shown in Figure 2.4(c), which represents the convolution of the transmitted data b_k with the channel f_k. By using the zero forcing method to calculate the tap weights of the feedforward filter with five taps, Figure 2.4(d) shows the output after the equalizer. Note that there is no noise included in the simulation in this example.

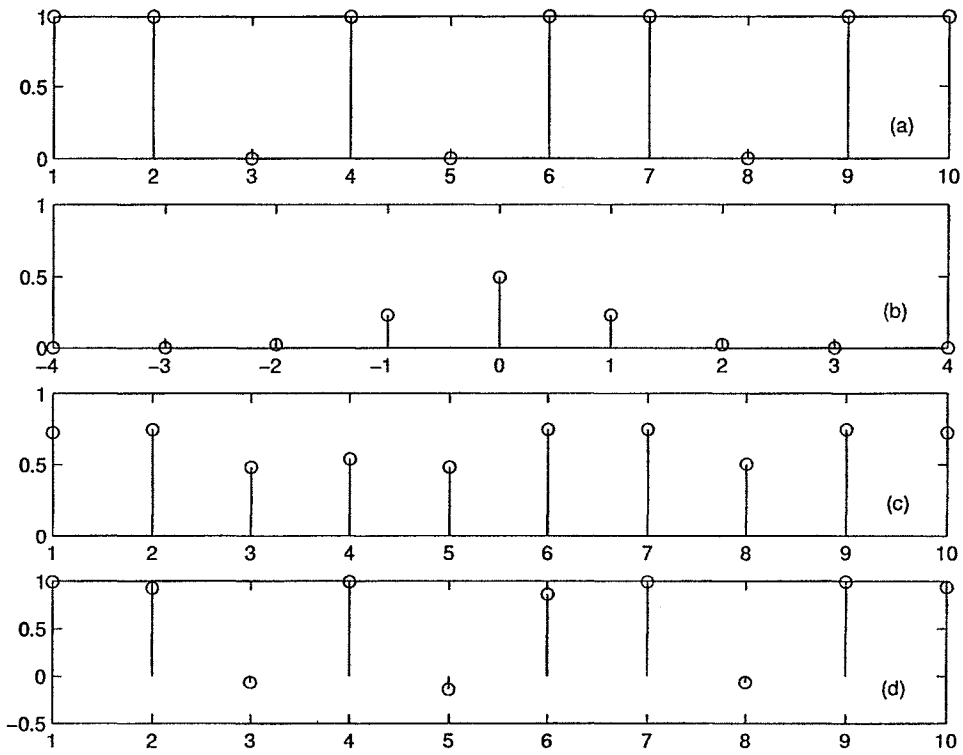

Figure 2.4: Feedforward equalization (a)Input data, (b)Fiber impulse response, (c)Data with no equalization, (d)Data after equalization.

To consider the noise reproduction of one simulation result of [6] that plots the power penalty versus the ratio of $6dB$ bandwidth to the bit rate, a simulation of this was done by introducing an additive white Gaussian noise (AWGN) with known characteristics. Equalization with an 11 tap feedforward filter was then carried out and the power penalty was calculated by calculating the change of the signal to noise ratio due to equalizer, followed by change bit rate, and then this step was repeated. Figure 2.5 shows this result which is in good agreement with that of [6].

2.3.2 Feedback Filter

The feedback filter is an infinite impulse response (IIR) filter. Its output depends on the past values of the output. The advantage of an IIR filter over a FIR filter is that it can 100% correct for the channel, but the disadvantage is

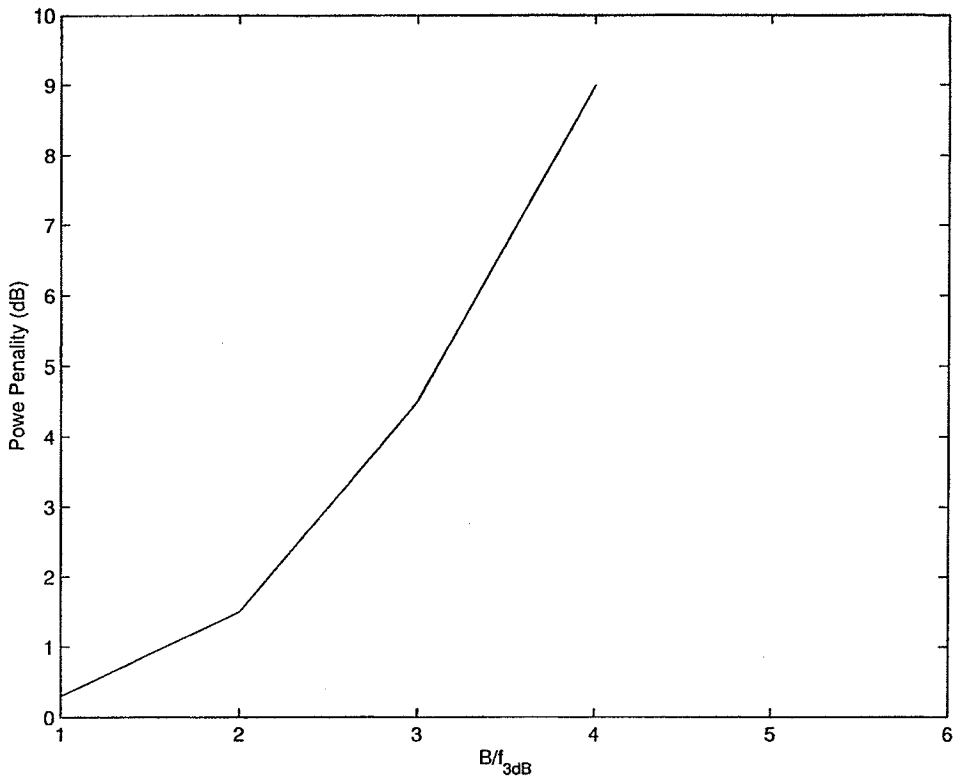

Figure 2.5: Power penalty due to equalization vs. bit rate.

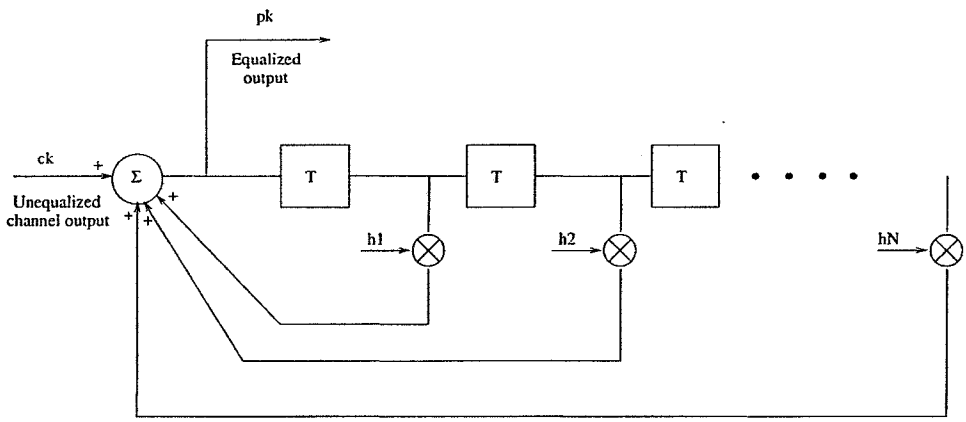

Figure 2.6: Feedback filter structure.

its stability, which means if an error occurs, this error will propagate through the whole data sequence. The output of Figure 2.6 can be represented as follows:

$$p_k = c_k + h_1 p_{k-1} + h_2 p_{k-2} ... + h_N p_{k-N} \tag{2.3-8}$$

$$c_k = p_k[1 - h_1 p_{-1} - h_2 p_{-2} ...] \tag{2.3-9}$$

The frequency response of this stage, which is the equalizer, can be written as

$$H(\theta) = 1/(1 - h_1 e^{-j\theta} - h_2 e^{-2j\theta} ..) \tag{2.3-10}$$

And for the channel frequency response $C(\theta)$ for a four taps filter is

$$C(\theta) = f_2 e^{2j\theta} + f_1 e^{j\theta} + f_0 + f_{-1} e^{-j\theta} + f_{-2} e^{-2j\theta} \tag{2.3-11}$$

To eliminate the ISI, the condition $H(\theta) = 1/C(\theta)$ should be satisfied and hence the tap weights should be

$$h_i = -f_{2-i}/f_2 \tag{2.3-12}$$

2.3.2.1 Example Data

Figure 2.7(a) shows the data b_k that might be sent through a channel represented by its impulse response f_k, shown in Figure 2.7(b), which is a normalized Gaussian channel. The received signal c_k is shown in Figure 2.7(c), which is the convolution of the transmitted data b_k with the channel f_k. Utilizing the above method to calculate the tap weights of the feedback filter with five taps, Fig 2.7(d) shows the output after the equalizer. Note that there is no noise simulated in this example.

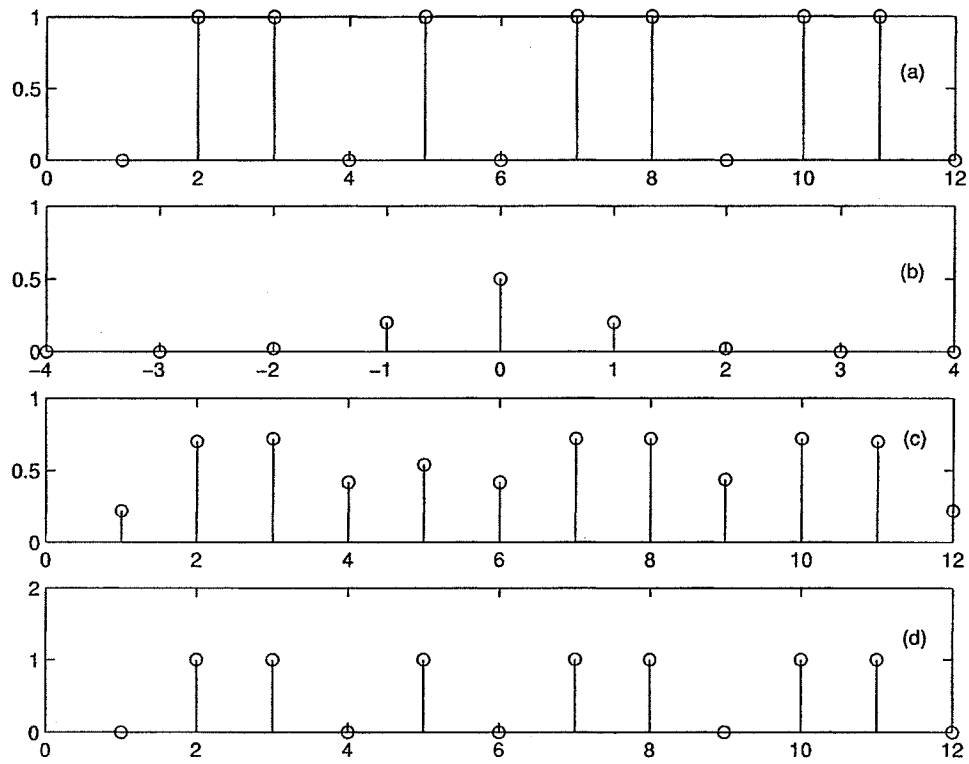

Figure 2.7: Feedback equalization (a)Input data, (b)Fiber impulse response, (c)Data with no equalization, (d)Data after equalization.

2.4 Non-linear Equalization

As mentioned before, linear equalization deals with the input data and the noise equally. Since the equalizer enhances the high frequency response to compensate for ISI, it also enhances the noise. When the noise of the system is considered, linear equalization may not recover the input bit sequence correctly. This motivates non-linear equalization, which deals with the input data differently than noise. One well-known form of non-linear equalization is the decision feedback equalizer (DFE). The basic idea of the DFE is that once the value of the current transmitted symbol has been determined, the ISI contribution of that symbol can be precisely removed from future symbols; i.e., it utilizes the previous bit decisions to cancel the ISI. The non-linearity is due to the decision device that determines which symbol of a set of discrete levels was actually sent. Once this bit has been

decided upon, the filter structure takes this into account in the next symbol detection.

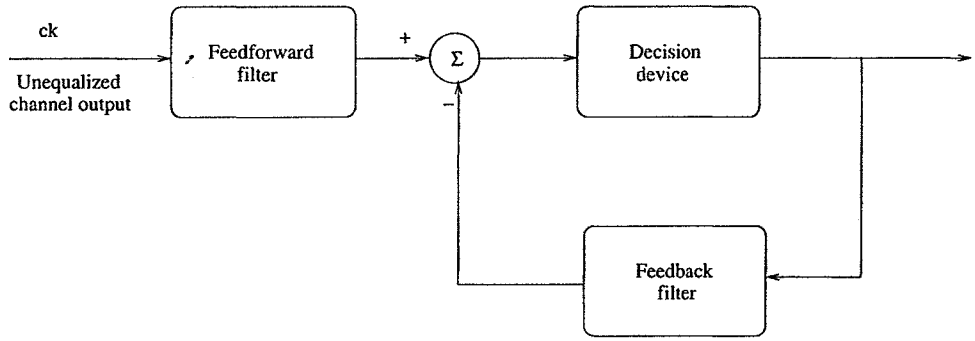

Figure 2.8: DFE equalizer structure.

Another type of non-linear equalization is what is known as maximum likelihood sequence estimation (MLSE), which deals with the channel as unknown and the detection process as a statistical decision problem. In principle, MLSE makes the detection process not dependent on a bit-by-bit basis but rather on a sequence of transmitted bits based on a set of observed received signals.

2.5 Performance Evaluation and Research Results

2.5.1 Performance Evaluation

This research deals with a LAN standard 1.25 Gbps data rate. Hence, to achieve equalization and monitor bit error rate (BER) as performance evaluation requires a multi-thousand dollar A/D converter and in addition a same value DSP chips, which our lab dos not have. An alternative method for measuring BER will be presented in this section. This method was half-experimental and half-theoretical. In this method, the two sources of error in the detection process were studied: errors due to ISI and errors due to system noise. In the errors due to ISI, a study of how many bits can be considered as a neighborhood were undertaken. Figure 2.9 shows that two leading bits are sufficient to cause the desired bit to reach

steady state; i.e., saturation for a long string of 1s. Consequently, by carrying out this experiment at 1.25 Gbps, the conclusion was reached that the desired bit should be in the middle of four data bits, two before and two after. There are sixteen possible combinations of these bits, and all combinations are equally likely.

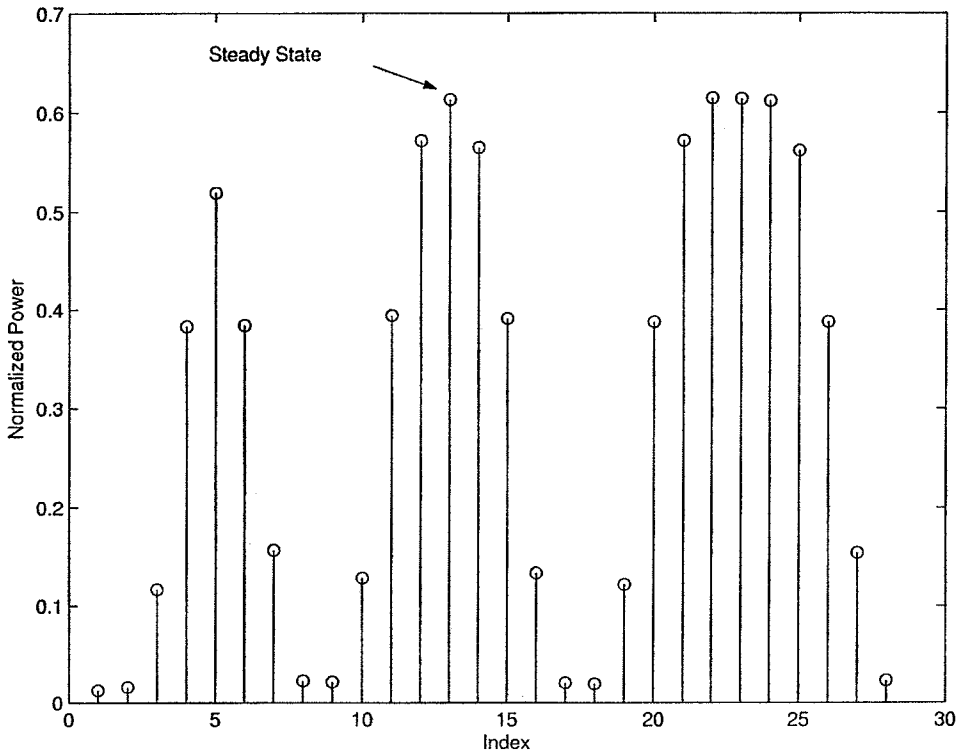

Figure 2.9: Test of bit neighborhood.

Now consider errors due to noise. The noise measured here experimentally and modeled as Gaussian noise, which is a very reasonable model[22]. Figure 2.10, shows the real noise and its distribution, which appears very close to Gaussian.

By assuming the system noise to be Gaussian, the BER can then be estimated as follows: Figure 2.11 shows the experimental setup of our performance evaluation system.

The data generator drives the VCSEL at the desired bit rate. Data then goes through a 1 km MMF fiber and is received at the end by the optical scope. Each one of the sixteen combination of the neighboring bits is run several times to arrive

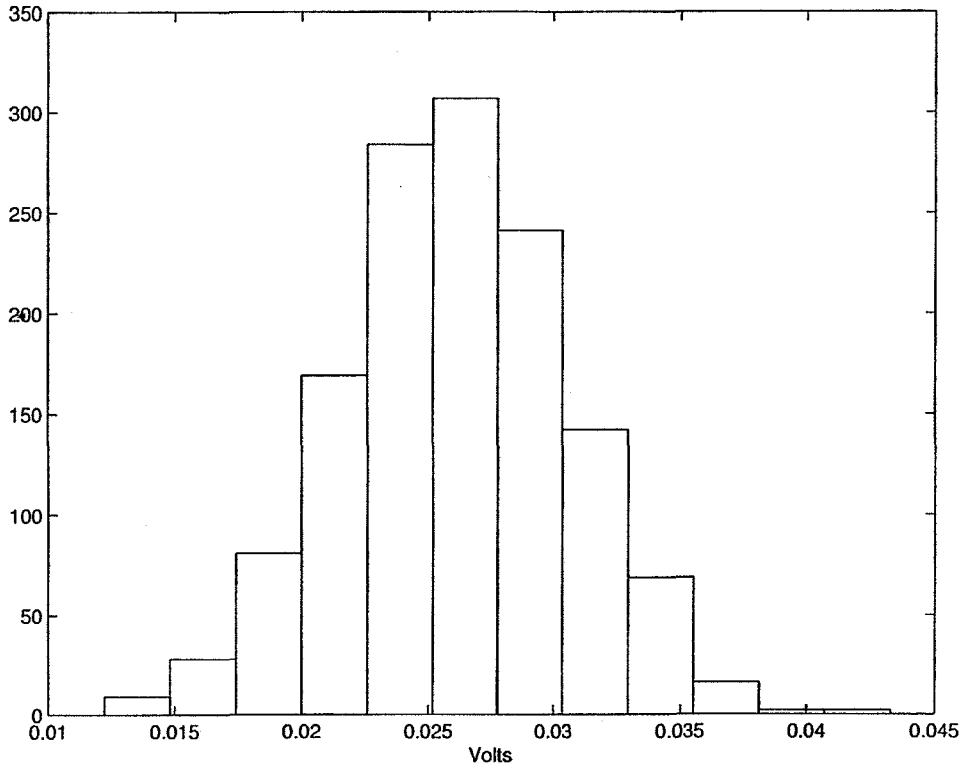

Figure 2.10: Real measurment of noise which appear Gaussian.

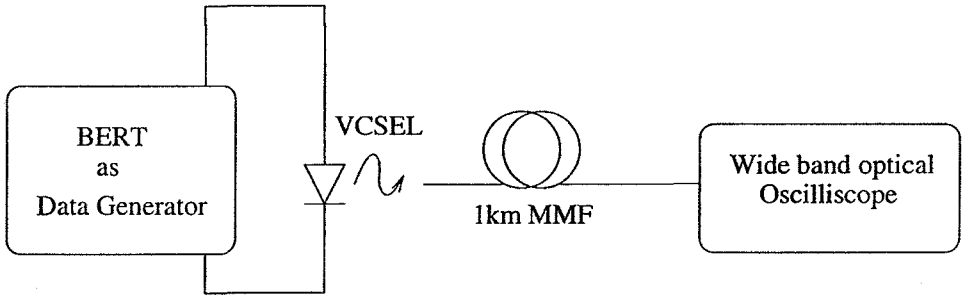

Figure 2.11: Performance evaluation experimental setup.

at the mean level of the desired bit at each possible combination. The BER can then be expressed as:

$$BER = \frac{1}{16}\sum_{i=1}^{16}\frac{1}{4}[erfc(\frac{V_{1i}-V_{th}}{\sqrt{2}\sigma}) + erfc(\frac{V_{th}-V_{0i}}{\sqrt{2}\sigma})] \qquad (2.5\text{-}13)$$

where V_{1i} is the mean of each of the ith neighborhood combinations when the desired bit is ONE, V_{0i} is the mean of each of the ith neighborhood combinations

when the desired bit is ZERO, V_{th} is the threshold level, and σ is the standard deviation of the noise.

The threshold level is determined by the following method: The sixteen possible runs are made with the desired bit of ONE, and the sixteen possible runs with the desired bit of ZERO. The threshold level is the mean of the means of the sixteen runs of the desired bit of ONE and ZERO.

2.5.2 Performance Evaluation Verification

To verify that this method of estimating the BER is good, an experiment was carried out to show the similarity of the real BER with that determined using this method.

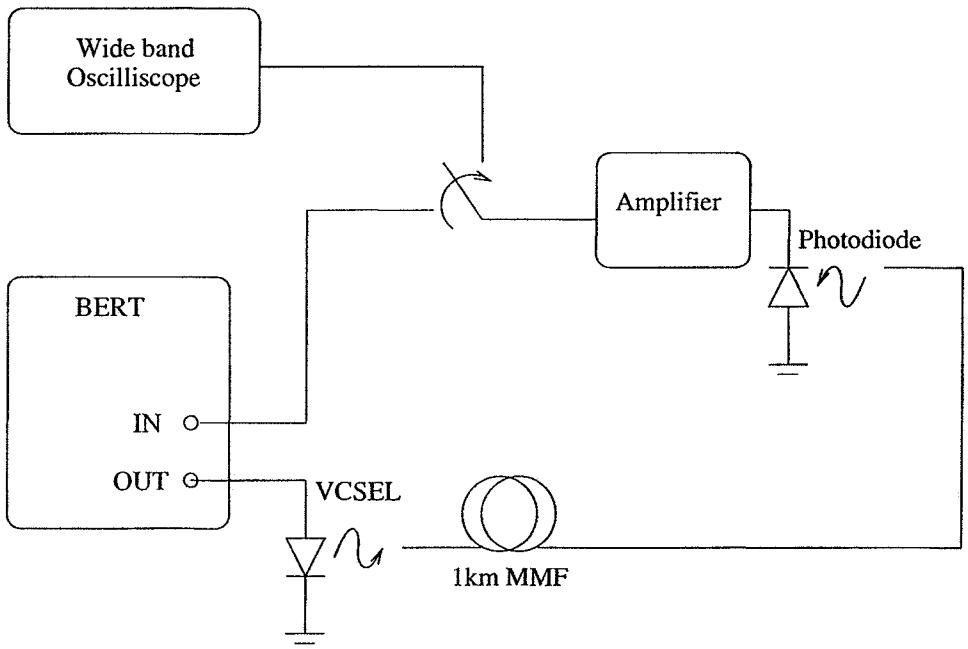

Figure 2.12: Performance evaluation verification experimental setup.

Figure 2.12 shows the experimental setup used in this experiment. The Bit error ratio tester (BERT) will send pseudo random bit sequence (PRBS) through the OUT port and receive them back through the IN port. The BERT has the ability to synchronize these bits regardless of the delay between them. The incoming bit

through the IN port is compared to a threshold level that can be controlled and the BER is monitored. By this means, a real BER measurement has been carried out. Our method of estimating the BER not through the BERT but through the wide band scope was then carried out and repeated for several bit rates. The result is shown in Figure 2.13, which shows good agreement of the two methods.

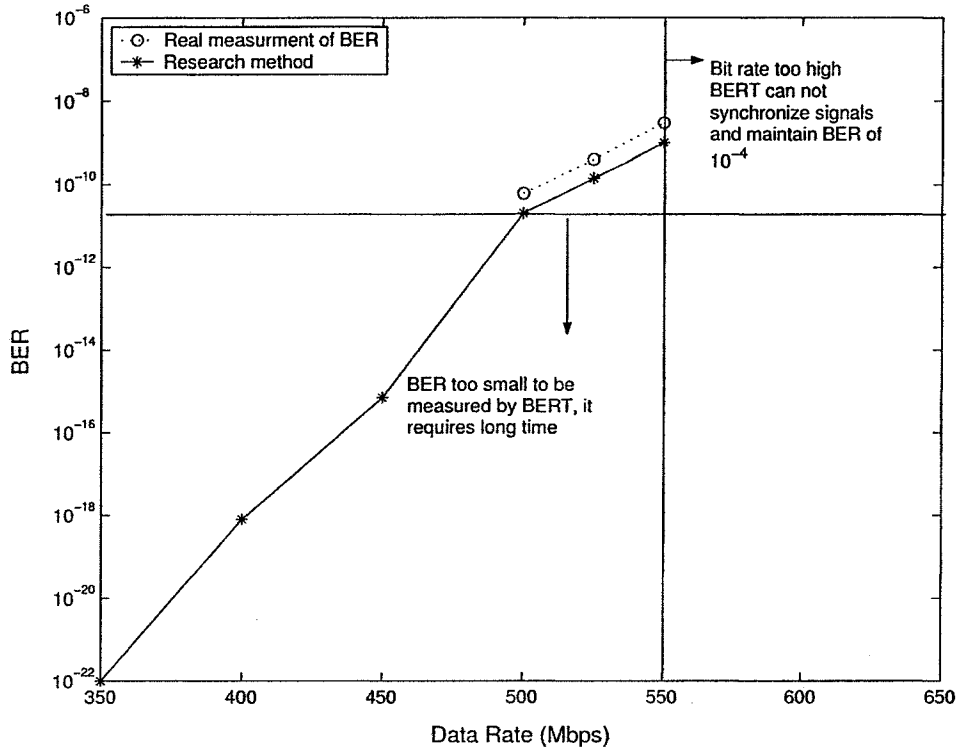

Figure 2.13: Comparison between BER measured and estimated.

In Figure 2.13 there is no reading from the real measurement below the horizontal line because too much time is required to collect sufficient data for very small error rates. To the right of the vertical line in this figure, the bit rate is too high. Consequently the ISI is so severe that the BERT cannot synchronize its output with the input while maintaining the minimum BER of 10^{-4} specified by the BERT.

2.5.3 MMF As a Linear System

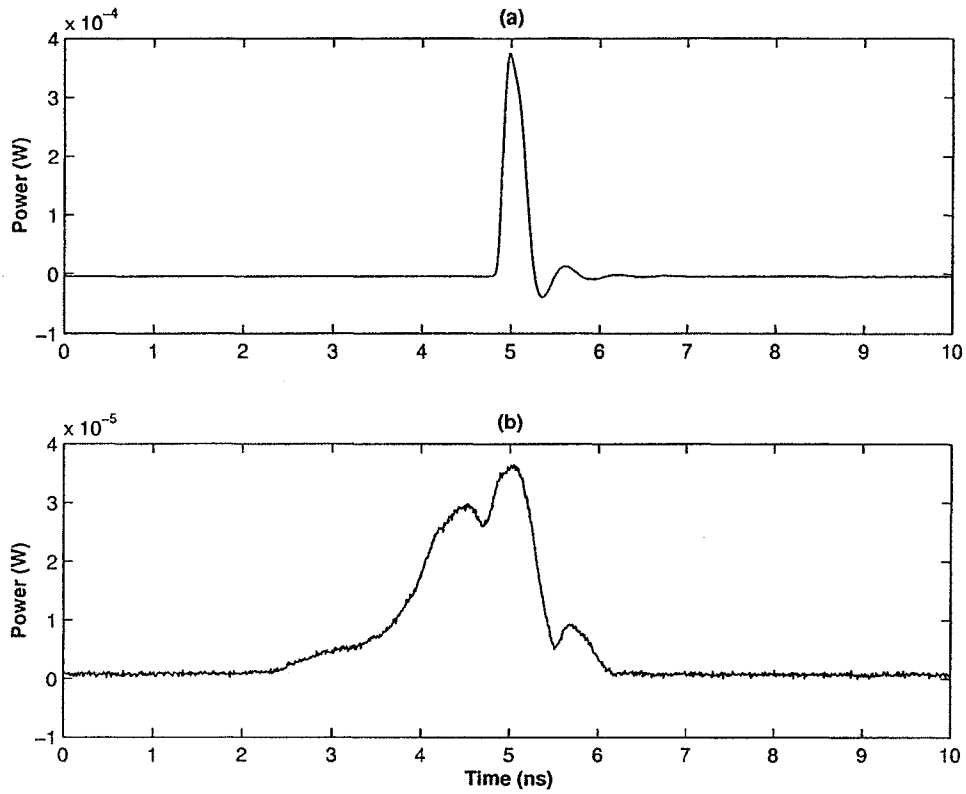

Figure 2.14: (a)The optical input pulse to the 1 km MMF, (b)The output of the fiber which represents its impulse response.

As mentioned before, to perform a simple linear equalization it is necessary to know the impulse response of the fiber channel. A simple experiment was carried out in our lab to determine the impulse response of a 1 km MMF. A bit error ratio tester (BERT) was used as a data generator to generate a short pulse that drives a commercial VCSEL. The generated gain switched optical pulse was as short of a period as 200 *psec.* The VCSEL launched this optical power into the 1 km MMF fiber and the output was measured by a wide band optical oscilloscope. Figure 2.14 shows the input pulse to the fiber and the output pulse from the fiber. The output pulse in Figure 2.14(b) can be considered as the impulse response of the fiber. The peaks of the impulse response correspond to different propagating modes, and the difference between the time at which the first and the last modes arrived is referred to as differential mode delay (DMD).

As a test of optical fiber system linearity, an experiment was carried out to measure the impulse response of the 1 km MMF fiber to the shortest pulse possible in our lab, as mentioned above. A wider pulse of 3 *nsec* was then sent and the output was measured first with the 1 km fiber and then without the fiber. The impulse response of the fiber, which is the output with the fiber of the 200 *psec* pulse, was convolved with the output with no fiber of the 3 *nsec* pulse, and then compared to the output with the fiber of the 3 *nsec* pulse. The result is shown in Figure 2.15, the comparison between the actual output of the longer pulse and the predicted output for the longer pulse. While there is some error in the prediction from this result, the question is whether or not this error is reasonable.

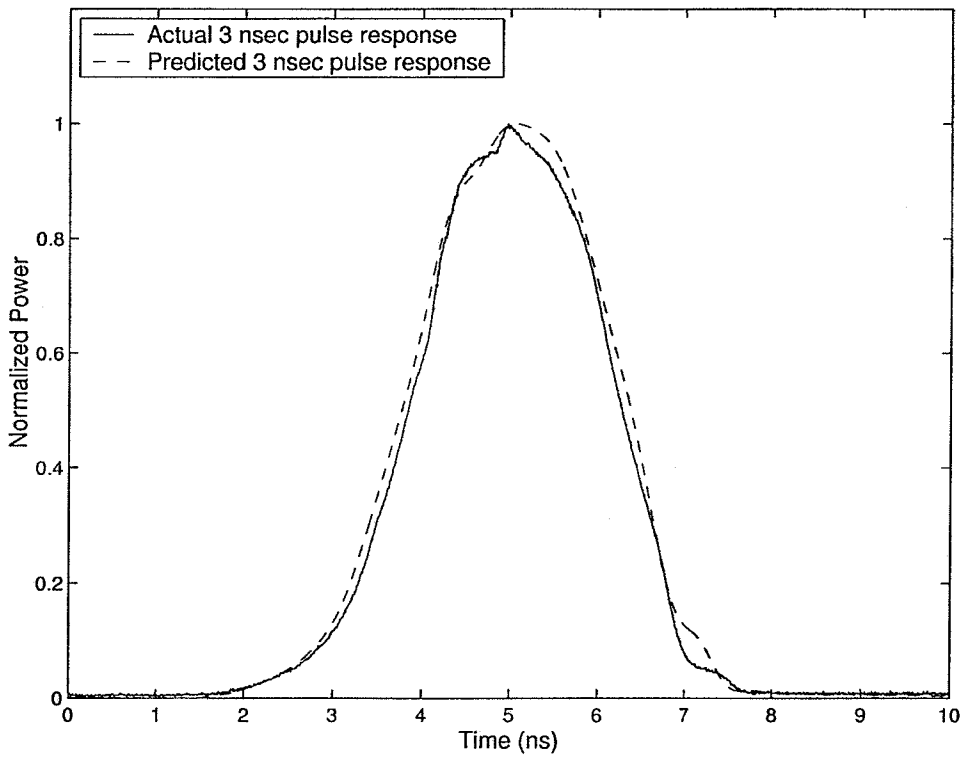

Figure 2.15: Linearity measure for 1km MMF fiber.

From the above result we computed a linear feedforward equalization with five taps for the 1 km MMF fiber at a bit rate of 1.25 Gbps and carried out a performance evaluation according to the method described in subsection 5.2.1.

Figure 2.16 shows the result of this experiment for four repetitions of the example bit sequence (00101). In this case the first ONE can be considered to be surrounded by the neighborhood $00-01$. Figure 2.16(a) shows the fiber impulse response, while 2.16(b) shows the fiber output with no equalization, which gives a BER of 0.1. 2.16(c) shows the data after equalization, which gave a BER of 4×10^{-4} at a received power of -14dBm. The bit error rate curves were produced by using the experimental setup shown in Figure 2.17, in which we introduced an optical attenuation to the received signal before the receiver to vary the received power. Figure 2.18 shows the error rate curves without equalization shown in the solid curve, and with linear equalization shown in the dashed curve which is estimated by considering all sixteen possible pattern combinations.

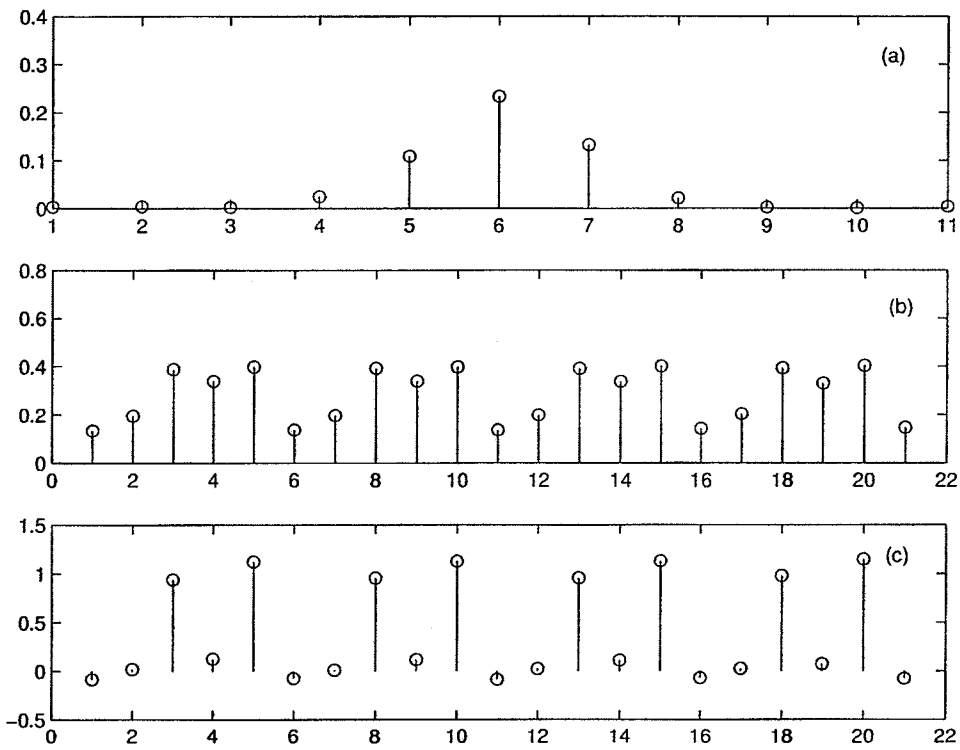

Figure 2.16: Equalization result: (a)The impulse response of the fiber, (b)The received data with no equalization, (c)Data after equalization .

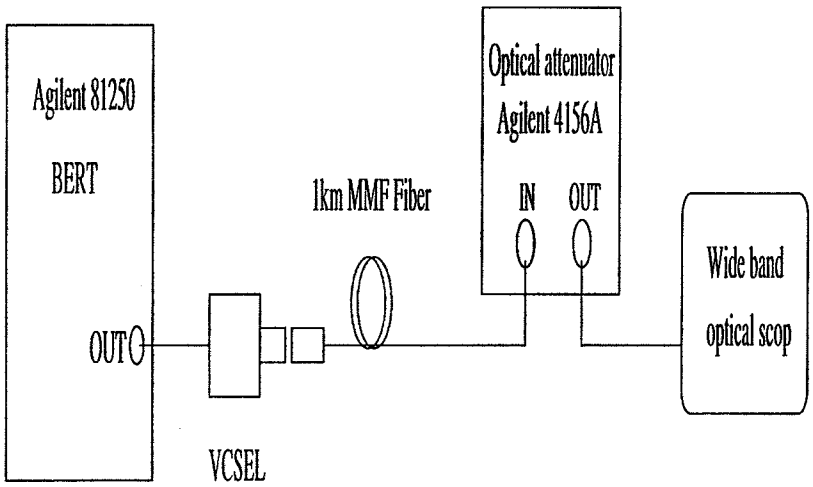

Figure 2.17: Experimental setup for producing the BER curves as a function of received power.

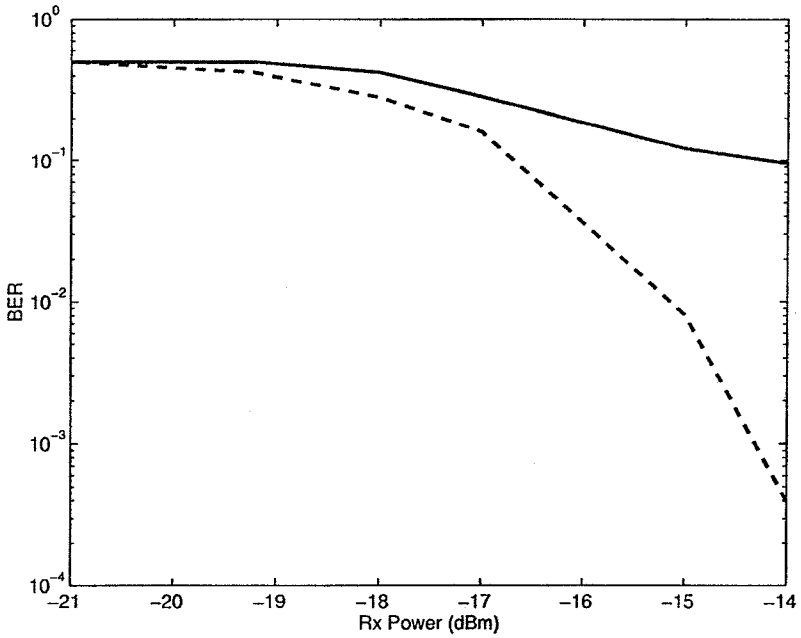

Figure 2.18: BER curves as a function of received power no equalization (solid), with linear equalization (dashed.)

Chapter 3

FIBER IMPULSE RESPONSE

3.1 Introduction

When a signal is transmitted through a channel, the channel should have a bandwidth that can accommodate the bandwidth required by the signal. The channel bandwidth can be derived from its impulse response.

A moderate number of papers have been reported in the literature dealing with MMF fiber impulse response or effectively the bandwidth of the fiber. Fiber optic channels with perfect mode mixing are usually modeled by a Gaussian impulse response[6]. Few publications have been presented in the literature that relate the bandwidth of the GIMMF fiber to the optical source being used, either light-emitting diode (LED) or vertical cavity surface-emitting laser (VCSEL). It has been shown that GIMMF bandwidth is sensitive to optical power launch conditions, which in turn depends on the source type and coupling[23]-[28].

3.2 Launch Condition and Fiber Impulse Response

3.2.1 Optical Source Effects

MMF fibers were originally implemented to be used with LEDs. LEDs produce an optical signal that has a large linewidth compared to lasers, which means that LEDs produce more pulse broadening than lasers. LEDs also produce a broader spatial beam than a laser (see Figure 3.1), which leads to overfilled launch (OFL).

To reach the OFL condition, the numerical aperture (NA) of the beam emitting from the source should be higher than the NA of the fiber, which leads to comparable excitation of all modes of the fiber. The corresponding bandwidth is termed OFL bandwidth, which is a low but stable bandwidth in the sense it is insensitive to source to fiber misalignment.

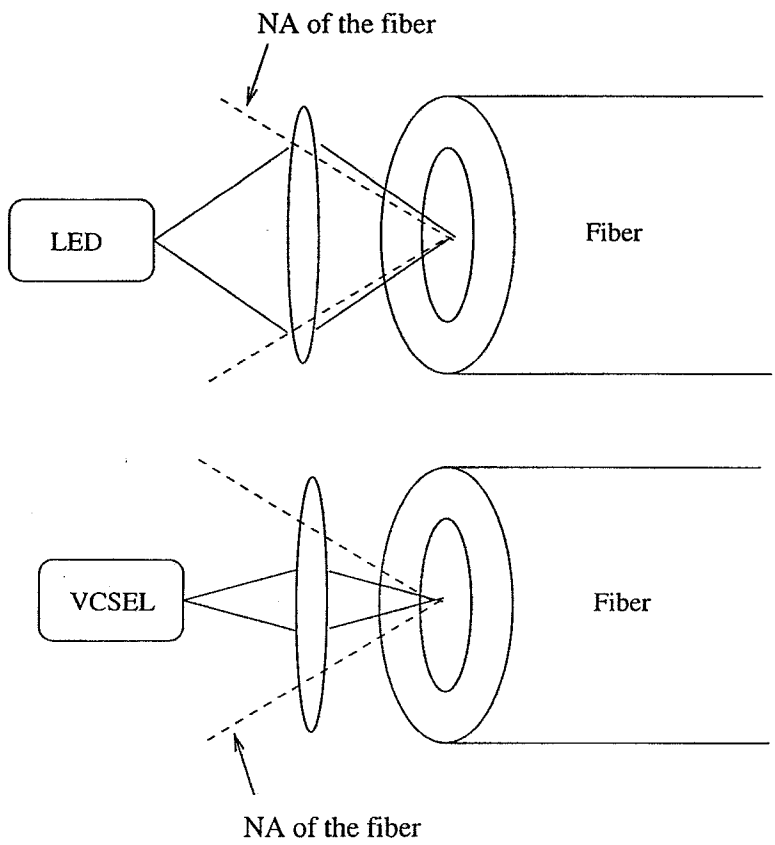

Figure 3.1: LED used as source (upper) which produce OFL, and VCSEL (lower) which produce narrow beam.

When using a laser-based transmitter with GIMMF fibers, a narrow beam is generated . This produces a small spot size, which leads to the fact that on-axis power excites a selection of lower order modes which face more pulse broadening[23] due to the common defect of having a distinct peak or dip in the index of refraction profile at the center of the fiber, as illustrated in the inset of Figure 3.2.

The body of Figure 3.2 shows the dependence of bandwidth on the source to fiber offset and launch angle for two different 850 nm sources to fiber offsets, based on data from[24]. For example, if there is a tilt of 2-3.5 degrees or an offset of $3\mu m$, the bandwidth will be less than the OFL bandwidth, which is in this case 366 MHz.km.

Since the bandwidth is sensitive to launch angle, it is important to consider which group of modes is being excited by laser sources.

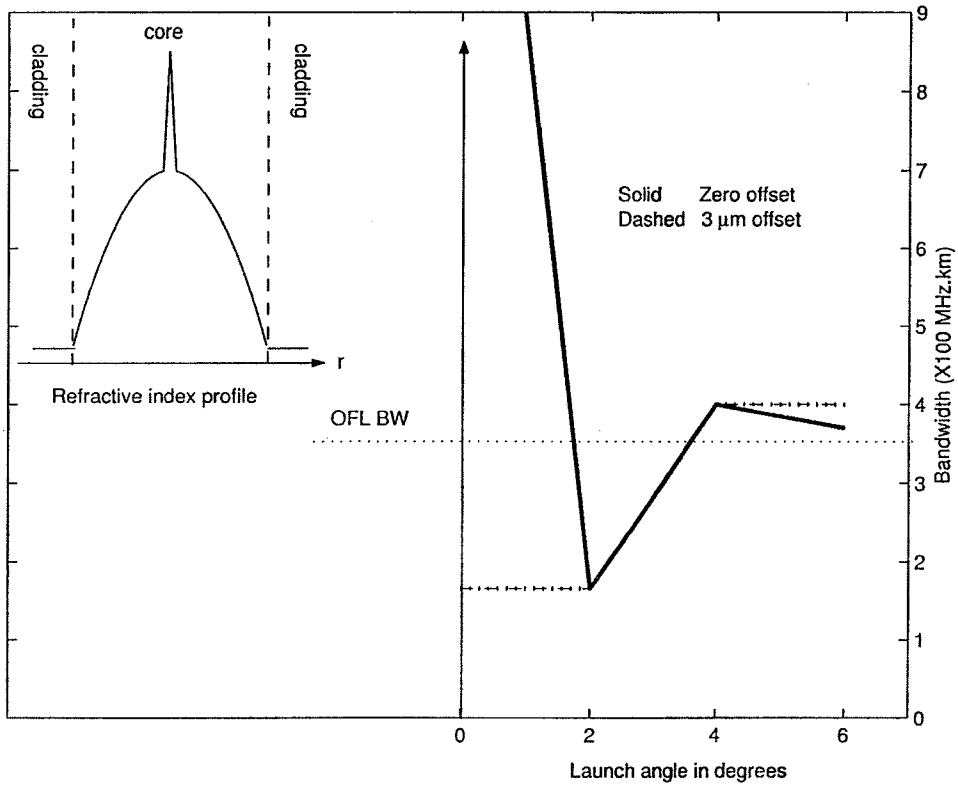

Figure 3.2: Refractive index profile for GIMMF fibers with a central peak (inset), Bandwidth dependence on angle of launch and laser to fiber offset (reproduced after[24] for 850nm transmission.

3.2.2 Launch Condition and Bandwidth

Since GIMMFs have a large number of propagating modes, it is useful to consider the impulse response of each mode rather than the overall impulse response

of the fiber, meaning that there exists a unique impulse response for each existing mode and the resulting fiber impulse response depends on which modes have been excited. To understand the structure of the modes of the GIMMF with respect to the configuration of the launch employed, and for the sake of simplicity, a detailed discussion is presented in the next section. Here, we shall consider only the meridional modes represented by rays that cross the fiber axis and represented by EM field distributions that have no azimuthal dependence . Let us parameterize the fiber modes by the maximum distance the ray travels away from the fiber axis before being refracted back by graded index. This maximum ray deviation from the axis is the variable a in Figure3.3.

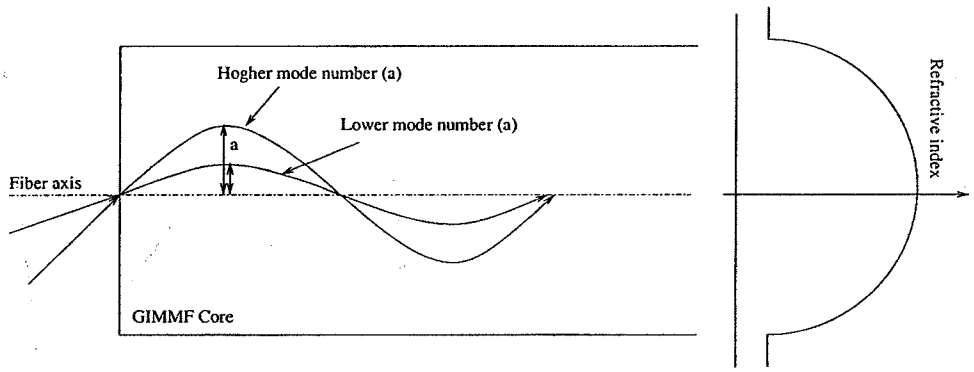

Figure 3.3: parametrization of GIMMF meridional modes.

By carrying out geometrical optics modeling to the beams from a source entering the fiber at any place (offset) and any angle, using Snell's law to calculate the distance (a) using a discrete version of a finite number of constant refractive index layers, and a common power law refractive index profile, the resulting mode numbers i.e., variable (a) are shown in Figure 3.4 as a contour plot with respect to position on the face of the fiber and angle. As the color of the contour becomes lighter gray, the mode number increases; these modes are termed higher order modes. Hence, as we get close to the fiber axis with shallow angles we excite lower order modes, and vice versa.

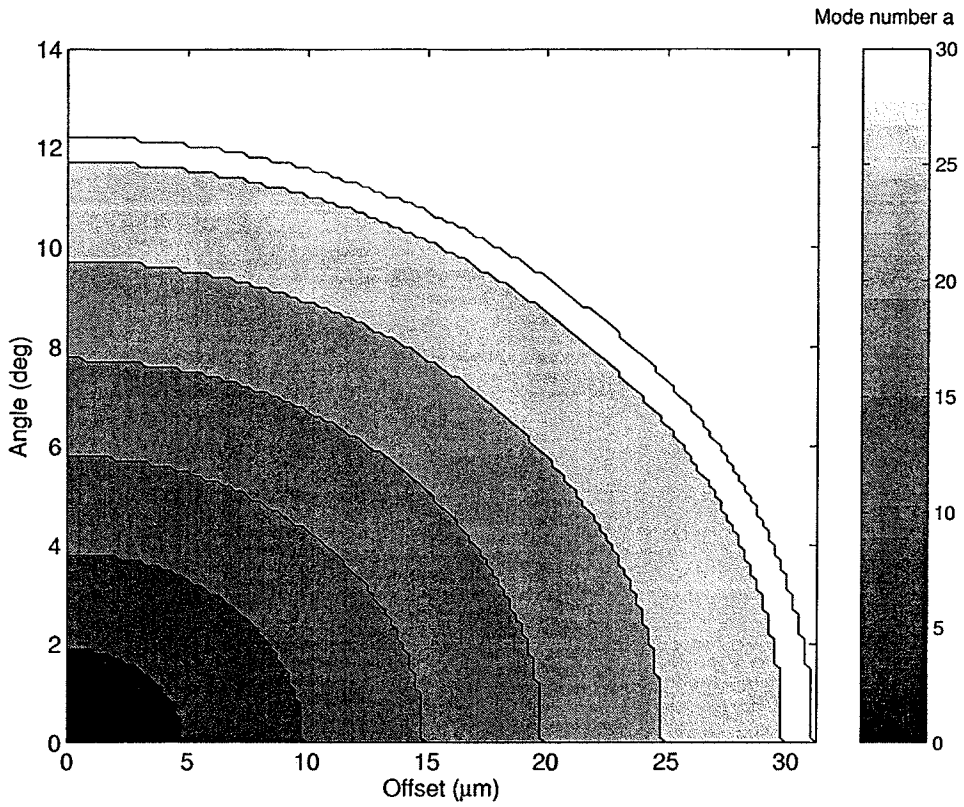

Figure 3.4: Contour plot showing GIMMF meridional mode numbers with respect to offset and angle of launch.

3.3 Parametrization of Graded Index Multimode Fiber Modes

In this section, a discussion of parametrization of the GIMMF modes will be presented. First we parameterized the GIMMF modes by considering only the meridional modes, as discussed briefly in the previous section. In the following subsections, a detailed discussion about the parametrization and modeling of the modes is presented.

3.3.1 Parametrization of Meridional Modes

When we first considered the parametrization of the GIMMF modes, we considered only the meridional modes. A model of the fiber was created by examining slices of small hollow cylinders that have a constant refractive index. If these cylinders are summed up, they yield a fiber structure with a power law refractive index

profile; i.e a step-wise approximation of the refractive index profile. The ideal, smooth refractive index profile used here is described in equation 3.3-1.

$$n(r) = [n_1^2 * (1 - 2\Delta(\frac{r}{f})^2)]^{1/2} \tag{3.3-1}$$

Where n_1 is the refractive index at the center of the fiber, it has a typical value of 1.5. $\Delta = 0.01$ is a typical value, r is the radial position (offset), and f is the radius of the fiber which is 62.5 μm. Parametrization here is achieved by calculating how far the ray should travel radially from the fiber axis before it bends by total internal reflection. By using geometrical optics with Snell's law and taking into account the refraction due to the interface between the air and the fiber, the resulting mode number (a) as a function of the offset and the angle as described before is shown in Figure 3.4 as a contour plot, whereas the contour gets lighter as the distance from the fiber axis gets higher, and this becomes higher order mode.

3.3.2 Parametrization of Meridional and Helical Modes

Considering only the meridional modes requires the assumption of a center launch, which means that the center of emission is the same as the center of the fiber. However, if the launch is not center launch, there should be a third dimension that takes care of the non-centered launch other than the offset and angle, which would be another angle. Figure 3.5 inset shows the parameters used here to describe the resulting excited modes, where r is the radial position (offset), θ is the angle between the fiber axis and the projection of the ray to the two-dimensional plane containing r and the axis, and ϕ is the angle between the fiber axis and the projection of the ray to the plane containing the fiber axis which is orthogonal to the line between the axis and r. As a description of Figure 3.5, there are four types of modes existing in the graded index fiber. One is an axial mode that exists if the offset is zero and the angle with respect to fiber axis is zero. The

second type is the meridional mode, which passes through the fiber axis and exists if the angle ϕ is zero, or if offset is zero and the angle of launch with respect to the fiber axis is non-zero. The third mode is helical and does not pass through the fiber axis but rather travels in a trajectory similar to a helix. If the angle θ is zero the helix would be circular, and if θ is non-zero the helix would be elliptical, yielding the fourth mode category. Circular helical modes travel with a constant offset and thus with the same refractive index as axial modes, while elliptical helical modes and meridional modes travel through different refractive indices.

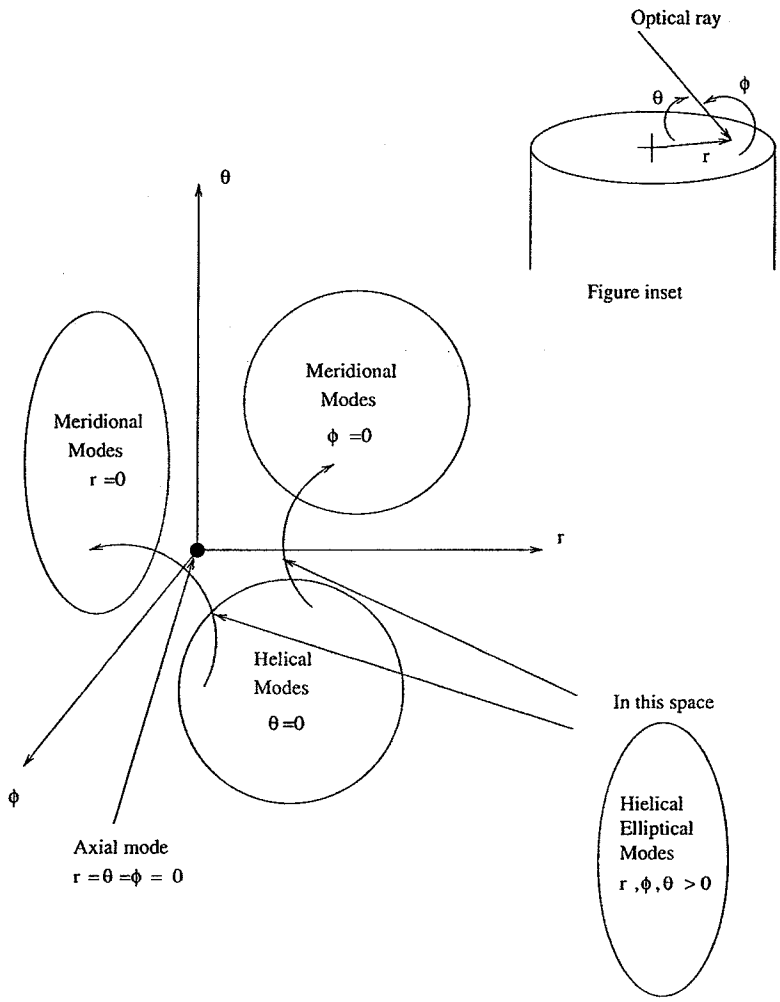

Figure 3.5: parametrization of GIMMF axial, meridional, and helical modes with three dimensions shown in inset.

3.3.3 Modeling of GIMMF Modes

As mentioned previously, when we first thought of characterizing the modes of the fiber we considered the distance the ray takes from the fiber axis to bend by total internal reflection. Later the matter became confused, and it was evident that if there exists a helical mode this method is useless since the helical mode will not cross the fiber axis. An alternative method is introduced here which characterizes every mode by some quantity that applies to all mode categories. This quantity is the travel time i.e., the time required by the ray to travel a certain longitudinal distance. This time is normalized to some distance, not in the direction of propagation but in the longitudinal direction along the fiber axis. It is worth commenting that this travel-time is related to the longitudinal phase velocity associated with the propagation factor, β.

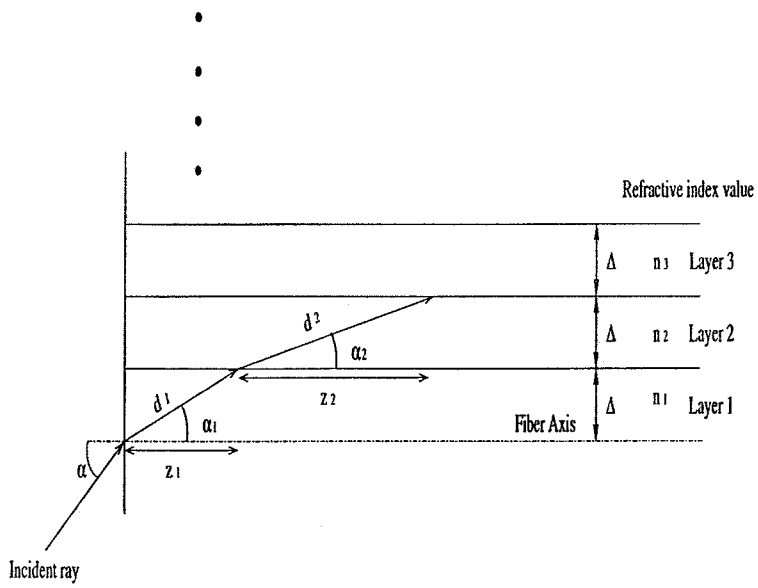

Figure 3.6: parametrization of GIMMF modes by the travel time.

This is done by considering a refractive index profile, then disecertizing this profile to a finite number of hollow cylinders with a constant refractive index. When

the refractive index is constant the speed of the ray can be calculated by the speed of light divided by the refractive index, and consequently the travel time is the ray speed divided by the distance. Figure 3.6 shows how the fiber core is divided into a finite number of layers (cylinders) to approximate the actual refractive index profile, and how the rays travel through these layers. By considering Snell's law which states that

$$n_1 \sin(\theta_1) = n_2 \sin(\theta_2). \tag{3.3-2}$$

As the ray enters the fiber from the air its angle α changes to α_1, and hence the distance d_1 this ray would travel is calculated from the trigonometry as

$$d_1 = \Delta / \sin(\alpha_1). \tag{3.3-3}$$

Where Δ is the size of the step chosen to approximate the refractive index profile, as Δ decreases the approximation becomes more accurate. From this, it is known that the time required by the ray to travel this distance of d_1 would be

$$t_1 = c/(n_1 d_1), \tag{3.3-4}$$

where c is the speed of light in a vacuum of $3 \times 10^8 m/s$ and n_1 is the refractive index of layer number 1. Here we are concerned with the distance d_1 to calculate the time but we need to normalize this time to the longitudinal distance of z_1 (see Figure 3.6). These steps are repeated for the ray to go from layer 1 to layer 2, and t_2, and z_2 are calculated. This process is repeated until we arrived at a total internal reflection from one layer to the other (say layer n). The process is then stopped and the times are added, so the total time to travel a distance of $z_{tot} = z_1 + z_2 + .. + z_n$ is $t_{tot} = t_1 + t_2 + .. + t_n$. Following this, all modes with different offsets or angles are normalized to the same length, and then the travel time becomes unique to each ray. Note that we will use this model to find the effects of the source nonlinearity in Chapter 5.

Chapter 4

FIBER BANDWIDTH ENHANCEMENT

4.1 Introduction

Non-idealities in graded index multimode fiber used in local area networks result in excessive differential mode delay, which is the variation in propagation delay that occurs because of the varied group velocities of different modes. For example, small area launches at the center of MMF from small, single transverse mode lasers[25] or single mode fiber (SMF) can result in non-equilibrium coupling into modes that propagate near the MMF axis, which often has undesired refractive index excursions[26]. Various spatial filtering methods have been investigated to enhance MMF bandwidth. Hass and Santoro proposed a mode filtering scheme to excite lower order modes and suppress spurious modes at the receiver end[29]. Raddatz and co-workers developed an offset launch technique whereby the optical power is launched in a localized area offset radially from the defective refractive index profile at the center of the fiber[7]. This offset launch technique was incorporated into the IEEE 802.3z Gigabit Ethernet standards to allow single mode 1000Base-LX transmitters to be used with MMF. This is done by specifying the use of an offset jumper using a SMF with the core offset from the axis of the connector ferrule by 17 to 23 μm at the end, to be connected to the MMF[27] to purposely introduce a non-concentric alignment. In addition to modifications to fibers, specialized source geometries have also been considered. Laser devices with an annular

emission area concentrically aligned to MMF excite higher order modes with similar propagation constants, which increases the system bandwidth[23]. The central emission area of the lasers reported in that work were blocked to prevent coupling into the low-order axial mode.

Such spatial filtering approaches result in improved bandwidth but require non-standard devices or fiber assemblies that may increase cost either due to greater complexity or lower volumes associated with customized components. For example, virtually no Gigabit Ethernet offset jumpers are employed due to the cost of the jumper assembly as well as the prevalence of multimode 1000Base-SX transceivers over single mode 1000Base-LX transceivers. However, as lower cost 1300 nm source technologies emerge[30], it is desirable to investigate low cost approaches to using the same single mode sources with both SMF and installed MMF without excessive DMD penalties. Accordingly, this section reports experiments showing a simple longitudinal separation of a SMF from a MMF that restores the MMF 3dB bandwidth to the value obtained using conventional multimode sources without significant decrease in the total coupled power. Because the longitudinal separation can readily be achieved using existing transmitter optical subassemblies (TOSAs), the approach can be implemented very simply by employing a spacer or stopper within the TOSA.

4.2 Simple Launch Technique for Bandwidth Enhancement

4.2.1 Experiment

The impulse response of a MMF was investigated as a function of the launch position of a SMF using the experimental set-up of Figure 4.1. Isolated $\sim$ 750 ps duration electrical pulses at a repetition rate of 41.7 MHz from an Agilent 81250 data generator were used to gain-switch VCSELs producing $\sim$ 200 ps optical pulses in a SMF from OZ optics part number SMJ-8LC-633-4/125-1-4. The commercial

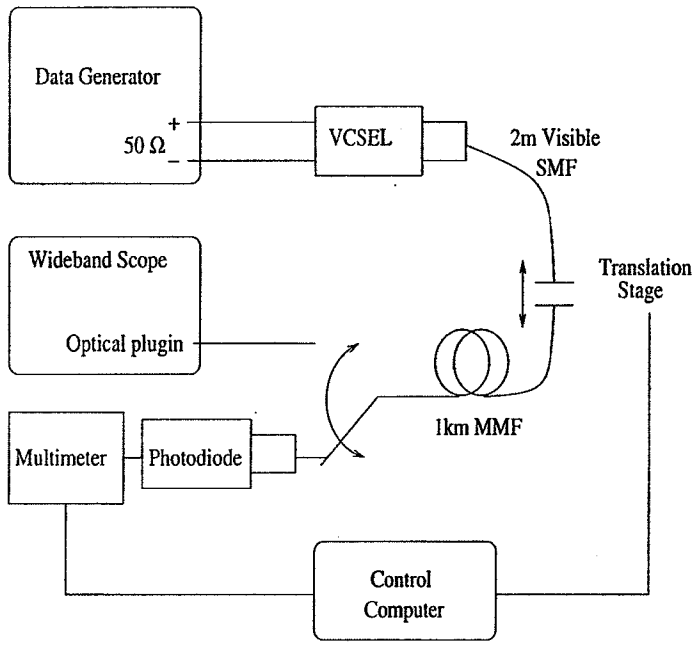

Figure 4.1: Experimental setup.

850nm VCSELs in the transmitter optical subassembly (TOSA) packages were multimode, oxide-confined structures specified for 2.5 Gb/s operation. Although the VCSELs emitted multiple transverse modes, the 4 μm core diameter SMF resulted in a well-controlled single transverse mode being launched into a 1 km long, 62.5/125 μm graded-index MMF. The separation between the connectorized ends of the SMF and the MMF was controlled using a motorized micropostioning translation stage. An initial concentric alignment of the SMF and MMF connector ferrules was established using a coupling sleeve. Concentric alignment was maintained by translating only the SMF along its axis, creating a calibrated gap between the ends of the fibers. The output of the MMF was connected directly to either a low-speed photodiode to measure the received average power or to an Agilent model 86100A digital oscilloscope with an FC optical channel plug-in (model 86101A) to measure the temporal shape of the output pulse. The bandwidth of the optical channel was specified to be at least 3GHz. Average power and output pulse forms were measured as a function of the separation between the SMF and

MMF using automated computer control of the translation stage. The range of separation distances studied was 0 to 2400 μm for average power measurement and 0 to 450 μm for temporal waveform measurement.

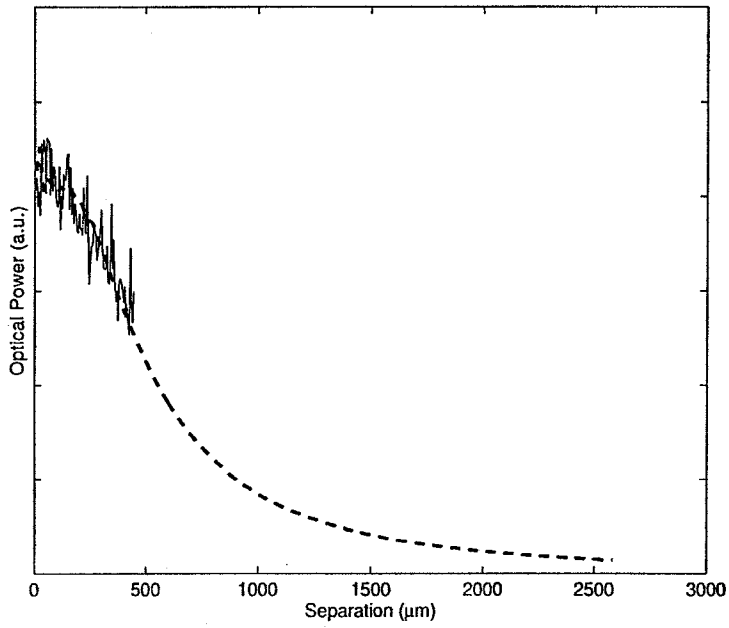

Figure 4.2: Total average power as a function of the separation distance d: from average power meter(dashed) , and integration under the curve from the temporal measurement (solid).

4.2.2 Measurement Results

Figure 4.15 shows the total received average power as a function of the distance of separation, *d*. The dashed line is from an average power meter, and the solid line is from the integration under the temporal pulses from the wide band scope with good agreement between the results. As expected, in Figure 4.16 the total power fits the area under Gaussian beam as a function of separation distance with beam waist equal to the mode field diameter of the single mode fiber of 4.5 μm[31],[32]. The total power starts to drop at 150 μm, where the outer region of the diverging beam from the SMF, whose NA is 0.15, falls outside the NA of the 62.5 um core diameter of the MMF, which corresponds to a radius of 22 μm (see

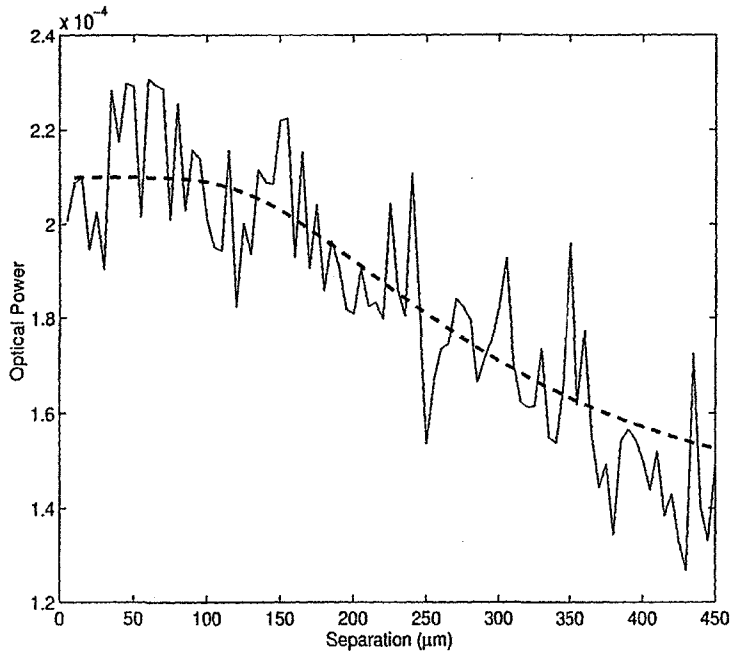

Figure 4.3: Total average power as a function of the separation distance d (solid), and Gaussian beam fitting (dashed).

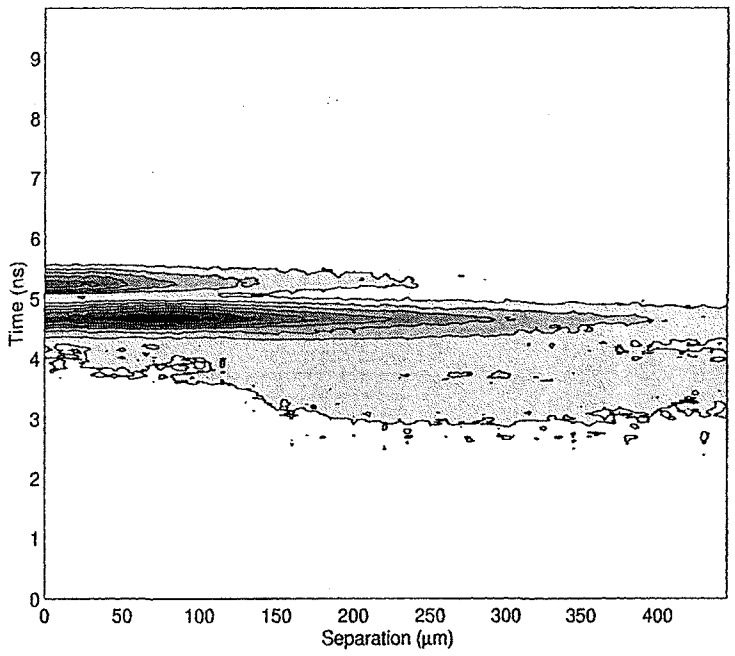

Figure 4.4: Temporal response contour plot as a function of the separation distance d.

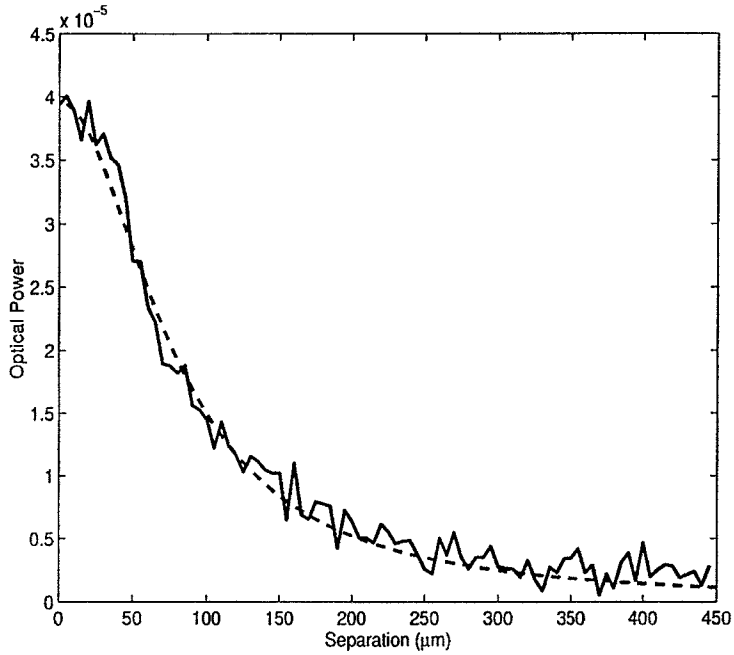

Figure 4.5: Average lower order mode power as a function of the separation distance d(solid), and Gaussian beam fitting(dashed).

Figure 4.19), in agreement with the geometrical model. This fiber is believed to have a common defect of a small region of abnormally high refractive index near the MMF fiber axis. A fraction of the total optical power from the SMF is launched into this region and is expected to result in slow, low order modes that contribute to increased DMD[26]. The amount of power coupled into this slow mode region also decreases with separation distance, as the area under the Gaussian beam as a function of separation distance with beam waist equal to the mode field diameter of the single mode fiber, as illustrated in Figure 4.18. The area under Gaussian beam as a function of separation distance can be expressed as

$$P_{fit} = \int_0^a \frac{r}{w(d)^2} \exp\left(\frac{-r^2}{(2w(d))^2}\right) dr \tag{4.2-1}$$

where

$$w(d) = w_0 \sqrt{1 + \left[\frac{\lambda d}{\pi w_0^2}\right]^2} \tag{4.2-2}$$

w_0 is the beam waist which is the mode field diameter of the SMF. An estimate of the diameter of the slow mode region can be found from the limits of integration used in the fitting $(2a)$, which yields $4\mu m$.

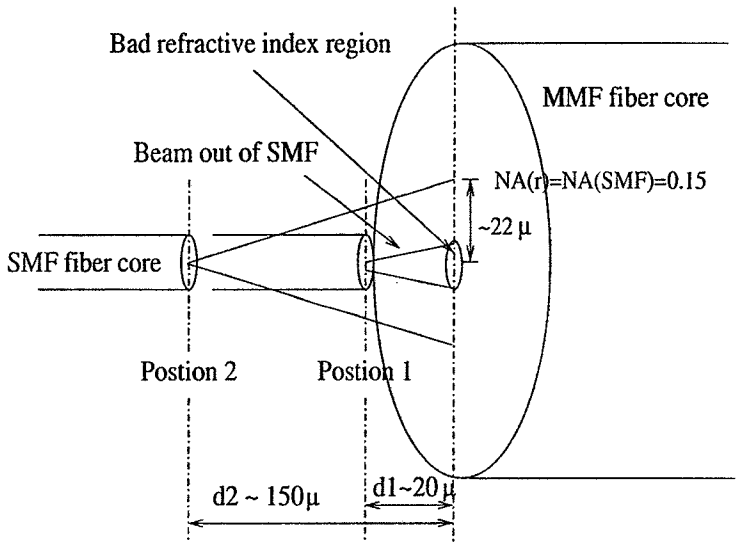

Figure 4.6: SMF to MMF separation configuration.

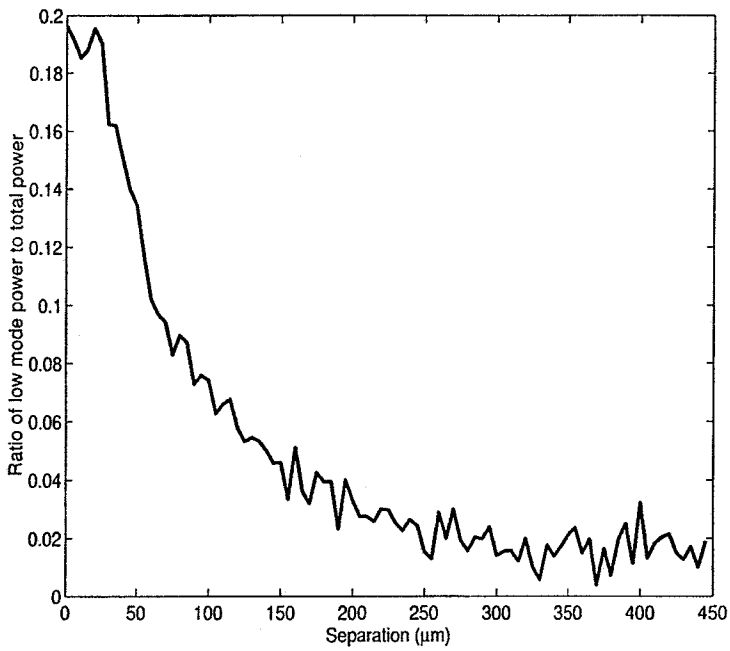

Figure 4.7: Ratio of slow mode power to total power.

In order to measure the amount of power coupled into the slow mode region, it is necessary to temporally resolve the optical output from the MMF. Figure 4.17 shows the impulse response of the MMF for a few specific fiber separations. The slow order mode peak arrives at 5.2 ns after the arbitrary time origin, while the main peak arrives 0.7 ns earlier. The trends in the temporal power distribution as a function of separation distance are clarified in Figure 4.17 as a contour plot with coordinates of time and separation distance. As the separation distance increases, the slow mode peak decreases in power, while the main mode peak first increases to a maximum at a separation distance of about $d = 70\mu m$ and then decreases with increasing separation. The power in a still faster mode increases slightly for separation distances of about $d \sim 150\mu m$. The dependence of the integrated power in the slow mode peak on separation distance is shown in Figure 4.18. The power in the slow mode starts to decrease for $d > 17\mu m$, validating the geometrical model of power coupled into the slow mode region. An estimate of the diameter of the slow mode region of $4\mu m$ is calculated from the geometrical arguments (see Figure 4.19), which agrees with the estimate found from the fitting. For $d < 17\mu m$, the amount of slow mode power varies only by 10% with separation distance. At zero separation, it is estimated that 20% of the power is coupled into the slow modes. Even though almost the entire 4.5 μm mode field diameter falls within the estimated $4\mu m$ diameter of the slow mode region, not all of the power is coupled into the slow modes, presumably because the large divergence angle portion of the beam from the SMF launches into meridional rays with trajectories that depart significantly from the fiber axis.

4.2.3 Application and Discussion

Beyond certain separation distances, both the slow mode power and the total power decrease according to the Gaussian beam fit, as shown in Figures 4.15 and

4.18. Large separation distances minimize the amount of slow mode power but also significantly decrease total power. However, for separation distances in the range $50\mu m < d < 150\mu m$, the total power is nearly unchanged, while the slow mode power decreases as Gaussian, allowing decreased DMD while maintaining total coupled power. Based on the plot of the fraction of slow mode power shown in Figure 4.21, the separation distance that minimizes the DMD is 125 μm. Figure 4.20(a) shows the measured impulse response at this optimum separation distance, as well as for no separation and direct coupling of the multimode VCSEL TOSA to the MMF. The Fourier transforms of the impulse responses in Figure 4.20(a) have been computed in order to determine the frequency response of the MMF under various launch conditions, as shown in Figure 4.20(b). Direct coupling of the SMF to the MMF results in a reduction of the 3dB bandwidth distance product of this fiber from 200 MHz-km to 130 MHz-km. This bandwidth reduction is well-known and is one reason why single mode transmitters are not directly coupled to MMF. However, by simply introducing a separation of 125 um between the SMF and MMF, the original bandwidth of the multimode laser coupled directly to the MMF is restored. One concern here is the possibility of their being any misalignments of the SMF from the MMF at this optimum distance of 125 μm. Experimental results that purposely introduce SMF to MMF lateral misalignment at the longitudinal separation of 125 μm show quite stable average power until a reasonable offset of 15 μm.

Thus, an improved single mode to MMF launch can be achieved by appropriate separation of a single mode source from the MMF studied here by use of a spacer or stops in a coupling sleeve or TOSA barrel. Reflections due to the introduced gap are not an issue and can be solved by AR coating or index-matching fluid. It should be possible to implement this method at significantly lower cost than the construction of an offset launch jumper and to a large extent it satisfies the

encircled-flux criterion since the percentage of power inside the 15 μm and 4 μm circles are 85 % and 25 % respectively at the optimum distance of 125 μm.

While the experiments here have used single mode fiber with various separations to control the launch into this MMF, similar results are expected for separations of single transverse mode lasers or images of single transverse mode lasers from the end of this MMF as is presented in the next section, There is no concern about mode selective loss since only a single mode is launched. It is noteworthy that this configuration is not a radial overfilled launch (ROFL) which is considered to be a bad launch in terms of bandwidth. The ROFL is defined as introducing a longitudinal displacement between the source and the fiber that would reduce the total power by 0.5 dB which corresponds to a distance of about 220 μm in our experiment. The proposed launch is a radially concentric launch but not overfilled. It is important to note that these results are for one specific fiber and that discussions with others who work in the same field indicate that there exist certain profiles of MMF for which this launch might not work so well. As a continuation for this work a more detailed study for the statistical distribution of MMF index profiles and its impact on the effectiveness of the simple longitudinal separated launch is proposed as future work.

4.2.4 Summary

The experiments described here demonstrate that when multimode VCSEL is connected to a SMF to resemble single mode lasers, the corresponding MMF fiber bandwidth is reduced by 70 %. A simple operation of separating the SMF fiber from the MMF fiber at an optimum distance will regain the multimode bandwidth without losing more than 10% of the total power, keeping in mind that this scheme will maintain a simple center-launching configuration.

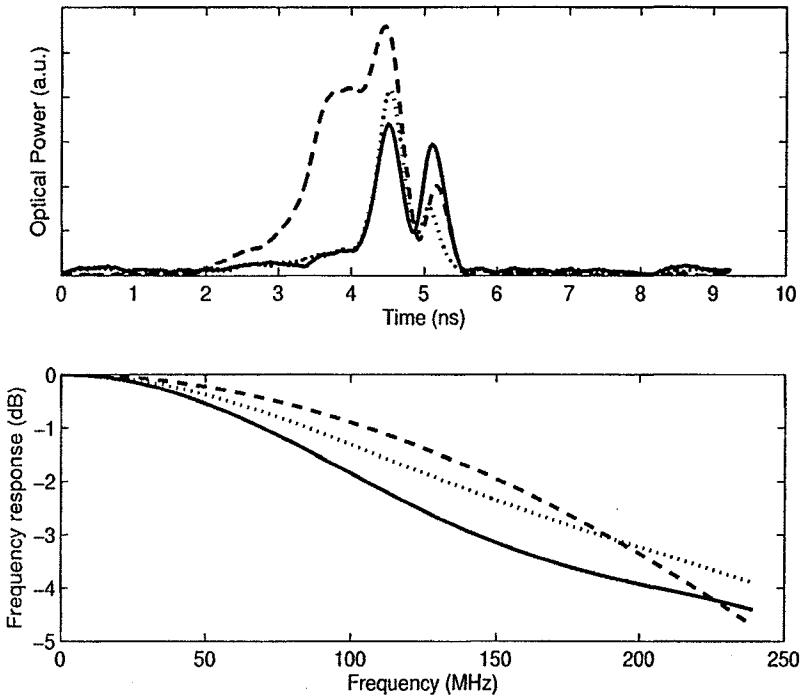

Figure 4.8: (a)Impulse response for $d = 0$ (solid), at optimum distance of $125\mu m$ (dotted), and the multimode impulse repose out of multimode VCSEL directly to the multimode fiber (dashed), (b)Frequency responses for $d = 0$ (solid), at optimum distance of $125\mu m$ (dotted), and multimode VCSEL directly to the multimode fiber (dashed.)

4.3 Simple Launch Technique using Single Mode Laser

As mentioned in the previous section, this launch configuration can be used with single mode lasers and will enhance the bandwidth of the MMF fiber. This section discusses the experiment carried out with the use of a single mode laser with high power of up to 1 mW. This high power makes it possible not only to calculate but also to measure the bit error rate performance of the system.

4.3.1 Experiment

The experimental setup was the same as that of the previous section however, instead of using a multimode laser and a single mode fiber, a single mode laser from a major VCSEL manufacturer was used. The VCSEL was specified to be single

transverse mode with a high power of up to 1 mW, ion implanted, and its output beam focused using a spherical lens which adjusts the focus to about 1.5 mm above the lens. The MMF fiber tip was manipulated by a three-axis motorized translation stage until the power coupled into the MMF was maximized. This position of maximum power is considered the zero position, or where the fiber axis is in the focus of the single mode laser. The output of the MMF was connected directly to the wide band scope. Output pulse forms were measured as a function of the separation between the single mode laser and MMF using an automated computer control of the translation stage and the scope.

4.3.2 Results

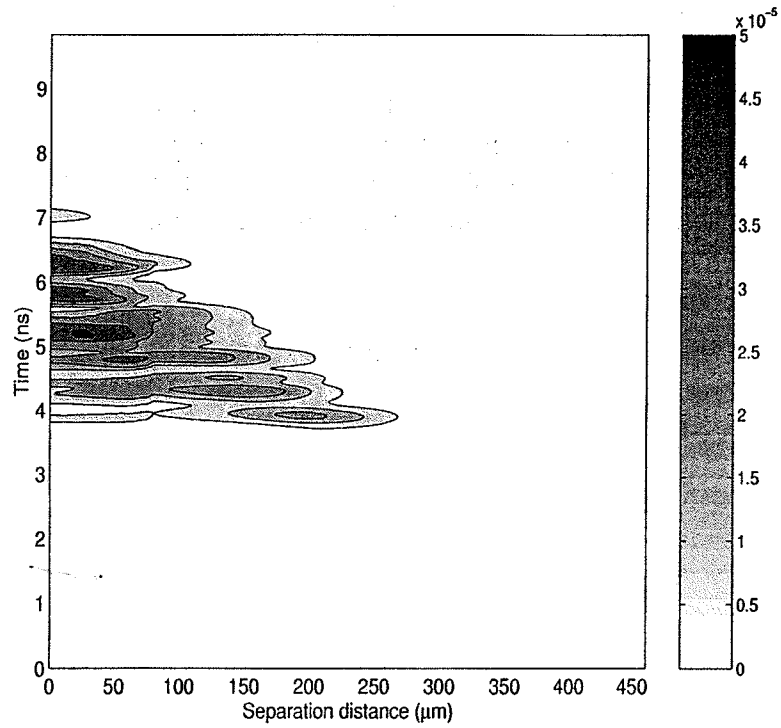

Figure 4.9: Single mode laser to MMF temporal response contour plot as a function of the separation distance .

Figure 4.9 shows the trends in the temporal power distribution as a function of separation distance in the form of a contour plot with coordinates of time and

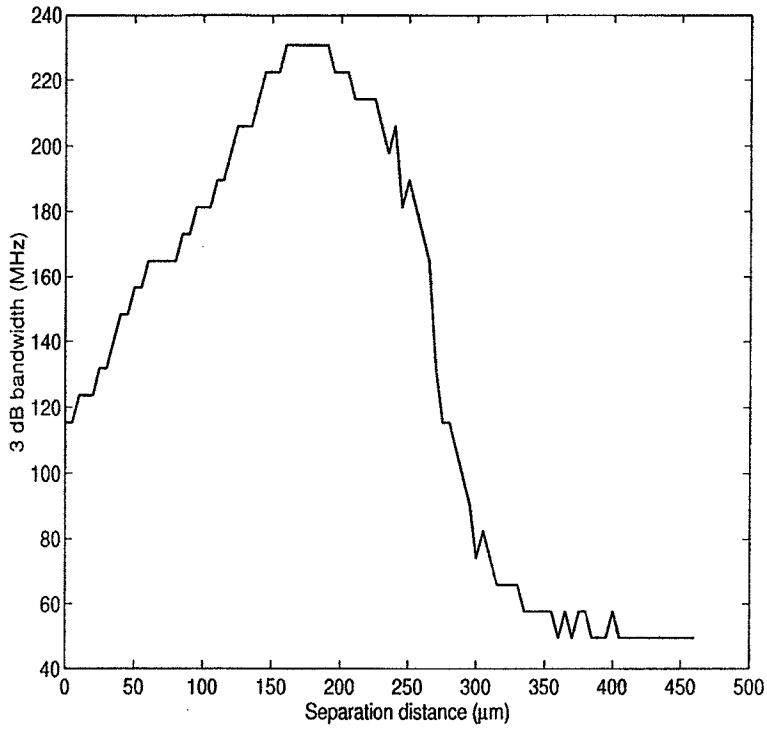

Figure 4.10: 3 dB bandwidth calculations as a function of the separation distance

separation distance. It is clear from this figure that the principle described in the previous section of dimensioning slow modes with increasing separation distance is also applied here with a single mode laser. Calculations of the corresponding 3 dB bandwidth from the temporal responses are shown in Figure 4.10, which clearly demonstrates that increasing the separation distance increases the bandwidth to some optimum distance when both bandwidth and power are a concern. Figure 4.11 shows the eye diagram for the system with an input of a pseudorandom bit sequence of $10^{15} - 1$ at a data rate of 625 Mbps before modifying the launch, and Figure 4.12 after modifying the launch to the optimum separation distance, which clearly demonstrates the improvement in the eye diagram. These two eye diagrams correspond to a bit error rate of 0.2 before and 4E-9 after modifying the launch. These measurement of the bit error rate were carried out using the experimental setup shown in Figure 4.13, where the single mode laser was driven directly by a

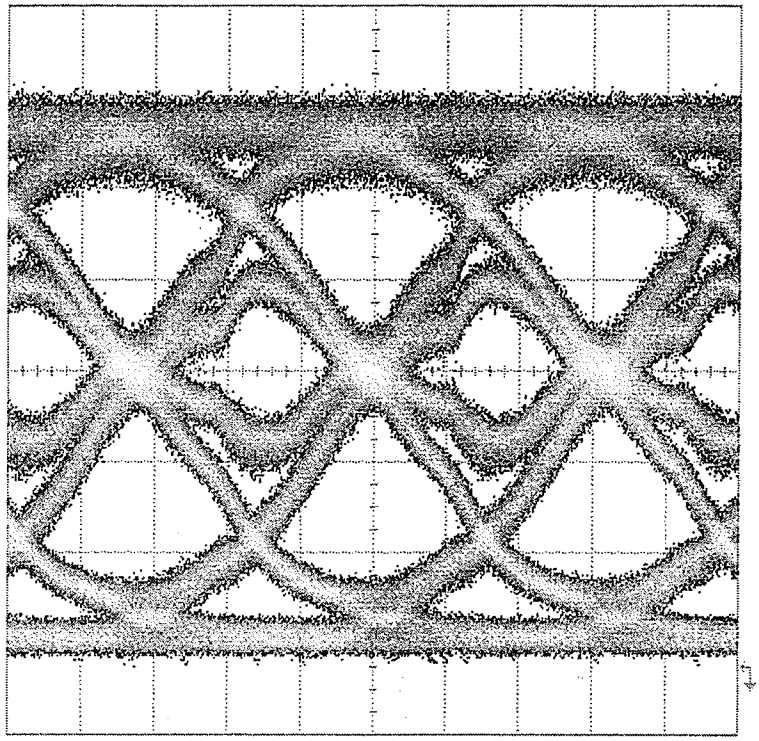

Figure 4.11: Eye diagram at zero separation.

BERT acting as a 50 Ω source with a 13 dB optical extinction ratio (ER). The laser output was launched into the 1km MMF; the output of the MMF was then collected by a preamplified PIN photodiode from Honeywell part number HFD3381-102 which has a specified bandwidth of 2.4 GHz. The photodiode's output was returned to the BERT to carry out the error measurement. In order to produce the bit error rate curves for different received powers, an optical attenuator, Agilent 8156A with option 350 module specified for multiomde fibers, was used between the fiber and the photodiode to change the received power, and the bit error rate was measured at each power level. Figure 4.14 shows the bit error rate curves with a data rate of 625 Mbps before and after modifying the launch.

4.4 VCSEL Beam Divergence Dependence on Data Pattern

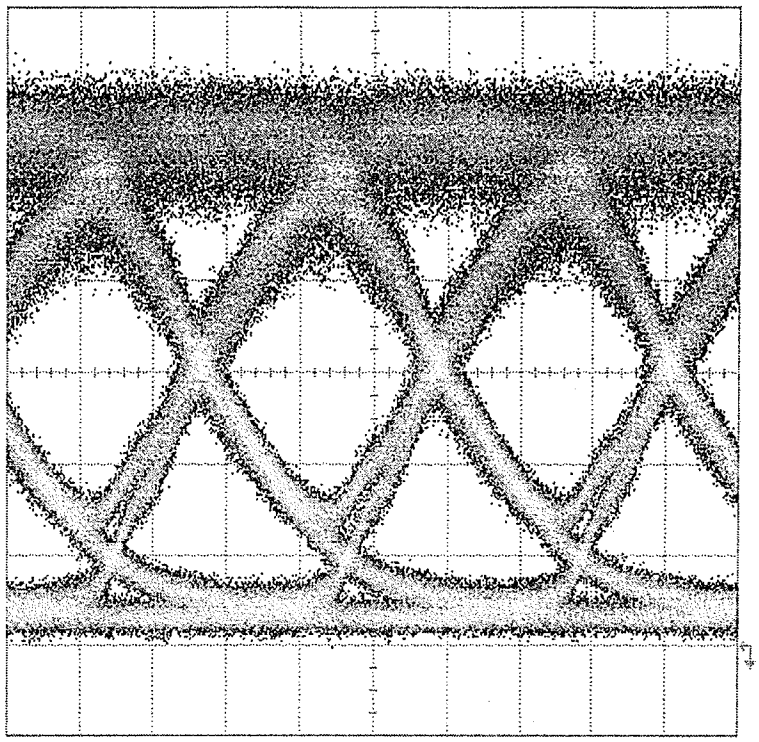

Figure 4.12: Eye diagram at 150 μm separation.

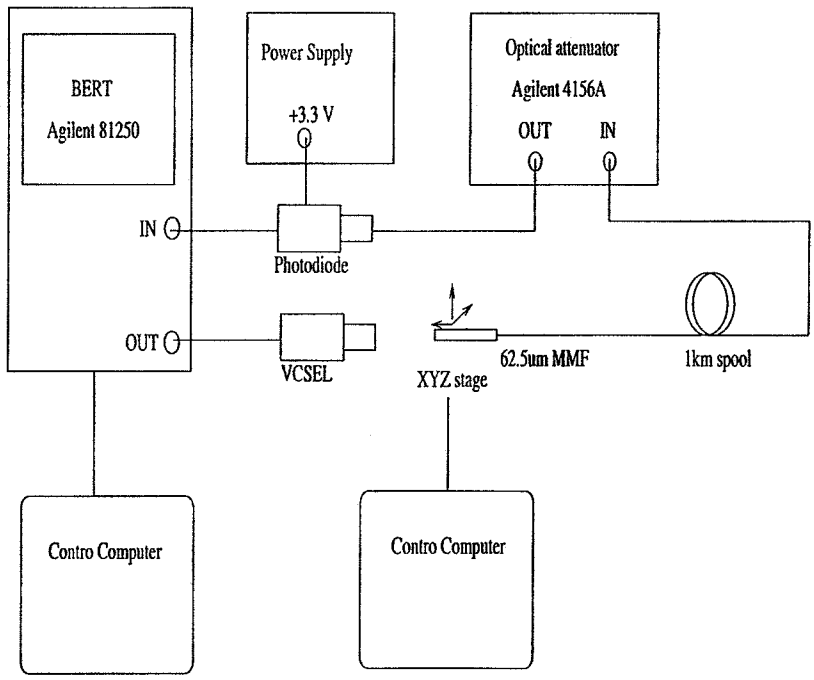

Figure 4.13: Experimental setup for measuring the BER.

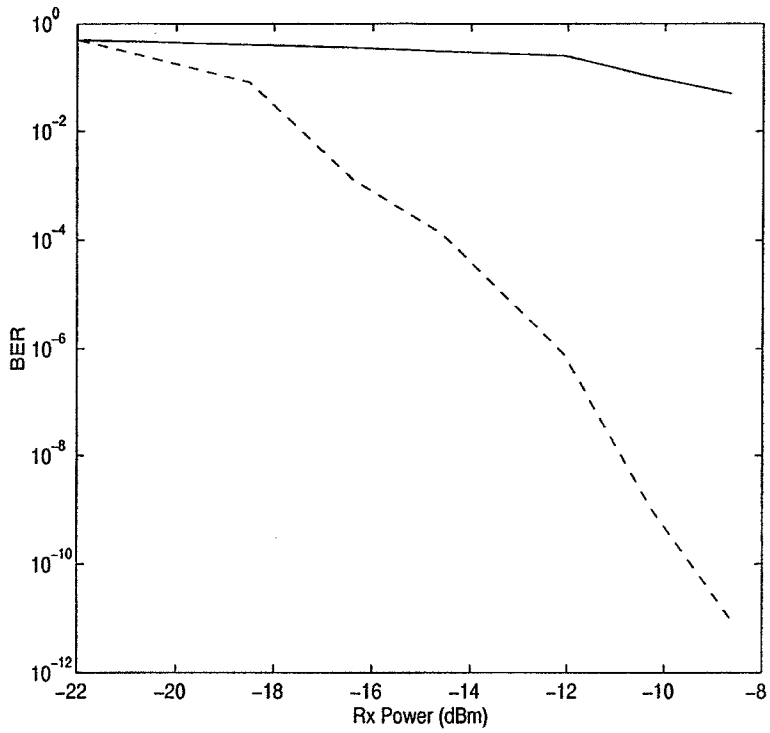

Figure 4.14: BER for a data rate of 625 Mbps with zero separation (solid), and 150 μm separation (dashed) .

4.4.1 Experiment

In the experimental setup of Figure 4.15, commercial VCSELs purchased from two major VCSEL manufacturers were used as the optical sources. Parts from both manufacturers, referred to as Part A and Part B, are oxide-confined, 2.5Gbps, 850nm VCSELs in transmitter optical subassembly (TOSA) packages with approximately 1:1 imaging lenses. Multiple samples of each part were tested with consistent results. These VCSELs are directly driven by a Bit Error Ratio Tester (BERT) (Agilent 81250) acting as a 50 Ω source at a rate of 1.25Gbps. The high and low drive levels were set to achieve an extinction ratio of approximately 13dB and an average total power of -4dBm. With this apparatus, the output beam divergence angle distribution was measured by rotating a multimode fiber tip around the focal spot of the VCSEL TOSA under test. The fiber is was connected to a photodiode to measure the received power. The distance between the fiber tip and

the TOSA focal spot was approximately 5mm so that the 62.5 μm core diameter of the fiber subtends an angle of 0.7 degrees. The rotation stage is motorized and is controlled by a computer that also obtains the photocurrent as the fiber tip is stepped through the beam angles. A rotation stage was used instead of a translation stage to maintain constant light acceptance of the fiber independent of position. The beam divergence angles from the TOSA focal spot are assumed to be comparable to those from the VCSEL itself due to the 1:1 imaging ratio of the lens in the TOSA. The VCSELs were driven by two different square wave data patterns, one with a 2-bit period and one with a 32-bit period corresponding to fundamental frequencies of 625MHz and 39.1MHz, respectively. Both patterns had a 50% duty cycle so that the average power dissipation and thus thermal biasing were the same. The maximum run length of 16 ones or zeroes for the low-frequency pattern exceeds the run length for Gigabit Ethernet's 8B/10B block coding, but higher data rate standards, e.g. 10 Gigabit Ethernet, might use coding with run lengths of up to 64 [33]. As discussed below, overshoot was observed for some portions of the far field using the 50% duty cycle patterns. Additional patterns, including gain-switched pulses and altered drive levels, were used to investigate the overshoot phenomena. Gain-switching was achieved using the BERT by driving the VCSEL with a one followed by a pattern of 15 zeros, and the VCSEL lower bias was set below threshold.

4.4.2 Experiential Results

The measured far field distribution of Part A is shown in Figure 4.16, where the solid line is for the high frequency pattern, the dashed line is for the low frequency pattern, and the dotted line is for gain switched pulses. The far field scan was repeated four times and found to be reproducible, with Figure 4.16 being the average of the four. It is clear that the high frequency pattern results in more

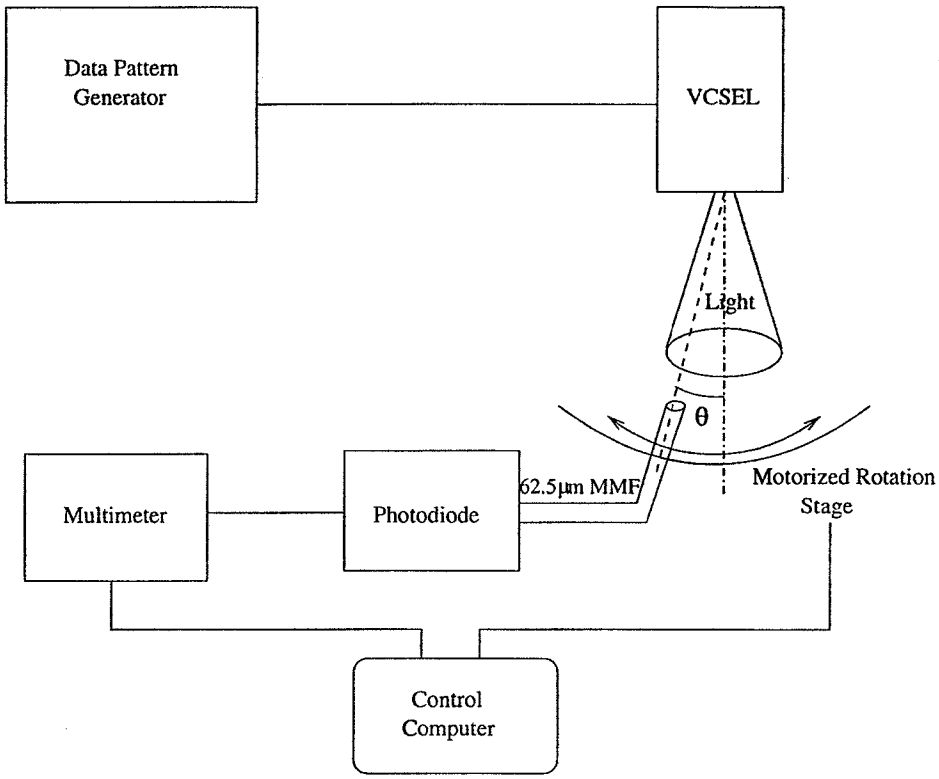

Figure 4.15: Experimental setup for measuring VCSEL's beam divergence.

on-axis output power and slightly reduced off-axis output power in comparison to the low frequency pattern. The gain-switched far field pattern is even more concentrated near the axis. From this figure it is clear that gain-switching the VCSEL reduces the excitation of high order fiber modes in comparison to pulses formed with regular bias levels.

The situation is similar for Part B shown in Figure 4.17, where the on-axis power is slightly higher for the high frequency patterns but the difference is not as great as for Part A, and both high and low frequency patterns have the notable side lobes at +/-7.5 degrees. Since the far field power distribution changes with the data pattern for both parts, it is expected that the effective fiber bandwidth or corresponding pulse spreading would also be pattern-dependent. Patterns with different duty cycles could be expected to change the power dissipation and thus

the strength of the thermal lens, which in turn would impact the beam divergence slightly for oxide-confined VCSELs and to a greater extent in implant-confined VCSELs[34]. But the effects observed here with the same duty cycles must be related to carrier dynamics on a time scale much shorter than the thermal time constant.

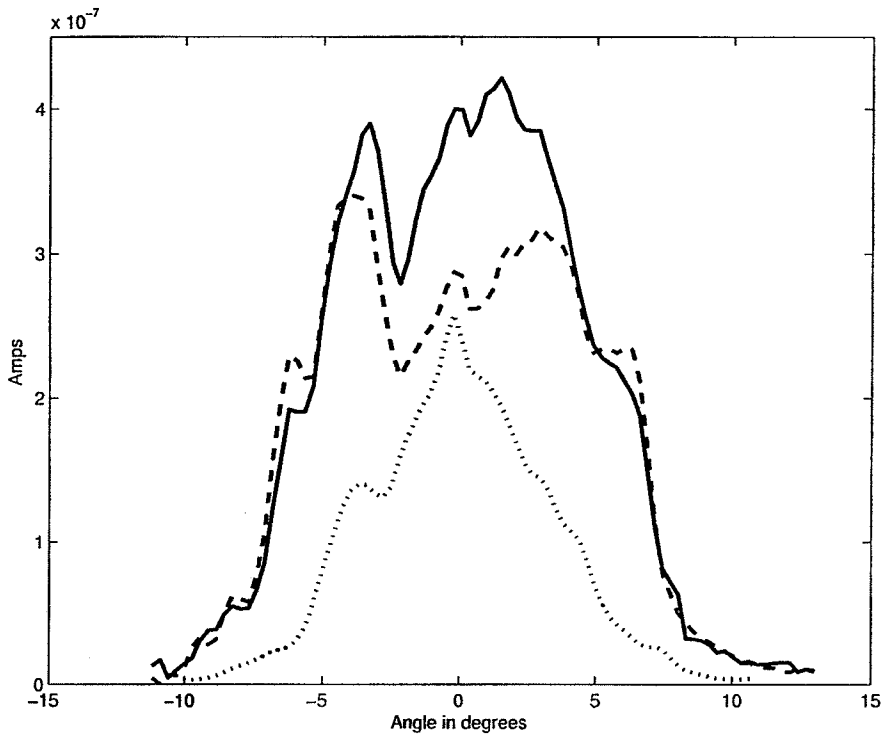

Figure 4.16: Beam divergence angle distribution for Part A: alternating ones and zeros pattern (solid), alternating sixteen ones and sixteen zeros (dashed), and gain switched pulse one followed by fifteen zeros (dotted). Dotted data is multiplied by 7 to ease comparison.

To better understand the origin of the change in beam distribution with data pattern, the temporal waveform of the laser output was observed as a function of far field angle using a data pattern with both high and low frequency content. This measurement was carried out by coupling the fiber patch cord to a HP model 86100A digital oscilloscope with an FC optical channel plugin model 86101A. The

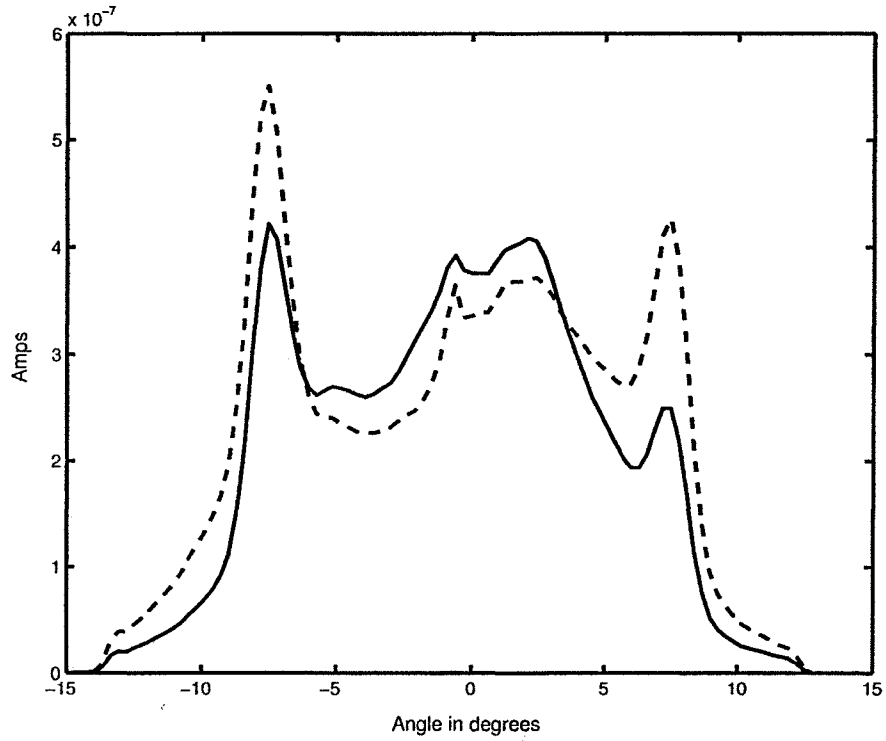

Figure 4.17: Beam divergence angle distribution for Part B: alternating ones and zeros pattern (solid), alternating sixteen ones and sixteen zeros (dashed).

bandwidth of the optical channel was specified to be at least 3GHz. Figure 4.18 shows the measured pulse shapes for Part A at launch angles of (a) zero degrees, (b) -3 degrees, and (c) -6 degrees.

These waveforms show significant overshoot on-axis and undershoot off-axis at the zero to one transition. Part B (see Figure 4.19) also exhibits off-axis undershoot together with on-axis overshoot. For both parts, overshoot is maximized at 0 degrees, and the overshoot contributes noticeably to the average on-axis power from the VCSEL. Figure 4.19 part (c) shows the waveform of Part B at -7.5 degrees, which corresponds to the enhanced left-side lobe where the power is high but the rise time is slow with clear undershoot, which clearly demonstrates that this phenomenon is angle- dependent. The presence of more transitions in the high frequency pattern results in it generating more power on-axis than the low frequency

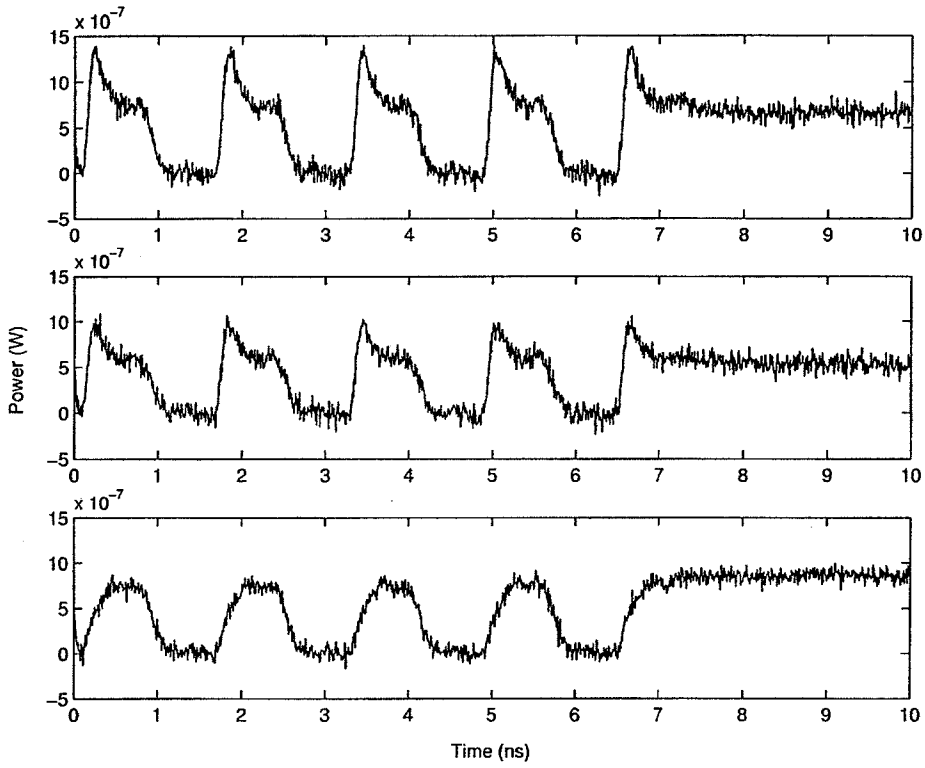

Figure 4.18: Bit time pulses of Part A: (a) at 0 degrees, (b) at -3 degrees, and (c) at -6 degrees.

pattern. But in the case of Part B the overshoot is less than that of Part A, thus reducing the contribution to differences in on-axis average power. When the fiber is placed into the TOSA to couple all the light within the numerical aperture of the fiber, both Parts A and B create waveforms, as shown in Figure 4.20, with significantly less overshoot or undershoot than seen in the angle-resolved waveforms of Figure 4.18 and 4.19. Thus, the on-axis overshoot and off-axis undershoot in large part balance when the integrated power is considered. Figure 4.21 shows the angle-resolved pulses for Part A for regular pulses (solid), and gain-switched pulses (dotted) at 0 and 6 degrees. As expected from the time-averaged far-field scans presented in Figure 4.16, the temporally resolved gain-switched pulse has a greater percentage of its power on-axis than the 50% duty cycle balanced pulses.

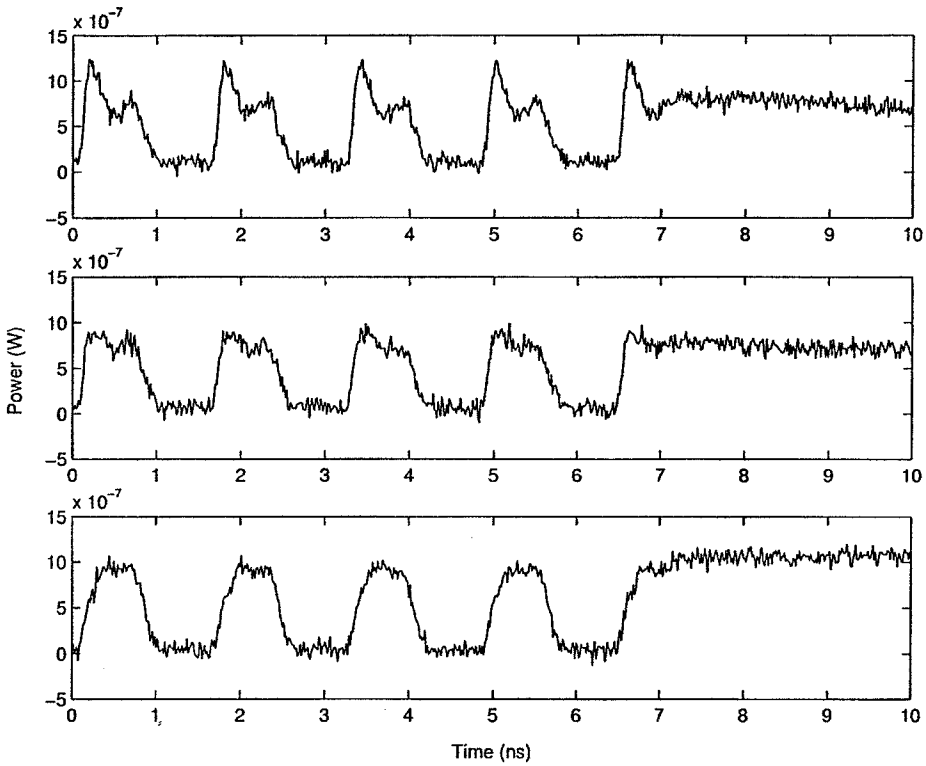

Figure 4.19: Bit time pulses of Part B: (a) at 0 degrees, (b) at -3 degrees, and (c) at -7.5 degrees.

In fact, the comparison in Figure 4.21 shows that the gain-switched pulse is more concentrated on axis than even a single pulse created with the regular bias level.

4.4.3 Discussion of Results

Prior investigations of polarization-resolved waveforms led the authors of Ref. [35] to conclude that a low-to-high drive transition on a implant-confined VCSEL caused the high-order mode to overshoot and the low-order mode to undershoot. With the assumption that the fundamental mode contributes more on-axis power and higher order modes contribute more power in the wings of the beam distribution, it appears that the oxide-confined devices in this study behave opposite to those in [35]. Here the fundamental mode appears to overshoot and the high order mode undershoots. The difference in the angle and polarization-resolved studies

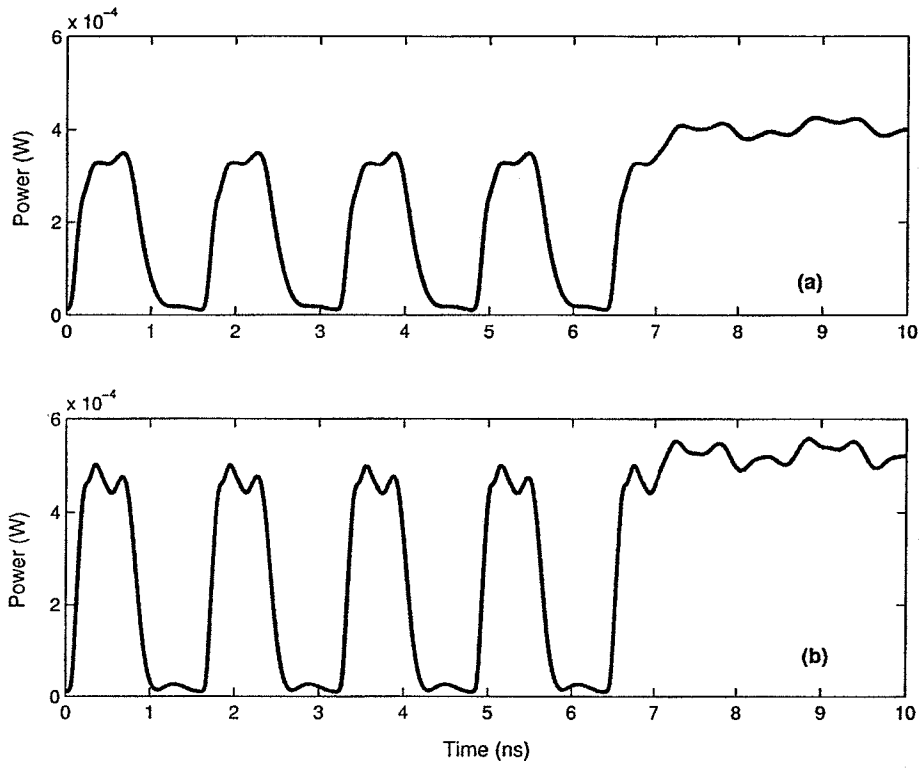

Figure 4.20: Total integrated bit time pulses of: (a) Part A, and (b) Part B.

may be due to the different behaviors of implant and oxide-confined VCSELs. The strong coupling of the high-frequency edge transition to the fundamental mode in this study is not consistent with a peripheral current-crowding effect, as seen bipolar transistor emitters, and the duration of the overshoot is inconsistent with thermal timescales.

Another possible cause for the observed overshoot that was considered was spatial hole burning decreasing the central carrier density and thus fundamental mode power as the photon density builds after the zero-to-one transition. To investigate this explanation, the high (one) drive level for Part A was reduced with the expectation that this would reduce spatial hole burning effects. Figure 4.22 shows the on-axis temporal waveforms for both regular pulses (solid) and reduced high-level drive current pulses (dotted). However, both waveforms exhibit

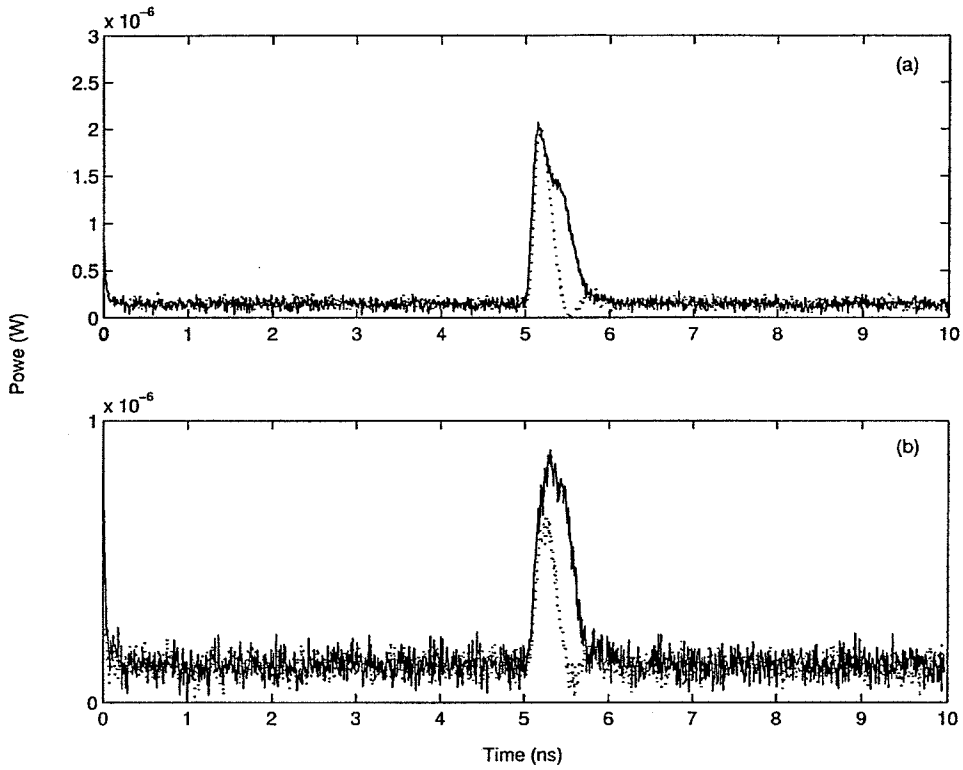

Figure 4.21: Bit time pulses of Part A: regular pulse (solid), and gain switched pulse (dotted): (a) At 0 degrees, and (b) At -6 degrees.

comparable overshoot, implying that spatial hole burning may not be responsible for the overshoot. Additional experiments showed that increasing the bias level strongly reduced the overshoot, as seen in Figure 4.23, indicating that some modes may be modulated below threshold with the original bias level used to obtain a 13dB extinction ratio.

4.4.4 Summary

The angle-resolved waveforms with undershoot or overshoot can be considered a non-linear response to the fairly rectangular current pulses, since deviations only occur on the leading and not on the trailing edge. The non-linearity is far smaller when considering the integrated power, as seen in Figure 4.20. However, to the extent that the fiber bandwidth or corresponding impulse response shown varies

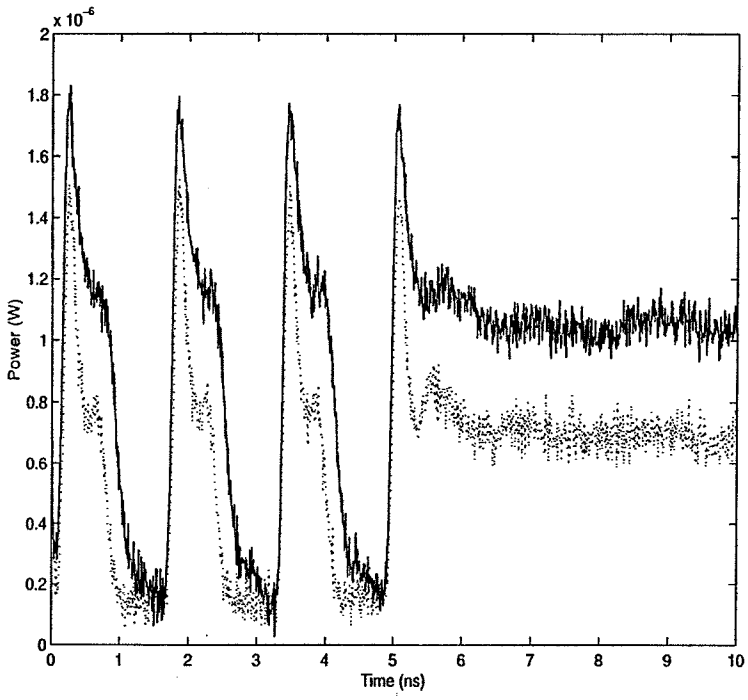

Figure 4.22: Bit time pulses of regular pulses (solid), and reduced drive current pulses (dotted).

with launch angle, as shown in Figure 4.1, the overall source and fiber system may again behave non-linearly even if the integrated power at the source does not overshoot. This situation is aggravated by the strong on-axis overshoot coupling to the unstable bandwidth region at the center of the fiber. Any non-linearity would complicate processes such as equalization of MMF links to obtain greater bandwidth-distance products.

4.5 System Bandwidth Dependence on Data Pattern

All researchers who have carried out fiber optic system equalization in the electric domain have assumed that the fiber channel is static or slowly varying with time. As such, they either carry out the equalization linearly, or non-linearly without taking into any account the data pattern dependency phenomenon. As

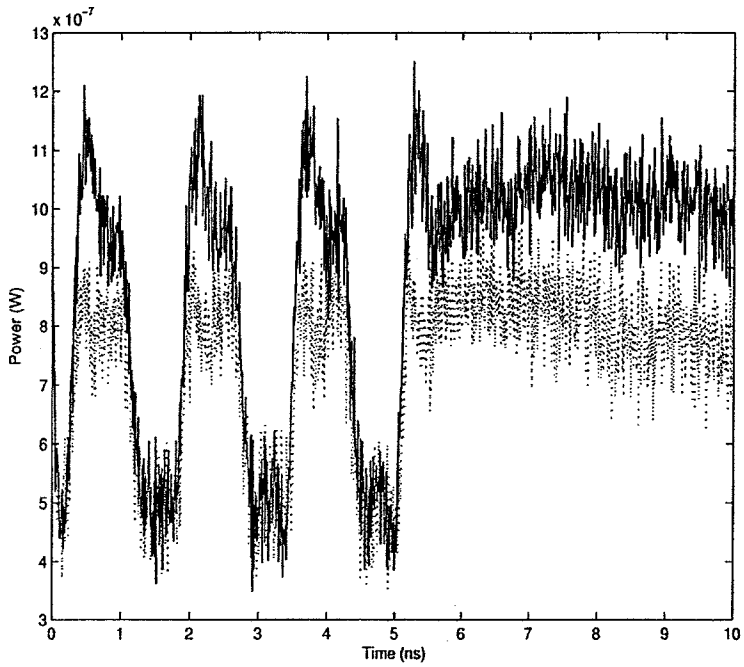

Figure 4.23: Increased bias level bit time pulses of regular pulses (solid), and reduced drive current pulses (dotted).

mentioned before, we determined that the source beam divergence distribution depends on the data pattern driving it (see Figure 4.24), and, as mentioned in the previous chapter, beam profile affects the impulse response of the fiber. This idea is itself our original, previously unpublished work. It is presumed that taking this into account in non-linear electrical equalization will improve the performance.

Unlike the traditional copper wire communications systems optical communication systems use light as a mean of communication by using lasers. Lasers would introduce some non-linearity to the whole system, as a simple example light can not go negative it is always positive.

If we consider the plot of the angle-resolved temporal pulses of the VCSEL, it is clear that these profiles shown in Figure 4.25 result from a non-linear device.If we were to equalize this signal in the continuous time-domain sense, considering

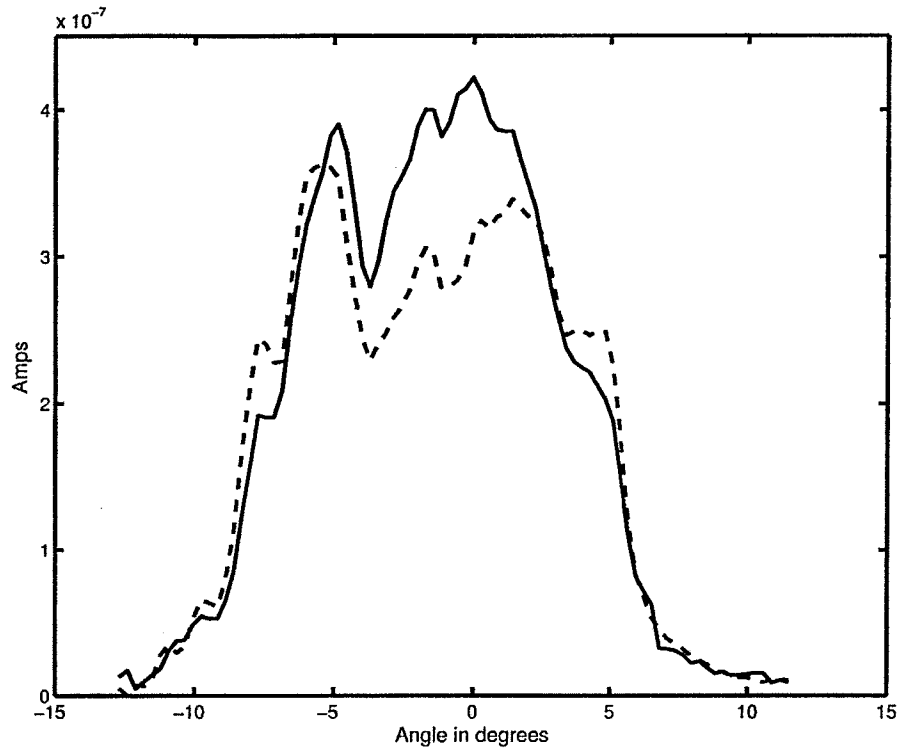

Figure 4.24: Beam divergence angle distribution for Part A: alternating ones and zeros pattern (solid), alternating sixteen ones and sixteen zeros (dashed).

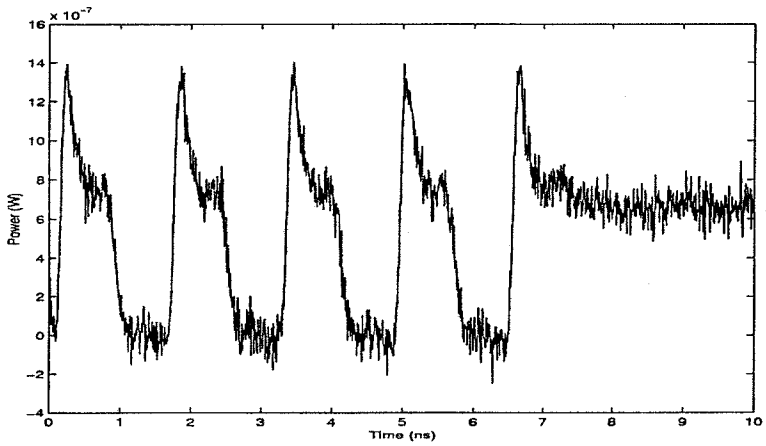

Figure 4.25: Bit time pulses of VCSEL at 0 degrees

$x(t)$ the required signal, which is of rectangular shape, then the output $y(t)$ would be

$$y(t) = h_1(t) * x(t) + h_2(t) * |\frac{dx(t)}{dt}|, \tag{4.5-3}$$

where * denotes convolution, $h_1(t)$ represents the small amount of normal spreading, and $h_2(t)$ is the shape of the overshoot. This is with no fiber, and if we need to include the fiber we need to convolve the whole thing with the impulse of the fiber, which would be data pattern-dependent. This is clearly a non-linear process due to the absolute value of the derivative of $x(t)$.

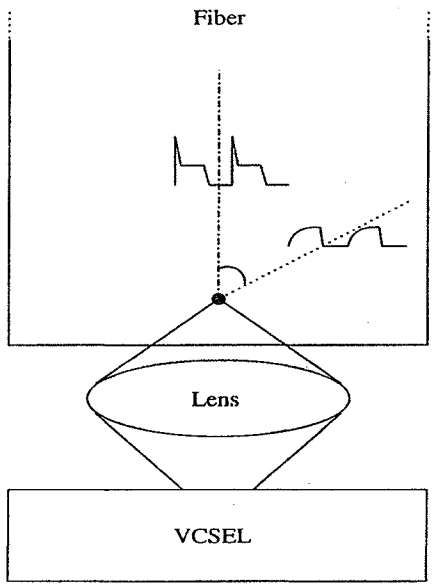

Figure 4.26: Power distribution over Beam divergence.

This constitutes one portion at some angle of the transmitted power. However, to find the total integrated power, we need to integrate over all possible angles, which would still exhibit some non-linearity according to equation 4.5-3.

$$P_{total}(t) = 2\pi \int_{\theta} p(\theta;t)h(\theta;t)d\theta \tag{4.5-4}$$

where $p(\theta;t)$ is the radiant intensity, that is power per solid angle, and $h(\theta;t)$ is the fiber impulse response as a function of launch angle. The description and effect of this non-linearity on link performance and its non-linear mitigation will be presented in the next chapter.

Chapter 5

PATTERN DEPENDENCY EFFECTS ON LINK AND NONLINEAR EQUALIZATION

5.1 Introduction

As mentioned in the previous chapter, it has been found experimentally that the far field beam divergence distribution of a multimode VCSEL depends on the data pattern driving the VCSEL. The implications of this dependency were discussed in the preceding chapter, including the fact that the effective multimode fiber bandwidth depends on the launch angle, and since the beam divergence angle distribution is data-pattern dependent, this would imply by chain rule that the effective multimode fiber bandwidth is likewise data-pattern dependent. In this chapter, various attempts, both experimental and modeling, to quantify the effect of this non-linearity on link performance are presented. These attempts include first studying the offset and angle launching conditions separately to parameterize the MMF modes by illumination of the whole fiber face by means of a collimated beam with different angles, then using a visible single-mode fiber to launch light in MMF fiber at different offsets.

This method, discussed in Section 5.2, presents some problems associated with the excitation of modes. Section 5.3 details a second attempt to excite selected modes using spatial filtering to filter the beam out of the source in order to control the light entering the MMF fiber by the use of a moving pinhole along the fiber

axis. This method, however, also presents some problems with diffraction due to small aperture size. A third attempt employed was the use of a mask set with holes very close to the MMF fiber face as a beam filtering method; it is presented in Section 5.4. This method yielded some reasonable results, which also agrees with the model built as the fourth attempt. The problem with this experiment is that the hole sizes are not sufficiently small.. The main idea of quantifying this effect on link impulse response, and hence bandwidth, is to linearly combine the different impulse responses taken at different launch angles and weighted by the beam divergence distributions for a certain data pattern.

After quantifying this effect a solution is presented in Section 5.7 to achieve an equalization that takes into account the non-linearity of the change in system impulse response with data pattern. A description of the algorithm and some results of the improved performance is reported here.

5.2 Angle/Offset Launch Experiments

5.2.1 Method

The main idea of quantifying the effect of the data pattern dependency is to apply the following superposition criteria: An impulse of light is launched into the multimode fiber at different angles simultaneously; the impulse response is then observed at the end of the fiber. Consequently, there would be different impulse responses for different launch angles. The far- field scans, i.e., the beam divergence angle distributions, are nothing but the distribution of the average power of the source over angles for a certain data pattern. In order to obtain the impulse response for a certain data pattern, we take the different impulse responses for different launch angles and combine them according to the source's average power distribution over angle (the beam divergence distribution) for this particular data pattern. For example, Figure 5.1 shows the normalized beam

divergence distribution of a VCSEL for alternating ones and zeros at a data rate of 1.25Gbps, as discussed in section 4.4.

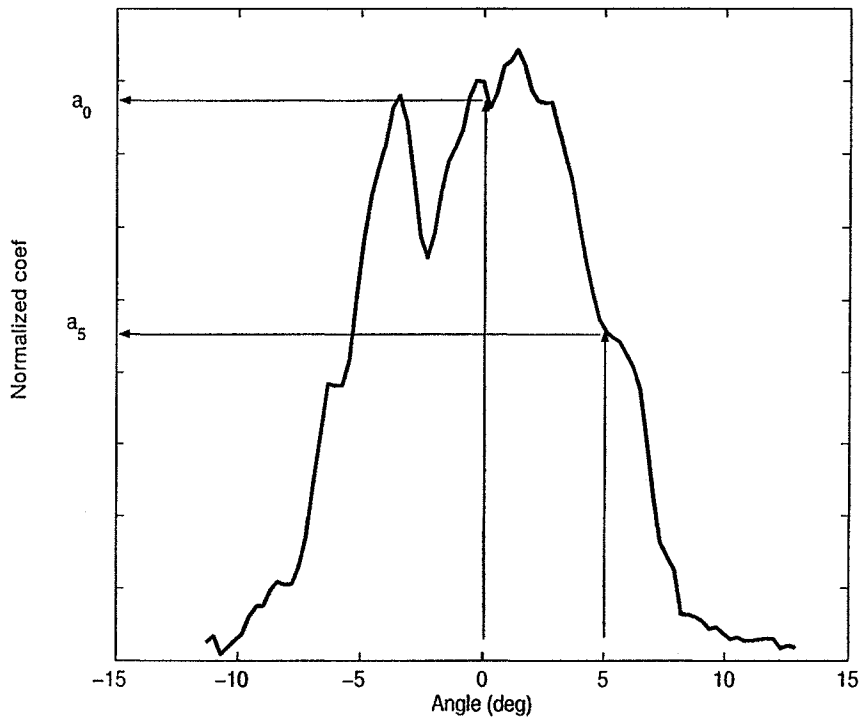

Figure 5.1: Beam divergence distribution of alternating ones and zeros with weight coefficients displayed.

Assume that imp_0 is the impulse response at a launch angle of zero, imp_1 is for launch angle of 1 degree, and so on. Then the effective impulse response for this data pattern is

$$Imp_{0101..} = a_0 imp_0 + a_1 imp_1 + ... \tag{5.2-1}$$

where the coefficients of a_0, a_1 are from the beam divergence distribution of the alternating ones and zeros pattern shown in Figure 5.1. Every term in equation 5.2-1 to predict the impulse response of the alternating ones and zeros are then weighted by the relative area of each incremental angle changing as the angle

grows. In order to determine the impulse response of a mode that corresponds to a certain launch angle or offset, we need to understand and describe the modes of the fiber which are believed to depend on the offset and angle of launch. The original plan was to characterize the modes of the fiber by offset and angle with two different experiments: one by fixing offset and changing the launch angle, which will be described in the following subsection, and the other by fixing the angle and changing the launch offset, which will be described in subsection 5.2.3. Subsequently it becomes possible to solve the problem as a system of linear equations where the unknowns are the impulse responses at different offset and angle of launch. Finally, we can describe our source-to-fiber orientation by selecting the correct combination of impulse responses of excited modes, after which we can weight and combine by the beam divergence distribution of a certain data pattern to find the effective impulse response for that particular data pattern.

5.2.2 Angle Experiment

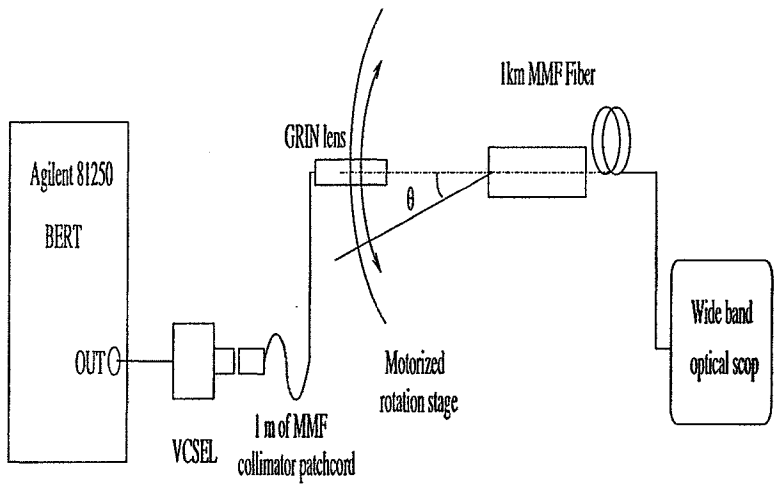

Figure 5.2: Collimated beam launch angle experimental setup.

The impulse response of the MMF is investigated as a function of the launch angle of a collimated beam that illuminates the whole MMF fiber face by the use of

a MMF fiber patch cord with a graded index (GRIN) lens mounted at the end with a beam diameter of 300 μm (purchased from OZ Optics part number LCP-01-850-125/50-3-8-1). This is achieved by using the experimental set- up of Figure 5.2. Isolated, $\sim$ 750 ps duration, electrical pulses at a repetition rate of 41.7 MHz from an Agilent 81250 data generator were used to gain-switch VCSELs producing $\sim$ 200 ps optical pulses in the GRIN-lensed MMF patch cord. The commercial, 850nm VCSELs in transmitter optical sub-assembly (TOSA) packages were multimode, oxide-confined structures specified for 2.5 Gb/s operation. The GRIN lens was mounted on a motorized micropostioning rotation stage with one end of a 1 km long, 62.5/125 μm graded-index MMF mounted at the center of the rotation stage. A pulse was launched into the 1km MMF at different angles. The output of the MMF was connected directly to an Agilent model 86100A digital oscilloscope with an FC optical channel plug-in (model 86101A) to measure the temporal shape of the output pulse. The bandwidth of the optical channel was specified to be at least 3GHz. Output pulse forms were measured as a function of the launch angle between the GRIN lens and MMF using automated computer control of the rotation stage. The range of angles studied was 0 to 13 degrees, at which the signal became very weak.

The trends in the temporal power distribution as a function of collimated beam launch angle are clarified in Figure 5.3 as a contour plot with coordinates of time and launch angle. As the launch angle increases, the impulse response starts to narrow down, causing the slow modes to disappear. This is clarified further when re-presenting the results of the 0 and 13 degree launch impulse responses, shown in Figure 5.4, in which the solid line shows the 0 degree launch and the dashed line shows the 13 degrees launch. It is clear that the width of the impulse response and hence the bandwidth depends on the launch angle. By using this set-up of a collimated beam, the whole offset range was excited at each angle. Consequently,

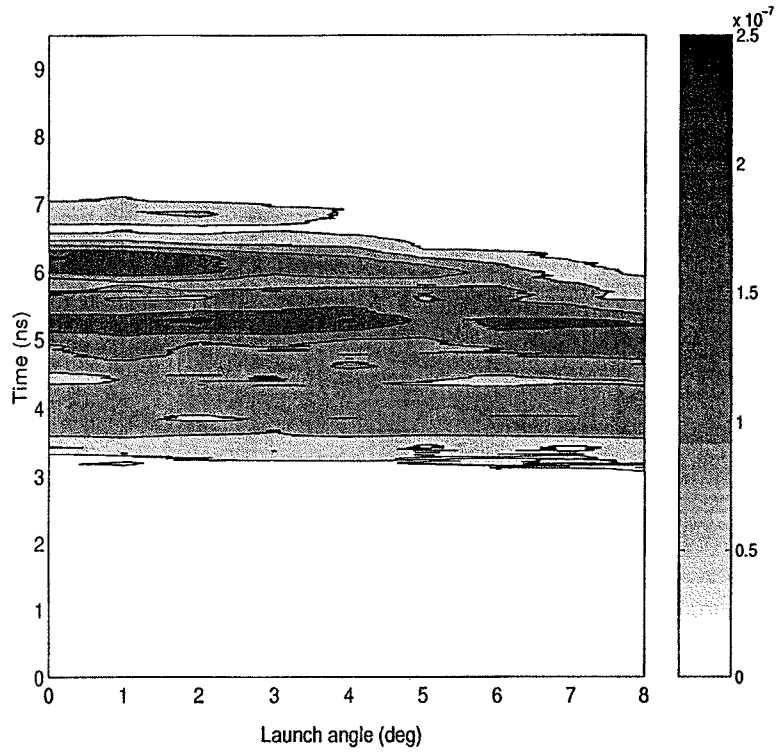

Figure 5.3: Temporal response contour plot as a function of the launch angle.

one part of the experiment was described. The other part, involving fixing the angle and changing the offset, will be described in the following subsection.

5.2.3 Offset Experiment

The impulse response of the 1km MMF was investigated as a function of the launch position of a SMF, using the experimental set-up of Figure 5.5. The pulses were produced in the same manner as discussed in the angle experiment (subsection 5.2.2), using the same VCSEL. Although the VCSEL emitted multiple transverse modes, the 4 μm core diameter SMF resulted in a well-controlled single transverse mode being launched into the 1km long, 62.5/125 μm graded-index MMF, which was the only fiber spool used throughout the research described in this dissertation. The separation between the connectorized ends of the SMF and the MMF

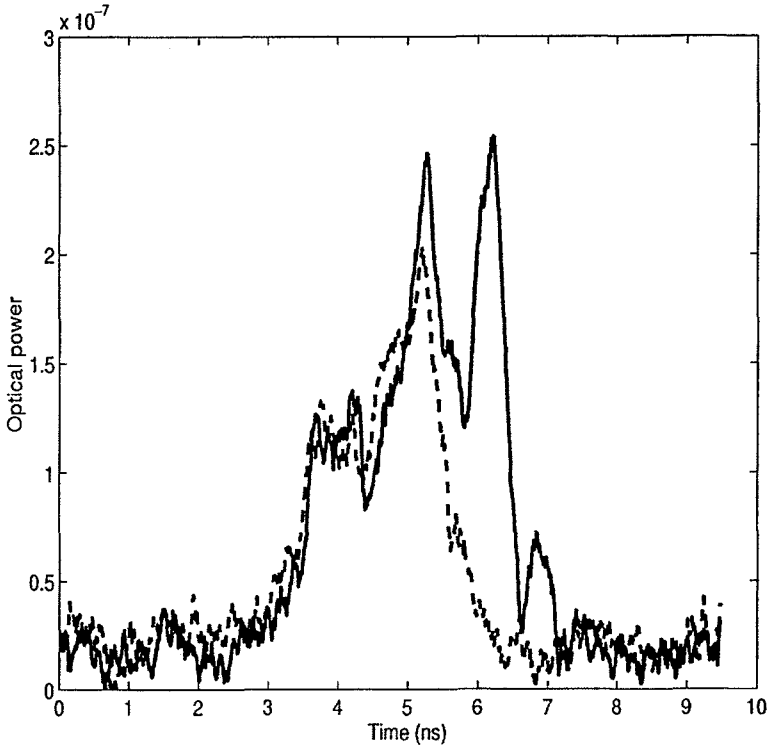

Figure 5.4: Temporal response at: zero degree (solid), and 13 degrees (dashed).

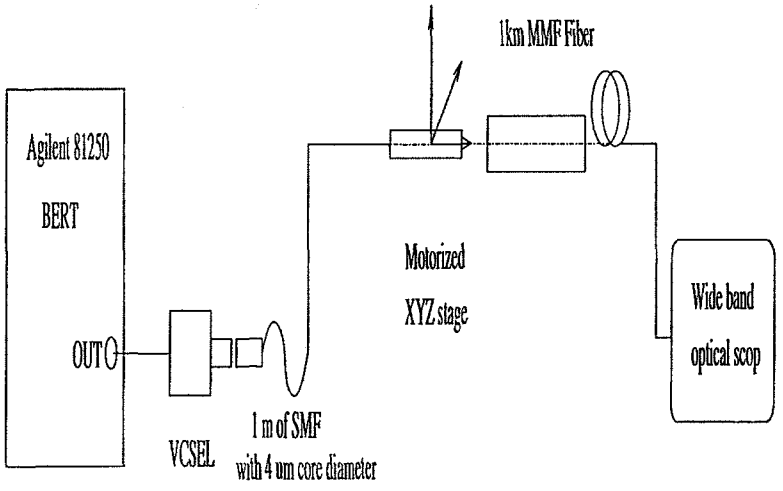

Figure 5.5: Offset launch experimental setup.

was controlled using a motorized micropostioning translation stage. An initial concentric alignment of the SMF and MMF connector ferrules was established using a coupling sleeve. The SMF was moved to scan the offset, that is, to emit the pulses at different radial positions of the MMF face. The output of the MMF fiber was connected directly to the Agilent model 86100A digital oscilloscope mentioned in subsection 5.2.2

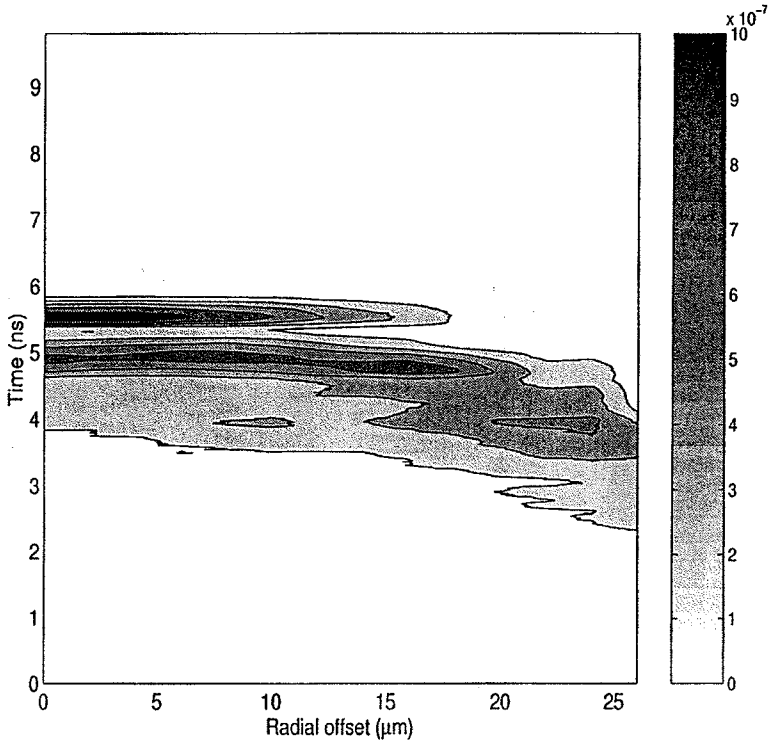

Figure 5.6: Temporal response contour plot as a function SMF launch radial position.

The trends in the temporal power distribution as a function of the SMF radial launch position are clarified in Figure 5.6 as a contour plot with coordinates of time and radial launch position. As the launch goes away from the center, the fast modes of this fiber, i.e. the higher order modes, start to dominate the impulse response.

After carefully considering the two parts of the experiment and further studying the shape of the beams of both the collimator and the 4 μm single mode fiber,

which has a numerical aperture of 0.12, and after understanding the distribution of the modes in multimode fiber with respect to launch configuration[36], it was understood that beams will excite helical modes in addition to meridional modes in both parts of the experiment. The helical modes add the third dimension in addition to offset and angle which are discussed in Chapter 3. This makes the interpretation of results shown in Figures 5.3 and 5.6 impossible, rendering it an underdetermined system that cannot be solved for a unique solution-i.e., the number of unknowns, which are the modes' impulse responses, is greater than the number of equations. Since we assumed center launch when describing the problem of bandwidth data pattern dependency, meaning that no helical modes are involved, it would be better if we could carry out an experiment without exciting the helical modes. An attempt at such an experiment is presented in the next section.

5.3 Pinhole Launch Experiment

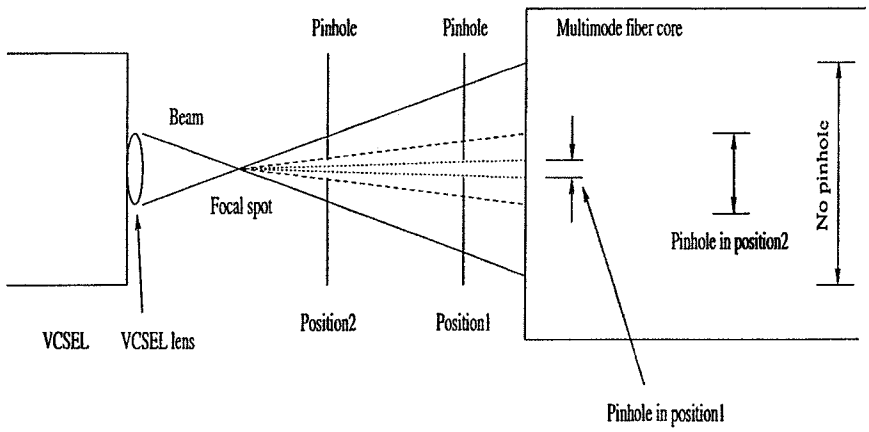

Figure 5.7: Spatial filtering idea using a pinhole.

An attempt to maintain a center launch configuration and not include helical mode spatial filtering was made. In this experiment, a pinhole was used as a

spatial filter to filter the beam out of a laser and select a portion of the beam to be coupled to the multimode fiber with fixed angle at all offset (see Figure 5.7), where in position 1 only a selection of the lowest order modes are excited and in position 2 more higher order modes are excited, with all modes being axial or meridional, without any helical modes being involved because of the center launch configuration. It was then possible to carry out a precise measurement by moving the pinhole with very small step size.

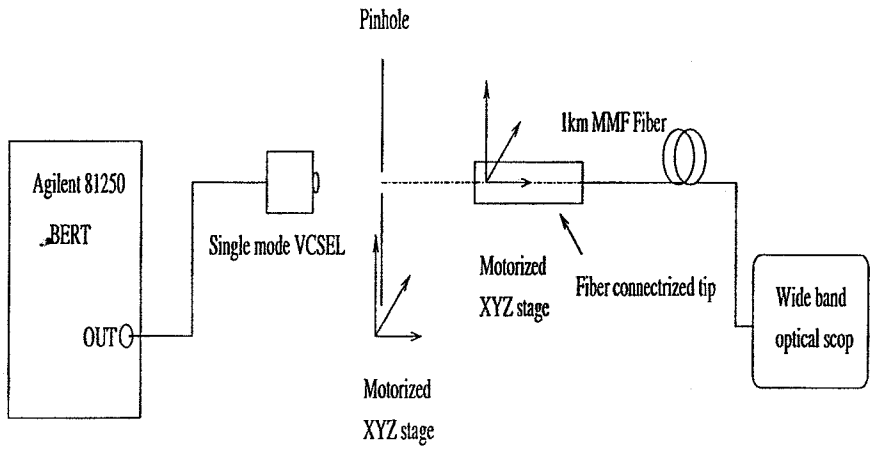

Figure 5.8: Pinhole experimental setup.

The experimental setup is shown in Figure 5.8 It was planned to investigate the impulse response of the 1km MMF as a function of the pinhole position. Pulses were generated from the Agilent 81250 data generator, as mentioned in subsection 5.2.2, and were used to gain-switch VCSEL producing $\sim$ 200 ps optical pulses. The commercial, 850nm VCSELs in modified transmitter optical subassembly (TOSA) packages were single mode, ion implant-confined structures. The VCSEL emitted a single transverse mode with a high power, specified to be 1mW in focus, which was 1.5 mm from the surface of the spherical lens of the TOSA. The barrel of the TOSA was cut to obtain a full beam from the VCSEL. A single mode VCSEL was used in this experiment without a single mode fiber for conditioning the launch in

order to obtain higher coupled powers to the MMF. The same 1km-long, 62.5/125 μm graded-index MMF used in the earlier experiments was manipulated using an XYZ micropositioning stage to couple the VCSEL's focal spot into the fiber axis by maximizing the power coupled into the fiber measured by a low frequency optical power meter. After the fiber was positioned at the focal spot, it was pulled back a distance of 50 μm and the pinhole was inserted between the VCSEL and the fiber. The pinhole was also mounted on an XYZ micropositioning translation stage and was manipulated to position the hole in the VCSEL focal spot by maximizing the power. In order to obtain a good result and a good range of shadow sizes that excite fiber modes from the pinhole, a very small pinhole diameter is needed. Consequently, we used a 5 μm diameter pinhole. The output of the MMF fiber was connected directly to the Agilent model 86100A digital oscilloscope mentioned in subsection 5.2.2.

Until we studied the experimental configuration and included what would happen with diffraction due to the pinhole, the output of the pinhole was believed to give a circ function. Fresnel diffraction computation gives the shape of the beam emitted from any aperture shape or size as a function of the distance from the aperture based on the assumption that the incident wave is multiplied by the aperture function $p(x, y)$, which in our case is a circle, and propagates according to the Fresnel approximation. The diffraction pattern $I(x, y)$ can be written as follows:[37],[38]

$$I(x,y) = \frac{I_i}{(\lambda d)^2}\left|\int\int_{-\infty}^{\infty} p(x^{'},y^{'})\exp[-j\pi\frac{(x-x^{'})+(y-y^{'})}{\lambda d}dx^{'}dy^{'}\right|^2 \quad (5.3\text{-}2)$$

where d is the distance from the aperture and λ is the wavelength. The above integral is nothing but the convolution of the aperture function $p(x, y)$ and the function $\exp(-j\pi(x^2 + y^2))$. In all similar problems in literature, a quantity is always defined here, which is the Fresnel number $N_F = a^2/\lambda d$, where a is the

aperture radius. The Fresnel number governs the result of the convolution; that is if N_F is large the shadow of the aperture-i.e., the pinhole is close to a circ function, and if it is small the shape of the beam after the pinhole would be close to Gaussian. To solve our problem, first we define our aperture function from the pinhole, which would be a circle in two dimension so that $p(x,y) = 1$ when $|r| \leq 2.5\mu m$ where $r^2 = x^2 + y^2$. After changing some variables, the intensity as a function of radial positoin r would be

$$I(R) = \left| \int_{R-\sqrt{N_F}}^{R+\sqrt{N_F}} \exp(-j\pi R'^2) dR' \right|^2 \tag{5.3-3}$$

where $R = r/\sqrt{\lambda d}$. After solving equation 5.3-3 and returning to the radial unit of r, the shape of the beam as a function of r is shown in Figure 5.9 as a contour plot with x axis being the radial position r and the y axis being the distance from the pinhole. Another way of presenting the result is shown in Figure 5.10, which shows the beam shape at 0.5 μm in (a), at 20 μm in (b) and at 100 μm in (c) as a function of the radial position.

From the results above, the shape of the beam that enters the multimode fiber depends on the position of the pinhole with respect to the fiber, making the resulting impulse response difficult to interpret, especially knowing that the beam forms significant wings at a fairly close distance of 20 μm (see Figure5.9.).

5.4 Near Field Aperture Launch Experiment

As mentioned in the last section, the beam shape emitted from an aperture is a function of how far we are from it. A way of having a similar beam shape enter the fiber is by fixing the distance between the spatial filter and the fiber on the order of 10 μm., This can be accomplished with a mask set in which gold of 300 nm thickness is deposited on a glass slide. The mask set consists of circles of different diameters, and the light is allowed to go through the glass with these

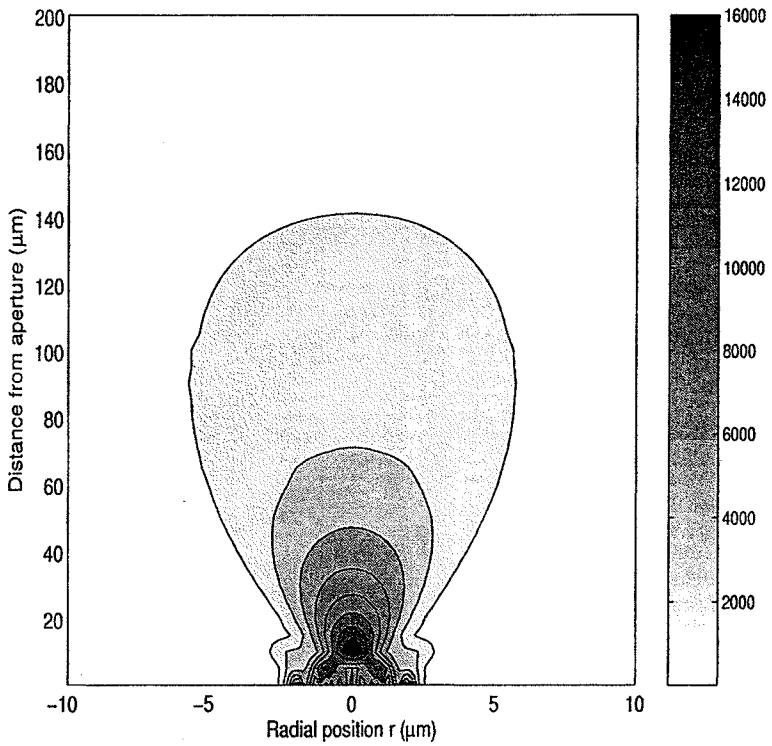

Figure 5.9: Spatial beam shape as a contour plot as a function of distance from aperture.

circles. The experimental set-up used here is the same as that used for the pinhole experiment shown in Figure 5.8 except that the pinhole is replaced by the mask. The distance between the MMF fiber tip and the glass is measured precisely by the use of a white light spectrometer (model Filmetrics F20) . This is done using the set-up shown in Figure 5.11, where the raw reflectance was measured from the MMF fiber tip and displayed on the computer. The maximum reflectance is known from our previous information. Consequently, by separating the glass from the fiber, the reflectance would go down by a percent that would be proportional to the separation distance, and thus we can maintain the required separation of about 10 μm.

When carrying out the experiment with mask set only about 10 μm from fiber, Figure 5.12 shows three results of using the 16 μm diameter aperture (solid),

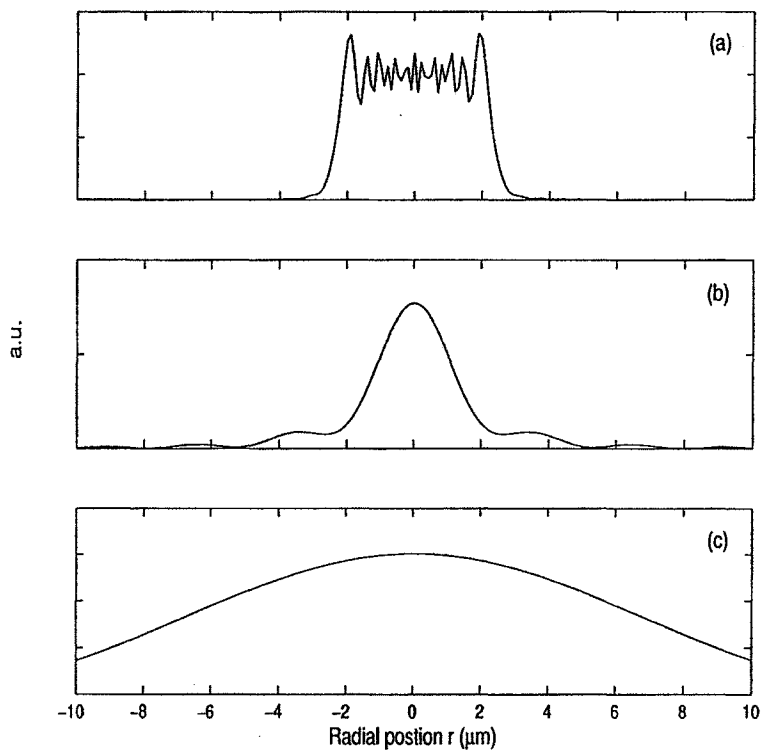

Figure 5.10: Spatial beam shape plot for distance from aperture (a) $0.5\mu m$, (b) $20\mu m$, (c) $100\mu m$.

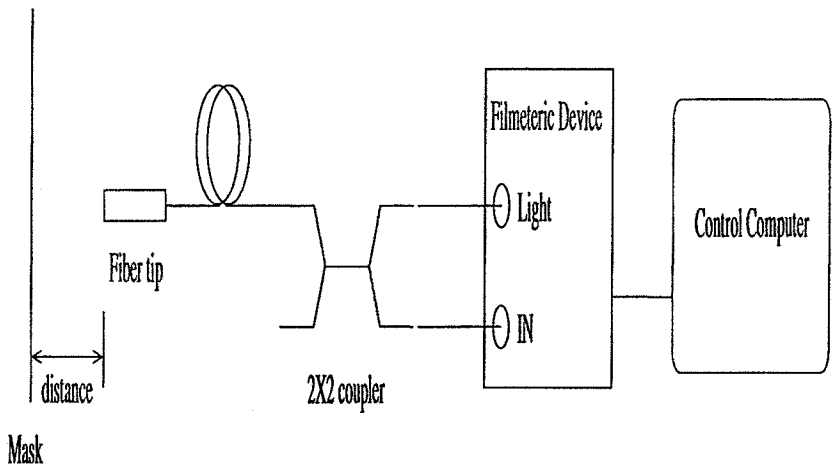

Figure 5.11: Spectrometer setup to measure separation between fiber and mask.

14 μm diameter aperture (dashed), and 12 μm diameter aperture (dotted), which shows the difference in which group of modes are excited by each aperture. Larger

circles were used from 28 μm down to 16 μm but the results were exactly the same as the 16 μm, since the MMF fiber modes reached a cutoff at this particular offset and angle (see Figure 5.13), meaning that at this configuration with the use of Figure 3.4, the cutoff angle is 12 degrees at a distance of about 38 μm from focal spot. leading to the same response for circles from 16 μm and above. Smaller circles (i.e., smaller than 12 μm) were not available at the time of experiment.

After this, the logical sequence is to carry out the same experiment with different circle sizes and then apply the superposition . That is, the smallest circle's response is subtracted from that of the second smallest, the second smallest's response is subtracted from that of the third smallest, and so on until there is a response for every hollow cone that represent a certain angle and offset. This then mapped to the angle offset parametrization graph. The problem with this method is that the minimum size obtained from this mask was as large as 12 μm at the time of the expriment. In future research, it would be useful to fabricate apertures with a wide range of sizes, starting as small as possible. From the available measurement, we can employ this method to obtain two responses for two hollow cones of offset 13 and 15 μm resulting from subtracting the responsse of 12 from 14, and 14 from 16 μm circles respectively. The results of these responses of the hollow cones are shown in Figure 5.14. It is clear from Figure 5.14 that the response of the 15 μm offset cone excites less low order modes than 13 μm. These responses will later be used to validate the model presented in the next section.

5.5 Fiber Modes Model and Effective Impulse Response

As mentioned previously, it is useful to characterize every mode by some quantity that applies to all mode categories. This quantity is the travel time-i.e., the time required by the ray to travel a certain longitudinal distance. This time is normalized to the same distance, not in the direction of propagation but in the longitudinal direction.

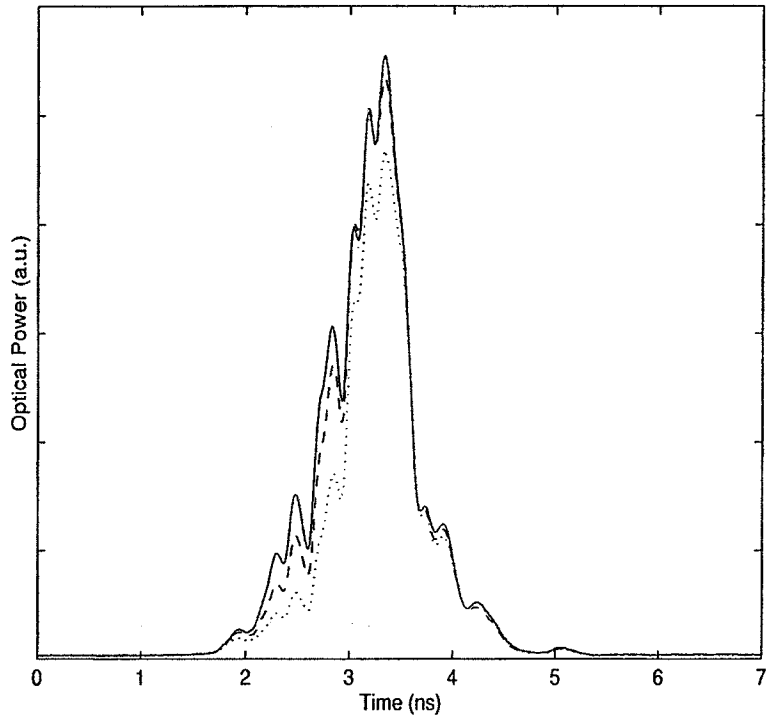

Figure 5.12: Response of 16 μm circle (solid), 14 μm circle (dashed), 12 μm circle (dotted).

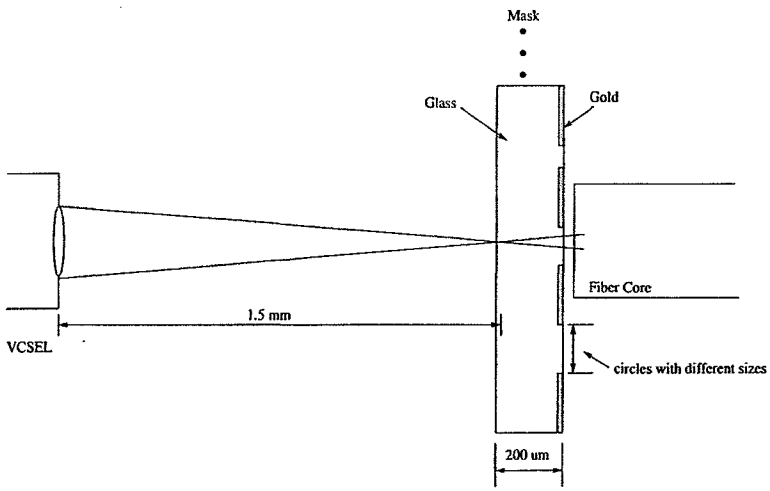

Figure 5.13: Mask set experiment configuration.

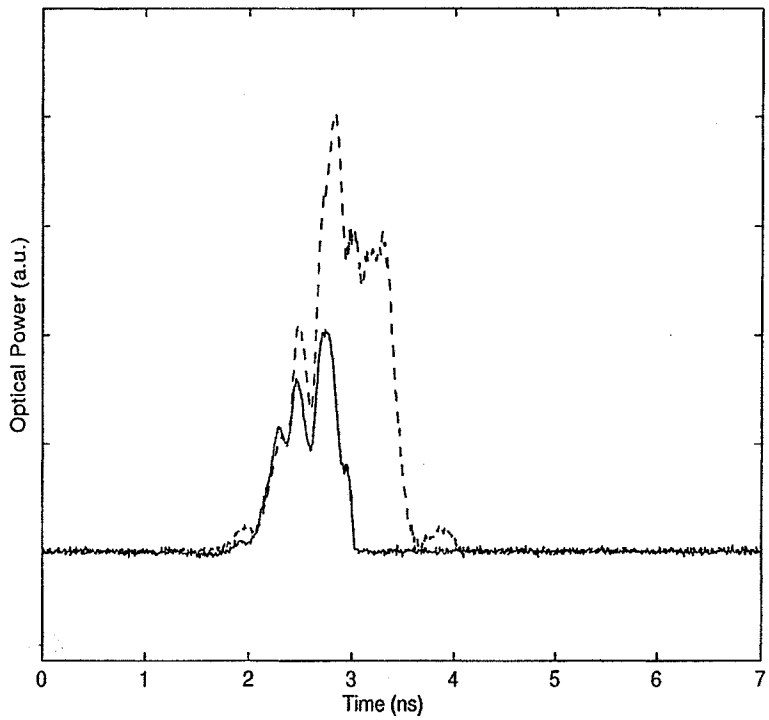

Figure 5.14: Cone responses of 15 μm offset (solid), 13 μm offset (dashed).

This is achieved by considering a refractive index profile, then disecretizing this profile to a finite number of hollow cylinders with a constant refractive index. When the refractive index is constant, the speed of the ray can be calculated by the speed of light divided by the refractive index, and consequently the travel time is the ray speed divided by the distance. Figure 5.15 shows how the fiber core is divided into a finite number of layers (cylinders) to approximate the actual refractive index profile, and how the rays travels through these layers. By considering Snell's law, which states that

$$n_1 \sin(\theta_1) = n_2 \sin(\theta_2). \tag{5.5-4}$$

As the ray enters the fiber from the air, its angle α changes to α_1, and hence the distance d_1 that this ray would travel is calculated by trigonometry as

$$d_1 = \Delta / \sin(\alpha_1), \tag{5.5-5}$$

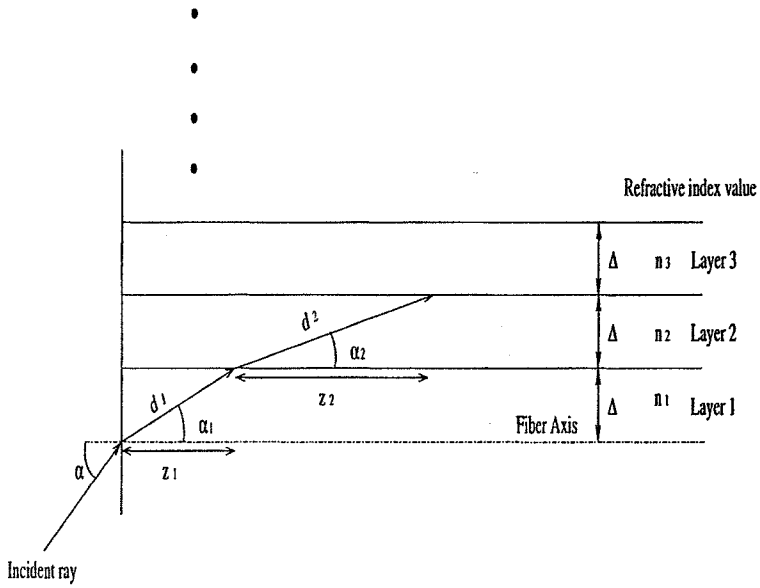

Figure 5.15: parametrization of GIMMF modes by the travel time.

where Δ is the size of the step chosen to approximate the refractive index profile, and as Δ decreases the approximation becomes better. From that, the time required by the ray to travel this distance of d_1 would be

$$t_1 = c/(n_1 d_1), \tag{5.5-6}$$

where c is the speed of light in a vacuum of $3 \times 10^8 m/s$ and n_1 is the refractive index of layer number 1. Here we need the distance d_1 to calculate the time, but we also need to normalize this time to the longitudinal distance of z_1 (see Figure 5.15). These steps are repeated as the ray goes from layer 1 to layer 2, and t_2 and z_2 are calculated. This process is repeated until we obtain a total internal reflection from one layer to the other, say layer n, and then the process is halted and the times are added so the total time to travel a distance of $z_{tot} = z_1 + z_2 + .. + z_n$ is $t_{tot} = t_1 + t_2 + .. + t_n$. After that, all modes with different offsets or angles are normalized to the same length, and then the travel time becomes unique to each ray. To validate the model, a multimode VCSEL was gain-switched and the

optical output of the VCSEL was measured by the wide band optical scope, as shown in Figure 5.16. This signal is then considered as the input pulse to the model. Attenuation is neglected in the model since we are only concerned about the timing of the pulses and attenuation of all modes is assumed to be similar. Hence, the impulse response of each mode (or ray) would be a delta function, but the total beam response of the fiber would be wide since different versions of the signal of Figure 5.16 would reach the receiver due to the different arrival time of each mode.

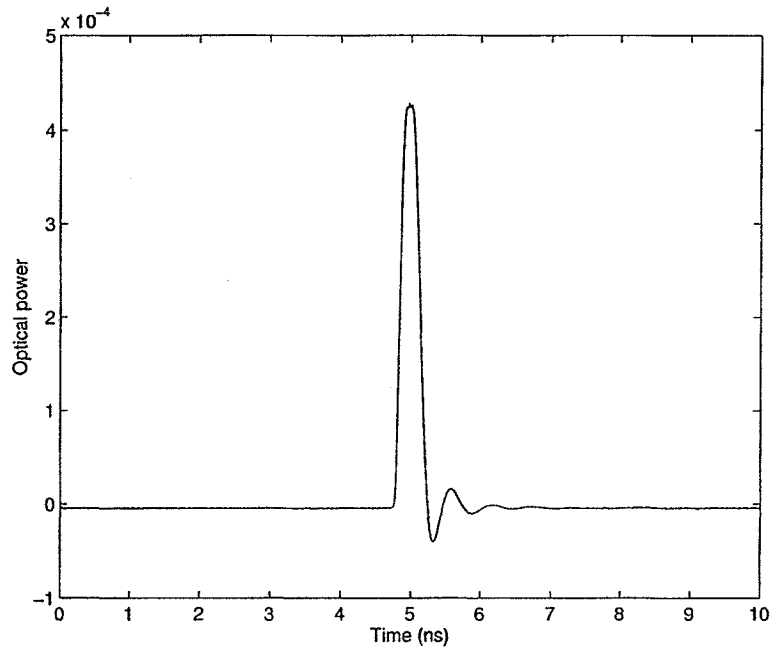

Figure 5.16: Gain-switched VCSEL optical output pulse.

After gain-switching the VCSEL, a single pulse was produced, as shown in Figure 5.16, with a repetition rate of 41.6 MHz. The far field beam divergence distribution was measured, as shown in Figure 5.17. The beam that would enter the MMF fiber from the VCSEL when gain-switched is represented by its beam divergence distribution in Figure 5.17, meaning that the input signal shown in

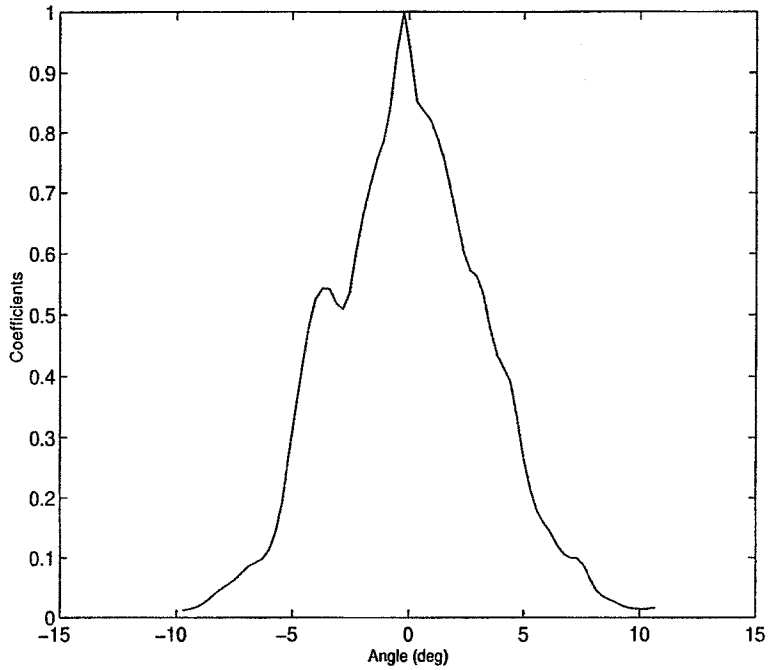

Figure 5.17: Beam divergence distribution of gain switched pulses with weight coefficients displayed.

Figure 5.16 is launched into the MMF fiber at the range of angles shown in the beam divergence distribution and scaled-i.e., multiplied by the coefficients that correspond to those of Figure 5.17. The resolution of the computation can be controlled by controlling the angle step size and the radial distance step size.

It is now time to test the model and adjust the parameters that would permit the result of the model to be as close to reality as possible. The parameters that would affect the result of the model include the refractive index profile, which would have non-ideality in the center of the fiber, either a peak or a dip, and the distance between the fiber face and the focal spot of the VCSEL. The actual measured optical output of the gain-switched VCSEL from the MMF fiber is shown in Figure 5.18- that Is, the response to the signal of Figure 5.16. The model output was tested against the adjustment parameters to yield the output that is closest to the actual measured output of Figure 5.18. Figure 5.19 shows the model

output,which is in good agreement with the measured output and thus validates the model. This is achieved by introducing a peak in the refractive index profile at the center of the fiber and making the distance between the fiber face and the VCSEL's focal spot about 50 μm.

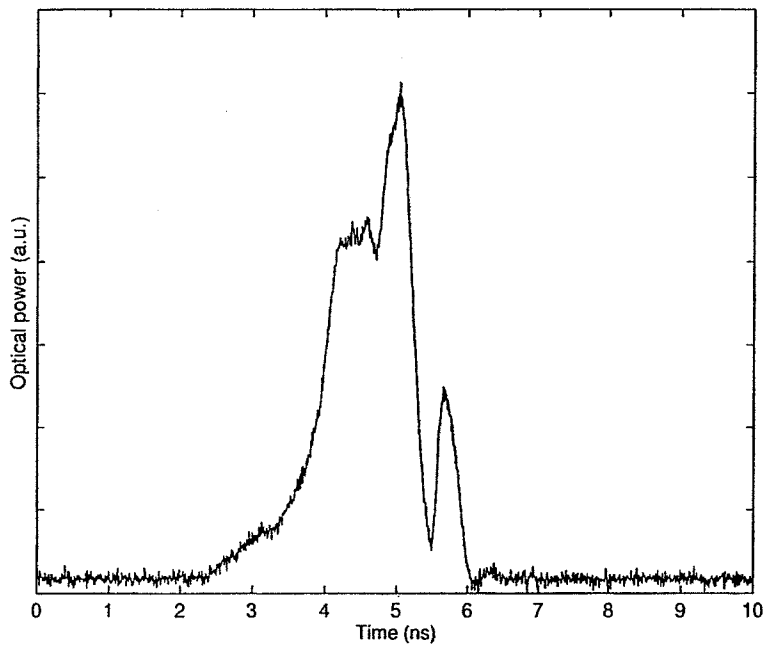

Figure 5.18: Measured gain-switched VCSEL optical output from the MMF fiber.

To further validate the model, the measured hollow cone responses presented in the previous section, shown in Figure 5.14, were used to compare the mean delay time of the measured responses with the model predictions. This is done by calculating the mean delay time of the measured hollow cone responses from a reference time point, namely, the slowest mode peak resulting from the axial mode, which arrived at 6.55 ns, as shown in Figure 5.12. The mean time calculation is carried out by using the following equation:

$$t_{delay} = \frac{\int th(t)dt}{\int h(t)dt} \tag{5.5-7}$$

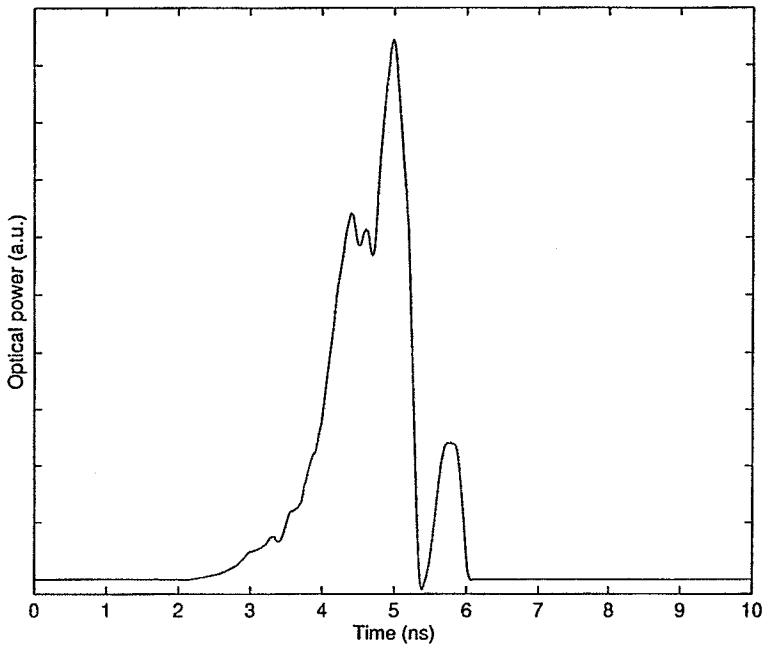

Figure 5.19: Model output.

where $h(t)$ is the hollow cone response. This was from the measured responses. To produce the same beam and let the model predict the delay time, the geometrical configuration is needed- i.e., that the distance between the focal spot and the fiber face should be 38 μm, as mentioned before. The input to the model was 0 degrees in order to know the axial mode arrival time to make it the reference, then a range of offsets that map to a range of angles between 12 to 14 μm for 13 μm diameter cone, and 14 to 16 μm for 15 μm diameter cone was used as inputs to the model. The mean delay of each of the two ranges was calculated to represent each hollow cone delay time. Table 5.1 shows the results of the comparison. Figure 5.20 shows the result of the comparison in figure format, which shows only a few points because of the limited available sizes of circles in the mask set used. However, these few points show good agreement between the model and the measured data

Offset (μm)	Measured Delay Time (ns)	Model Predicted (ns)
0	0	0
6.5	2.12	2.02
7.5	2.36	2.52

Table 5.1: Comparison between measured and model predicted beam mean delay time

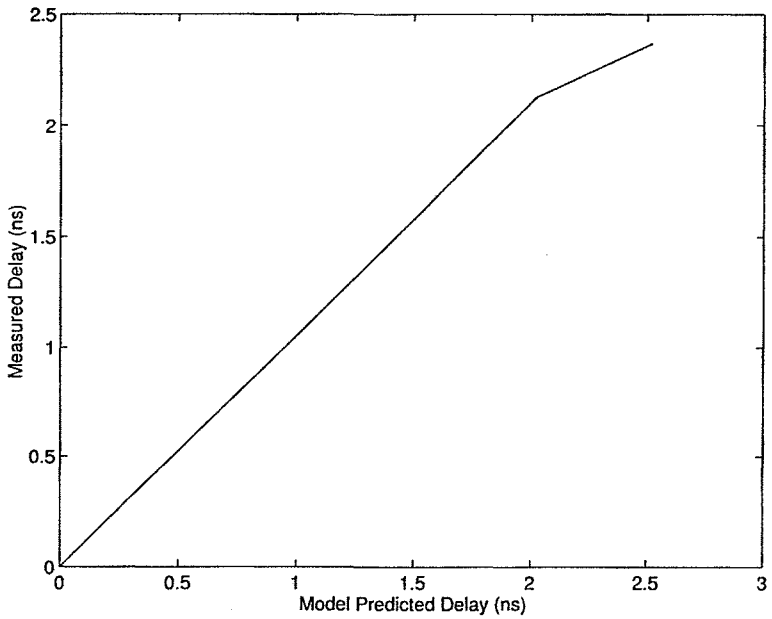

Figure 5.20: Comparison between measured and model predicted beam mean delay time.

It is of great importance for us to use the model to determine how different data patterns would have different impulse responses. The way to do this is as described before-that is, to use the MMF fiber time input signal shown in Figure 5.16 and transmit it through the model according to different beam divergence distributions for each data pattern. Two VCSELs were tested, as shown in Section 4.4, from two major VCSEL manufacturers. The results of their beam divergence distributions have been also shown in section 4.4 where Figure 4.16 shows the beam divergence distribution for part A, with the high frequency pattern as the solid line and the low frequency pattern as the dashed line. Similarly, Figure 4.17 shows the results for part B. Applying the model, Figure 5.21, shows the predicted impulse

responses for part A, with the solid line being the high frequency pattern and the dashed line the low frequency pattern. Similarly, Figure 5.22 shows the resultant impulse responses for part B. From Figure 5.21 and 5.22, it is clear that there is a difference in the impulse response for each data pattern due to the change in the beam divergence distribution. The difference is not so significant but it may be important to be considered when carrying out equalization. In the next section, an adaptive equalization algorithm that takes into account the change in impulse response will be presented.

5.6 Non-linear Equalization

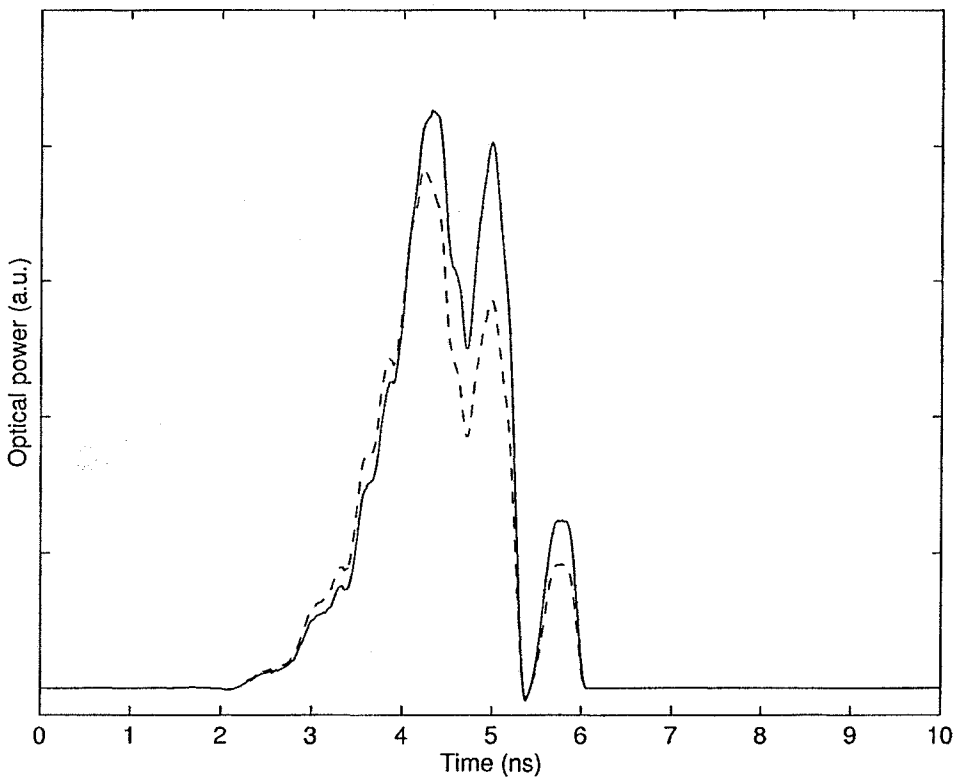

Figure 5.21: Model predicted impulse response for Part A: alternating ones and zeros pattern (solid), alternating sixteen ones and sixteen zeros (dashed).

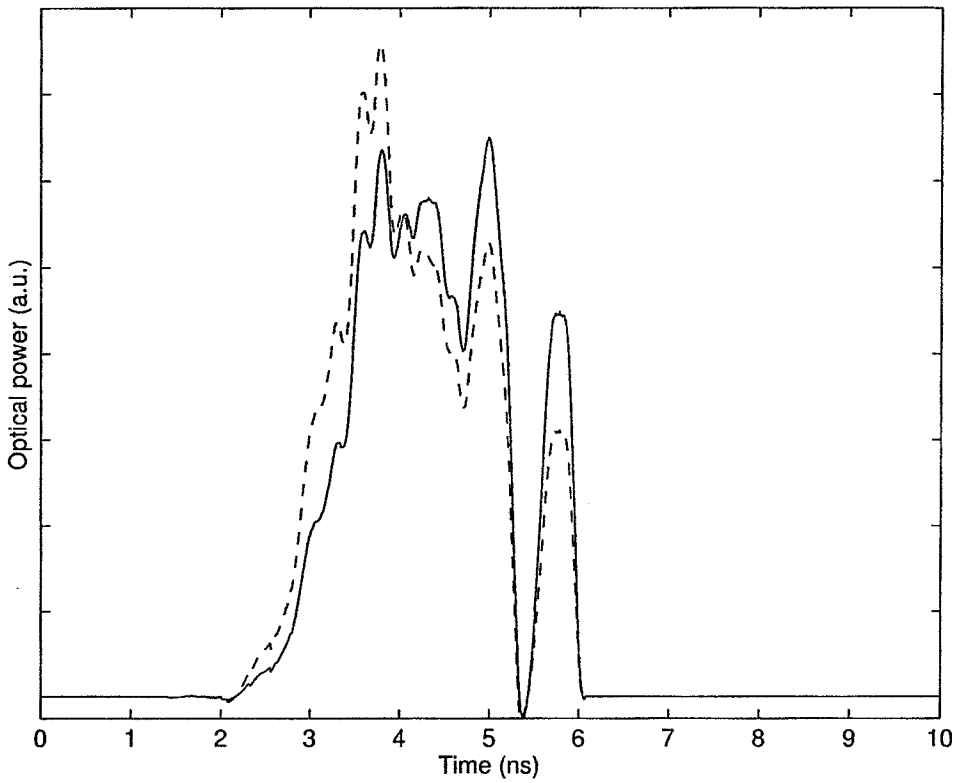

Figure 5.22: Model predicted impulse response for Part B: alternating ones and zeros pattern (solid), alternating sixteen ones and sixteen zeros (dashed).

5.6.1 Method

The idea of mitigating the effect of having different impulse responses for different data patterns is to form a look-up table of impulse responses for every possible data pattern. The way to do this is by first measuring the far field beam divergence distribution for each possible data pattern. This is done by using the experimental set-up described in Section 4.4 of Figure 4.15. Then from these far field scans the corresponding impulse responses are calculated using the model described in the last section. For each impulse response, a tap weight vector is calculated. When deciding on a certain bit depending on the previous bits, one tap weight vector is chosen.

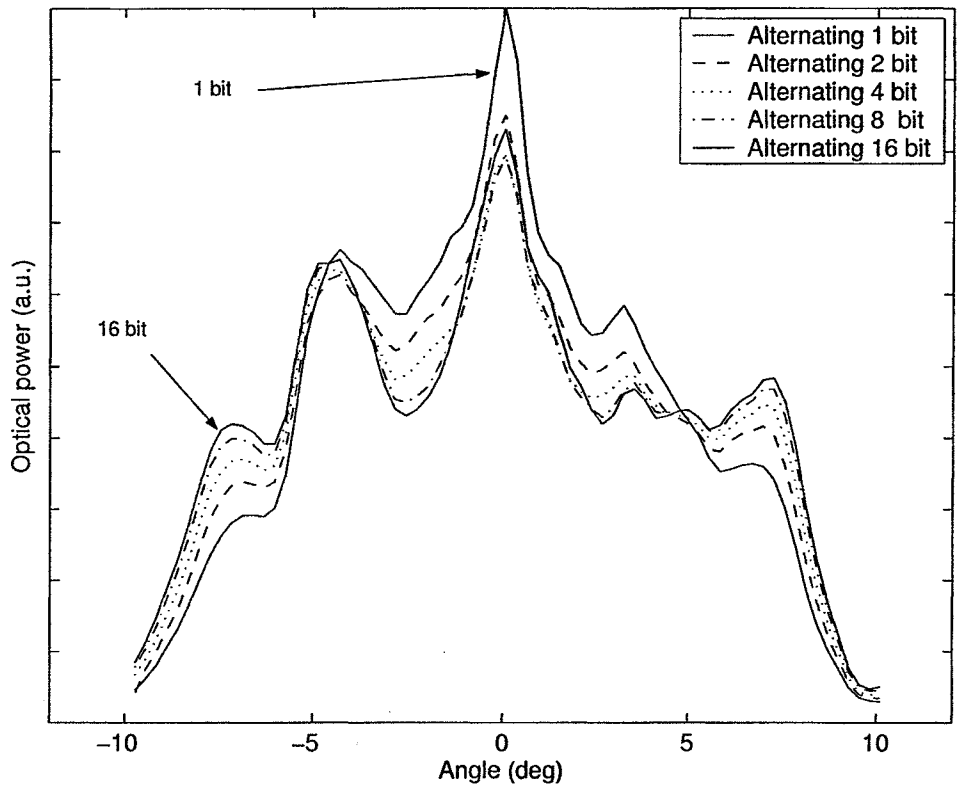

Figure 5.23: Measured far field scans for five different data patterns.

The measured far field scans using part A VCSEL are shown in Figure 5.23, where five different data patterns were produced: the first with alternating one bit, the second alternating two bits, the third alternating four bits, the fourth alternating eight bits, and the fifth alternating sixteen bits, as shown in the legend of the figure. The corresponding impulse responses were calculated from the model. For each impulse response the corresponding tap weight vector was calculated, using the linear zero forcing method.

5.6.2 Algorithm and Results

After forming a look-up table of tap weight vectors for the five possible data patterns using the linear zero forcing method, it is useful to form an algorithm that tracks the received data and decides which tap weight vector should be used. In

Impulse response name	Number of alternating bits	Number of consecutive 1s
Imp1	1	1
Imp2	2	2
Imp3	4	3,4,5
Imp4	8	7,8,9,10
Imp5	16	11,12,13,14,15,16

Table 5.2: Impulse responses with corresponding consecutive ones

Table 5.1. the first column gives the names of the different impulse responses and the second column gives the number of alternating bits with which the far field distributions were measured. The third column gives the corresponding number of consecutive ones that can be mapped to the different impulse responses; for example, if we have seven consecutive ones, we will use Imp4 in the process of equalizing the next bit.

Figure 5.24 shows the flow chart of the algorithm. In the flow chart, the function denoted by i<=c is simply the mapping from column 3 to column 1 in Table 5.2. The steps of the algorithm and escription of the algorithm flow chart is as follows:

- Start with i = 1 i.e Imp1 for alternating one bit.
- Carry out the equalization and test the decided bit one or zero.
- Count the number of consecutive ones as representing the impulse number and convert from c to i.
- If a zero appears, we start a counter b. If the number of zeros (b) detected is less than the number of ones (or what is called the impulse number c) in the previous ones segment, then we stay in the same impulse Impi. If b becomes greater than c, then we switch back to the alternating one bit i.e. Imp1 and clear c and b.

- After that period of ones followed by first zeros we do the same thing: if we detect a one, we start increasing c. However, our concern is the bit before the one, i.e., whether it was zero or one. If it was zero, then we clear c and b and use Impl If it was one, then we repeat the process of increasing c and go to 2nd step.

The results of using the algorithm in equalizing the data at a rate of 1.25Gbps for the 1km MMF are shown in Figure 5.25, where four bit error rate curves are shown. The upper solid line represents no equalization. The dashed line represents a simple linear equalization, and the dotted line represents the algorithm described. The left solid curve shows the BER with no dispersion as the theoretical limit. The results of the algorithm described here were obtained using the method described in Chapter 2. It is clear from the Figure 5.25 that there is an approximately 2 dB power penalty improvement at a standard BER of 10^{-9} by using the pattern dependent algorithm presented here rather than a simple linear equalization.

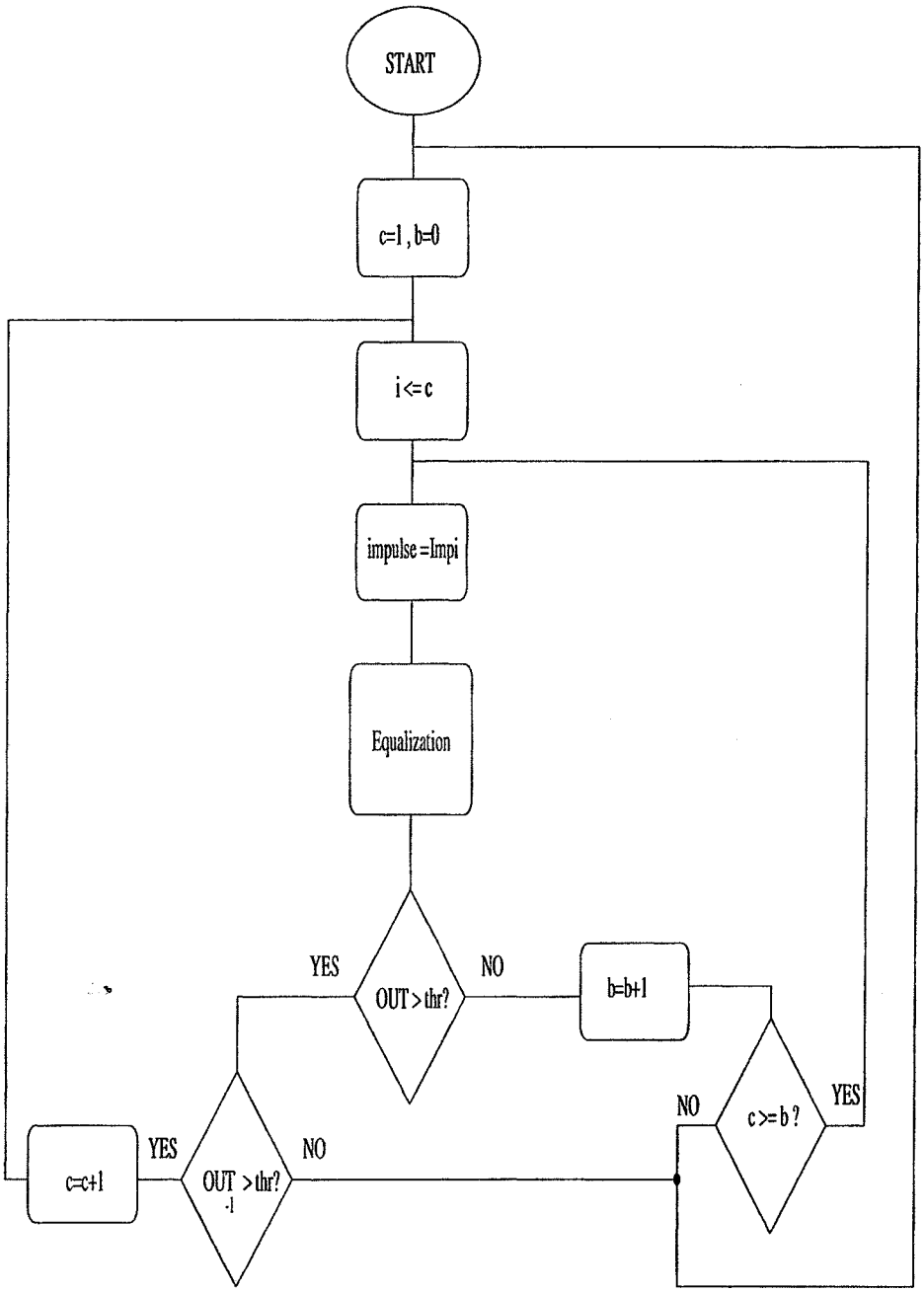

Figure 5.24: Algorithm flow chart.

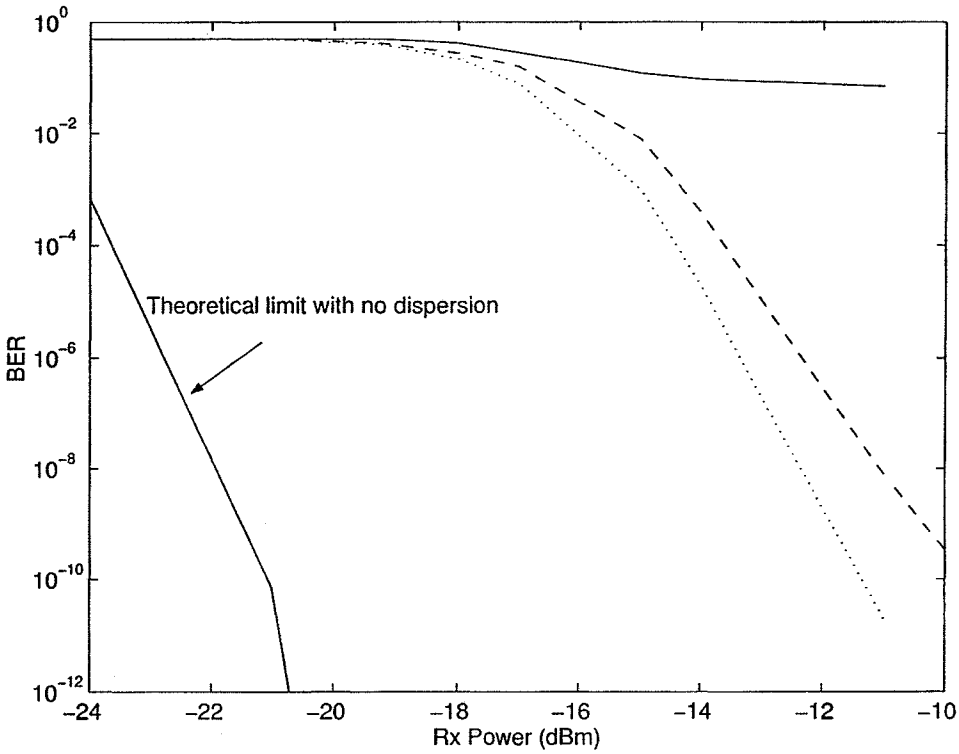

Figure 5.25: BER curves for: no equalization (solid), linear equalization (dashed), the developed algorithm (dotted), and the no dispersion limit shown.

Chapter 6

SUMMARY AND SUGGESTED FUTURE RESEARCH

6.1 Summary

6.1.1 Previous Work

The amount of work that has been published in fiber optic equalization, especially in the area of MMF fibers used in LANs is much less than that published about equalization in copper or wireless systems. Not many papers in the last two to three years have discussed the fiber bandwidth and related parameters. There is a moderate amount of work done in MMF equalization in last few years, but almost all this work, as shown in the literature review, has addressed processing in the optical domain, such as restricted launch condition (RML) and spatially resolved equalization (SRE). On the other hand little work has been presented on equalization processes in the electronic domain. In Chapter 2 we have shown how simple linear equalization, in the electronic domain, has significantly improved the performance of the system based on the result of our method of performance evaluation which is in good agreement with real BER measurements. An improvement to this simple linear equalization was made.

6.1.2 Single Mode Source with MMF

In this dissertation experiments demonstrate that when a multimode VCSEL is connected to a SMF to resemble a single mode optical source the corresponding

MMF fiber bandwidth is reduced by 70 %. A simple operation of separating the SMF fiber from the MMF fiber at an optimum distance would recover the multimode bandwidth without losing more than 10% of the total power[39]. It should be kept in mind that this scheme will maintain a simple, center-launching configuration. Also this same idea was applied using a single mode laser with MMF fiber which dramatically improved the performance of the system as shown by experimental measured eye diagrams and bit error rates. The impact of this result could be significant and should be investigated further since virtually no Gigabit Ethernet offset jumpers are employed due to the cost of the jumper assembly. This method offers significantly lower cost especially when considering the emerging low cost 1300 nm single mode VCSEL technology. On the other hand, the proposed centered, separated launch has been investigated on a single fiber and it might not be as good for other fibers i.e. results of this launch method could be fiber dependent.

6.1.3 Beam Divergence Dependence on Data Pattern and Its Impact on Link Performance

It has been experimentally shown in this dissertation that the beam divergence distribution of a common optical communication source (VCSEL) is data pattern dependent even with data patterns that produce the same thermal conditions[40]-[42]. This result was first reported here in this dissertation it has not been reported in the literature before. Several attempts both experimentally and theoretically have been presented in this thesis to quantify the effect of the nonlinearity of the data pattern dependent beam divergence distribution on MMF links. The approaches include launching with collimated beams at different angles, offset launching, and the use of optical spatial filtering. A model has been implemented, and verified by experimental results, to simulate the propagating modes of the MMF

fiber to be able to calculate the resultant impulse response of a beam and so quantify the change in impulse response with changing the data pattern.

An algorithm has been implemented to take in to account this nonlinearity of data pattern dependent beam divergence distribution when doing the equalization process. This was done by forming a lookup table of the possible generated data patterns and their corresponding impulse responses. Depending on the previously decided bits, the algorithm chooses an impulse response from the lookup impulse responses table to correct for ISI. The results of the performance evaluation of the algorithm was about a 2 dB improvement in power penalty when compared with treating the fiber as a linear channel. This work is thought to be the first that deals with MMF fiber channels considering their non-linearities due to source non-idealities.

6.2 Suggested Future Research

In the field of the improved launch technique for single mode lasers with MMF fiber, it is of great benefit to continue this research by considering different fiber index profiles. If the method gives promising results, it is of interest to practically implement this technique. This might be done by mounting the single mode laser on a transmitter optical subassembly (TOSA) with spacers or stoppers mounted to place the fiber tip at the optimum distance and deal with practical issues such as the reflections and mode selective loss. A challenge to doing this is to monitor the stoppers position and holding the fiber in this place firmly.

Another subject for future work is describing the nonlinearity of the data pattern dependent beam divergence. It would be interesting to perform the mask set experiment with a wide range of circle sizes starting as small as 2 μm in diameter for varying the focal spot from the fiber. This distance, d, determines the geometrical relationship between the launch offset, r, and the launch angle , θ, as

$r = d\theta$. This would map the impulse response of modes onto the offset/angle mode parametrization graph, i.e. the impulse response of each mode that corresponds to certain offset and angle could be found experimentally. Since the problem of mitigating this nonlinearity is related to possible data pattern combinations, the maximum likelihood sequence estimator (MLSE) might be a good field to explore that could improve the performance of the system. A general idea of how this would be done is to set a number of bits as the sequence say n bits. Consider the 2^n possible combination of the bits and for each combination measure the source far field distributions. From these far field scans form a lookup table of the possible impulse responses for each possible sequence. After that integrate this knowledge into the probability set of the MLSE algorithm.

Another challenging problem is to implement such a system in real time, i.e. sending bits through the fiber and receiving them and doing equalization and measuring the bit error rates in real time. This could be done in the receiver side by sampling the electrical signal after the fast photodiode using fast analog to digital A/D converters. The signal after that would be a digital signal so a digital signal processing (DSP) chip is needed to perform the filtering and equalization process. Dealing with digital signals is not easy in real time because of the clock problems. One of the challenges is to build a clock recovery circuit to retrieve the clock from the signal. Another issue that might be a problem is the measurement of the errors in performing the BER measurement if using the BERT. The input to the BERT should be analog, so a digital to analog converters might be required.

REFERENCES

[1] G. Keiser, "Optical Fiber Communications," 3rd Ed., New York NY; McGraw-Hill, 2000.

[2] J. Powers, "An Introduction to Fiber Optic Syatems," 2nd Ed., IRWIN, 1997.

[3] Lima, A.O., Adali, T., Lima, It. Jt, and Menyuk, C.R., "Polarization diversity and equalization for PMD mitigation in optical communication systems," *Acoustics, Speech, and Signal Processing, 2002. Proceedings. (ICASSP '02). IEEE International Conference on* , vol. 3, pp. III-2721-III-2724, 13-17 May. 2002.

[4] Wedding, B., Chiarotto, A., Kuebart, W., and Bulow, H.L, "Fast adaptive control for electronic equalization of PMD," *Optical Fiber Communication Conference and Exhibit, 2001. OFC 2001* , vol. 2, pp. TuP4-1-TuP4-3, Mar. 2001.

[5] Yu, Q., Yan, L.-S., and Willner, A.E., "10-Gb/s PMD compensation following a recirculating fiber loop," *Lasers and Electro-Optics, 2001. CLEO '01. Technical Digest. Summaries of papers presented at the Conference on* ., pp. 567-568, May 2001.

[6] B.L. Kasper, "Equalization of multimode optical fiber systems," *The Bell Systems Technical Journal*, vol. 61 No. 7, pp. 1367-1388, Sep. 1982.

[7] L. Raddatz, I. H. White, D. G. Cunningham, and M.C Nowell, "Increasing the bandwidth-distance product of multimode fibre using offset launch," *Electronics Letters*, vol. 33, pp. 232-233, Jan. 1997.

[8] L. Raddatz, I. H. White, D. G. Cunningham, and M.C Nowell, "An experimental and theoretical study of the offset launch technique for the enhancement of the bandwidth of multimode fiber links," *Journal of Lightwave Technology*, vol. 16, pp. 324-331, March 1998.

[9] L. Raddatz, I. H. White, D. G. Cunningham, and M.C Nowell, "Bandwidth enhancement of multimode fiber Gbits/s networks using conditioned launch," *Summaries of papers presented at the Conference on Lasers and Electro-Optics, 1998. CLEO 98. Technical Digest*, pp. 396-397, May 1998.

[10] M. Webster, L.J. Sargent, P.J. Heard, K.A. Williams, R.V. Penty, I. H. White, D. G. Cunningham, and M.R.T. Tan, "A simple device to allow enhanced bandwidths at 850 nm in multimode fibre links for gigabit LANs," *Summaries of papers presented at the Conference on Lasers and Electro-Optics, 1999. CLEO 99. Technical Digest*, pp. 242-243, May 1999.

[11] S. Choi, K. Oh, W. Shin, C.S. Park, U.C. Paek, K.J. Park, Y.C. Chung, Y. Kim, and Y.G. Lee, "Novel mode converter based on hollow optical fiber for Gigabit LAN communication ," *IEEE Photon. Technol. Lett.*, vol. 14, pp. 248-250, Feb. 2002.

[12] K.M Patel, and S.E. Ralph, "Enhanced multimode fiber link performance using a spatially resolved receiver," *IEEE Photon. Technol. Lett.*, vol. 14, pp. 393-395, March 2002.

[13] K.M Patel, and S.E. Ralph, "Multimode fiber link equalization by mode filtering via a multisegment photodetector ," *2003 IEEE MTT-S International, Microwave Symposium Digest*, vol. 2, pp. 1343-1346, June 2003.

[14] C. Argon, K.M. Patel, S.W. McLaughlin, and S.E. Ralph, "Spatially resolved equalization and forward error correction for multimode fiber links," *IEEE International Conference on Communications, 2002. ICC 2002.*, vol. 3, pp. 1726-1730, 28 April-2 May 2002.

[15] C. Argon, K.M. Patel, S.W. McLaughlin, and S.E. Ralph, "Spatially resolved equalization and decision feedback equalization for multimode fiber links," *2002 IEEE/LEOS Summer topic in All-Optical Networking.*, pp. TuB31-19-TuB31-20, July 2002.

[16] M. Bruensteiner, G.C. Papen, J. Poulton, S. Tell, R. Palmer, K. Giboney, D. Dolfi, and S. Corzine, "3.3-V CMOS pre-equalization VCSEL transmitter for gigabit multimode fiber links," *IEEE Photon. Technol. Lett.*, vol. 11, pp. 1301-1303, Oct. 1999.

[17] X. Zhao, and F.S Choa, "Demonstration of 10-Gb/s transmissions over a 1.5-km-long multimodefiber using equalization techniques," *IEEE Photon. Technol. Lett.*, vol. 14, pp. 1187-1189, Aug. 2002.

[18] P. Pepeljugoski, J. Schaub, J. Tierno, J. Kash, S. Gowda, B. Wilson, H. Wu, and A. Hajimiri, "Improved performance of 10 Gb/s multimode fiber optic links using equalization," *Optical Fiber Communications Conference, 2003.*, pp. 472-474, March 2003.

[19] C. Pelard, E. Gebara, A.J. Kim, M. Vrazell, E.J. Peddil, V.M. Hietala, S. Bajekal, S.E. Ralph, and J. Laskar, "Multilevel signaling and equalization

over multimode fiber at 10 Gbit/s," *2002 Gallium Arsenide Integrated Circuit (GaAs IC) Symposium, 2003. 25th Annual Technical Digest 2003. IEEE, 2003* ., pp. 197-199, 2003.

[20] R. Khosla, K. Kumar, K.M. Patel, C. Pelard, and S.E. Ralph, "Equalization of 10GbE multimode fiber links," *The 16th Annual Meeting of the IEEE, Lasers and Electro-Optics Society, 2003. LEOS 2003.*, vol. 1, pp. 169-170, 26-30 Oct. 2003.

[21] J.G. Proakis, "Digital Communications," 3rd Ed., New York NY; McGraw-Hill, 1995.

[22] D.R. Smith, I. Garrett, "A simplified approach to digital optical reciever desgin," *Journal of Optical Quantum Electronics*, vol. 10, pp. 211-220, Feb. 1978.

[23] L.J. Sargent, M. Webster, I.H. White, P.J. Heard, R.V. Penty, M.R.T. Tan, and D.G. Cunningham, "Simple technique for bandwidth enhancement of multimode fibre links using controlled spatial emission from vertical cavity surface emitting lasers ," *Electronics Letters.*, vol. 34, pp. 2038-2040, Oct. 1998.

[24] M. Webster, L. Raddatz, I. H. White, and D. G. Cunningham, "A statistical analysis of conditioned launch for gigabit ethernet links using multimode fiber," *Journal of Lightwave Technology*, vol. 17 Issue: 9, pp. 1532 -1541, Sep. 1999.

[25] L. Raddatz, I. H. White, "Overcoming the modal bandwidth limitation of multimode fiber by using passband modulation," *IEEE Photon. Technol. Lett.*, vol. 11, pp. 266-268, Feb. 1999.

[26] L. Raddatz,I. H. White,D. G. Gunningham, and M. C. Nowell, "Influence of restricted mode excitation on bandwidth of multimode fiber links," *IEEE Photon. Technol. Lett.*, vol. 11, pp. 534-536, Apr.1998.

[27] IEEE802.3z Gigabit Ethernet Standard

[28] Y. Koyamada, and K. Yamashita, "Launching condition dependence of graded-index multimode fiber loss and bandwidth ," *Journal of Lightwave Technology*, vol. 6 Issue: 12, pp. 1866 -1871, Dec. 1988.

[29] Z. Hass, and M. A. Santoro, "A mode-filtering scheme for improvment of the bandwidth-distance product in multimode fiber systems ," *Journal of Lightwave Technology.*, vol. 11, pp. 1125-1131, Jul. 1993.

[30] P. Sundgren, R.M. von Wurtemberg, J. Berggren, M. Hammar, M. Ghisoni, V. Oscarsson, E. Odling, and J. Malmquist, "High-performance 1.3 */mum* InGaAs vertical cavity surface emitting lasers ," *Electronics Letters.*, vol. 39, pp. 1128-1129, July 2003.

[31] M. Young, "Mode-field diameter of single mode optical fiber by far-field scanning," *Applied Optics.*, vol. 37, pp. 5605-5619, Aug. 1998.

[32] M. Young, "Mode-field diameter of single mode optical fiber by far-field scanning: addenum," *Applied Optics.*, vol. 37, pp. 836-837, Dec. 1998.

[33] R. Walker, and R. Dugan, (1999, November). Low overhead coding proposal 10GbE serial links. Presented at IEEE802.3 Higher Speed Study Group November 1999 Plenary Week Meeting. [online]. Available: http://group.ieee.org/groups/

[34] K.L. Lear, R.P. Schneider Jr., K.D. Choquette, and S.P. Kilcoyne, "Index guiding dependent effects in implant and oxide confined vertical-cavity lasers," *IEEE Photon. Technol. Lett.*, vol. 8, pp. 740-742, June 1996.

[35] D.V. Kuksenkov, H. Temkin, and S. Swirhun, "Polarization instability and relative intensity noise in vertical-cavity surface-emitting lasers," *Applied Physics Letters*, vol. 67, pp. 2141-2143, Oct. 1996.

[36] D. Marcuse, "Calculation of bandwidth from index profiles of optical fibers. 1: Theory," *Appl. Opt.*, vol. 18, pp. 2073-2080, June. 1979.

[37] J.T. Verdeyen, "Laser Electronics," 2nd Ed., Englewood Cliffs NJ; Prentice Hall, 1989.

[38] B. Saleh, M. Teich, "Fundamentals of Photonics," 2nd Ed., John Wiley and Sons, 1991.

[39] S. Al-Sowayan, and K. L. Lear, "MMF bandwidth enhancement by longitudinal displacement launch ," *Proceedings of IEEE/LEOS 2004 Annual Meeting*, pp. 985-986.

[40] S. Al-Sowayan, and K. L. Lear, "Data pattern dependence of VCSEL far-field distributions ," *IEEE Photon. Technol. Lett.*, vol. 16, pp. 2215-2217, Oct. 2004.

[41] S. Al-Sowayan and K. L. Lear, "Beam divergence angle distribution dependence on data pattern ," *Proceedings of SPIE - The International Society for Optical Engineering, Vertical-Cavity Surface-Emitting Lasers VIII Conf.*, Vol. 5364, pp. 138-145, San Jose, CA, January 2004.

[42] S. Al-Sowayan, and K. L. Lear, "Multimode fiber response dependence on data pattern ," *Proceedings of IEEE/LEOS 2004 Annual Meeting*, pp. 757-758.

[43] M. Nakamura, "Single mode operation of semiconductor injection lasers," *IEEE Transactions on Circuits and Systems,* vol. 26, pp. 1055-1065, Dec. 1979.